Dual-mode Ultrasound: Magnetoacoustics for Biological Tissue Imaging and Ultrasound Mediated Neuromodulation

A DISSERTATION
SUBMITTED TO THE FACULTY OF THE
UNIVERSITY OF MINNESOTA
BY

Kai Yu

IN PARTIAL FULFILLMENT OF THE REQUIREMENTS

FOR THE DEGREE OF

DOCTOR OF PHILOSOPHY

Dr. Bin He, Adviser

August 2018

Acknowledgements

I would first like to sincerely thank my advisor Professor Bin He for constantly providing me with guidance and support during my research in the past six years. For the first three years of my Ph.D. training, Dr. He encouraged me from many aspects and offered me a myriad of opportunities working independently. Without his foresight project planning and insightful advices, I may not have the chance to join the big community of neuromodulation and thus the Brain Initiative during my second three years.

I would also thank my current and former committee members, Dr. Wei Chen, Dr. Shai Ashkenazi, Dr. Esther Krook-Magnuson, Dr. Paolo Provenzano, and Dr. Emad Ebbini for their kind support towards this dissertation.

Throughout my Ph.D. study, I have been receiving many helps from lab colleagues, collaborators and friends. I would thank Dr. Leo Mariappan for leading me into the magnetoacoustic world, and thank Dr. Xiaotong Zhang, Dr. Jiaen Liu and Dr. Yicun Wang for all stimulating discussions in electrical property imaging. I would also like to thank Dr. John C. Bischof, Dr. Qi Shao and Dr. Chunlan Jiang for developing an animal model for my research. Besides, I also want to deliver my special thanks to Dr. Qi Shao here for being a wonderful research collaborator and a close friend. We conducted and explored many interesting experiments together, and even spent much time together “debating” on numerous topics. He and my first undergraduate research assistant, Ms. Maryam Zhian offered their great help on initiating the experiments of Lorentz-current and ultrasound neuromodulation.

Dr. Dalong Liu and Mr. Hasan Aldiabat also provided their generous help in this early phase of the experimentation.

I would also thank Ms. Xiaodan (Rachel) Niu for her tremendous efforts working together on the ultrasound neuromodulation project. She has been sharing a pile of bright research ideas with the group, which really pushes our project to make steady progress. I would extend my appreciation to Dr. Haiteng Jiang, Dr. Yi Zhang, Dr. Wynn Legon, Dr. Nessa Johnson, Dr. Michelle Case, Dr. Chris Cline, Dr. John Basile, Mr. Daniel Suma, and Ms. Mickinney Zhang for their help in many discussions and experimental practices. I would thank Dr. Yicun Wang and Dr. Xiaohong Zhu for their time and kind help on customizing the MR scanning for my research project.

Here, I would also send special thanks to one of my colleagues and friends, Abbas Sohrabpour for the years-long collaboration on both research projects. I really appreciate his expertise, efforts and most of all his patience in helping me improve the experiment, conduct data analysis and initiate useful discussions.

Thank you to all my current and former colleagues of Biomedical Functional Imaging and Neuroengineering Lab. Thank you to all my dear friends in Minnesota.

Dedication

This dissertation is dedicated to my beautiful wife Qingnan Yang, my parents, parents-in-law and grandparents. The blessing of their constant support endows me with ongoing courage and strength.

This is also dedicated to my lovely daughter, Ocean S. Yu, who would be 1-year, 4-month and 10 days old when her father defends his own thesis. She makes my life even brighter than ever before.

Abstract

Ultrasound is a type of mechanical energies that have been widely employed in clinical diagnosis and therapeutic use. The overall goal of this dissertation is to further develop ultrasound-based imaging modality in assisting cancer diagnosis and explore the transcranial focused ultrasound (tFUS) in brain stimulation. In this dissertation, I firstly summarize my research on detecting cancer by harnessing a passive-mode ultrasound generated by magnetoacoustics. Probing the electrical conductivity of *in vivo* tissues, a high-frequency magnetoacoustic tomography with magnetic induction (hfMAT-MI) imaging system has been developed for cancer imaging with 1-mm spatial resolution. With the aid of magnetic nanoparticles (MNPs), the magnetoacoustic tomography is further enhanced in the imaging contrast and thus used to reconstruct the *in vivo* biodistribution of MNPs noninvasively. By reversing the imaging model, I secondly introduce my studies of transmitting active-mode pulsed ultrasound in a transcranial way and electrically sensing global and local brain responses to the deposited low-intensity ultrasound energy. In this second research topic, non-invasive electroencephalography (EEG)-based source imaging (ESI) is used to map the whole brain dynamics, which allows to better understand the effects of tFUS stimulation with high spatiotemporal resolutions. Furthermore, towards a mechanistic investigation, intracranial electrophysiological recordings from *in vivo* brains receiving low-intensity tFUS uncover an intrinsic cell-type specificity of neurons in responding to levels of ultrasound pulse repetition frequencies.

Potential confounding factors, i.e. auditory side effects and somatosensation are also studied to thus identify the direct neuronal effects induced by the tFUS *in vivo*.

Table of Contents

List of Tables

List of Figures

Chapter 1: Introduction

1.1 Magnetoacoustics: A Passive-mode Ultrasound Detection for Non-Invasive Cancer Diagnosis

1.1.1 Magnetoacoustic Tomography with Magnetic Induction (MAT-MI) for Probing Electrical Conductivity of Biological Tissues [1]

Electrical properties of biological tissue including electrical conductivity σ and permittivity γ are important biophysical parameters in the study of electrophysiology and electromagnetic therapies such as transcranial direct current stimulation (tDCS) [2]. In addition, due to their changes under physiological and pathological conditions, tissue electrical properties may serve as an imaging contrast for possible diagnosis and research use [3]. Previous studies have shown that cancerous breast tumor tissue has significantly different electrical properties than normal breast tissue or benign tumors [4-6]. Significant electrical conductivity difference has also been found between liver tumors and normal liver tissue [7]. Generally, such differences between carcinoma and normal tissue are attributed to different cellular water content, amount of extracellular fluid, membrane permeability, packing density and orientation of the malignant cells [8]. Other than carcinomas, tissues under conditions of ischemia, hemorrhage or edema are expected to exhibit different electrical properties as blood and most body fluid have quite different conductivity and permittivity than most other soft tissues [9, 10]. Therefore, noninvasive imaging methods measuring tissue electrical properties

with good accuracy and high spatial resolution are of great research and clinical interest.

Over decades, different electromagnetic imaging methods have been developed to measure electrical properties of biological tissue, including electrical impedance tomography (EIT) [11, 12], magnetic induction tomography (MIT) [13] and magnetic resonance electrical impedance tomography (MREIT) [14, 15]. Among these techniques, EIT maps tissue electrical properties using acquired surface voltage measurements in response to different current injections. Though EIT has advantages in its low cost, real-time speed and safety, major limitations including its low spatial resolution and degraded sensitivity in the center of an object still hinder its broader application. In addition, due to its use of current injection through surface electrodes, EIT may be limited by the 'shielding effect' [16] caused by an insulating or low conductive region in the object, such as bone or adipose tissue. In comparison, MIT uses dynamic magnetic field to induce current in conductive tissue and measures the second magnetic field generated by the induced eddy current using noncontact sensing coils. Yet, because of the ill-posed inverse problem similar to EIT, the spatial resolution of current MIT techniques is still quite limited. In order to achieve high spatial resolution in imaging electrical conductivity, MREIT has been developed by combing EIT and magnetic resonance current density imaging (MRCDI) [17]. With current injection through surface electrodes similar to EIT while measuring the corresponding magnetic field disturbance generated by injected current in tissue through magnetic resonance imaging (MRI), MREIT made it possible to map electrical conductivity in *ex*

vivo and *in vivo* tissues with high spatial resolution [18, 19]. However, a relatively high level of current injection (on the level of mA) is generally required in MREIT to obtain sufficient signal-to-noise ratio (SNR) level and the use of MRI machines makes the cost of MREIT higher than other methods.

Alternative approaches utilizing the coupling between electromagnetic field and acoustic field have also been developed to image electrical properties of tissue or bioelectrical current [20]. Such kind of coupling was first demonstrated in magnetoacoustic tomography (MAT) [21, 22] and Hall effect imaging (HEI) [23]. In MAT and HEI, the imaging object is placed in a static magnetic field. Spontaneous or injected current flow, which is associated with ion movement in biological tissue, is then coupled to acoustic vibrations through Lorentz force acting on these moving ions. Such vibrations can be sensitively detected by ultrasound transducers and used for possible mapping of the bioelectric current or tissue electrical properties with spatial resolution close to ultrasound imaging. Using similar coupling mechanism in a reverse mode, one can apply ultrasonic energy to the imaging object and record voltage/current signals to obtain the sample's conductivity information [24-26]. Such technique was also called magneto-acousto-electrical tomography (MAET) [27-29] or Lorentz force electrical impedance tomography (LFEIT) [30, 31]. Of course, the problem of the 'shielding effect' associated with the use of surface electrodes for current injection or voltage measurement, i.e. regions surrounded by low-conductive tissue become invisible, still exists in these methods. Such problems have then led to the development of magnetoacoustic tomography with magnetic induction (MAT-MI) [32, 33]. MAT-MI utilizes magnetic

induction to induce eddy current in the conductive sample and generates acoustic vibrations through the same Lorentz force coupling mechanism as in MAT or HEI. Ultrasound waves are then sensed to reconstruct the electrical conductivity related image. Ever since the MAT-MI method was proposed, there have been many numerical studies [34-37] and experimental studies using physical phantoms [38-40] or biological tissues [41, 42] demonstrating the feasibility and performance of MAT-MI. Advancement on experimental system design [43, 44] and image reconstruction algorithms [44, 45] has also been achieved in recent years. In addition, similar to the reverse mode of HEI or MAET, i.e. applying ultrasound transmission and measuring the Lorentz force induced current or voltage for imaging electrical conductivity, the reverse mode of MAT-MI—named magneto-acousto-electrical tomography with magnetic induction (MAET-MI)—has also been developed recently [46], which uses ultrasound stimulation and coil measurement of the dynamic magnetic field generated by Lorentz force induced current in conductive imaging objects.

1.1.2 Magnetoacoustic Tomography (MAT) for Imaging Magnetic Iron Oxide Nanoparticles [47]

In recent years, magnetic nanoparticles (MNPs) have been widely used as contrast agents in a variety of clinical and molecular imaging modalities [48]. Target specificity is typically accomplished by coating MNPs with appropriate tumor/tissue specific markers, such as antibodies, allowing them to bind to the tumor region [49, 50]. These nanoparticles can then be imaged within the tumors for clinical applications such as detection or pre-treatment planning. For instance,

there is a wide consensus that early detection of cancer improves both 5-year survival rates and quality of life for patients. As seen in clinical data from 24,740 cases, five-year breast cancer survival rates can reach 96.2% if the tumor is diagnosed when the size is less than 5 mm [51]. This has led to significant effort in exploration of contrast agents and biomarker indicating tumors [52]. Also, techniques are being actively developed to image cancer through the use of indigenous tissue properties such as elastic properties [53] or electrical properties (EP) at various electromagnetic wavelengths [33, 54-58]. The goal of these efforts is to obtain highly sensitive, good resolution detection of tumors.

In addition to magnetic nanoparticles being used as imaging contrast agents, they are also being actively investigated as therapeutic agents owing to the ability to heat MNPs by alternating radiofrequency (RF) magnetic fields. Thus, the use of magnetic nanoparticles could lead to theranostic (therapeutic and diagnostic) applications in cancer management [59-61]. For these reasons, developing high spatial resolution imaging techniques for the detection of the distribution of these MNPs in tissue is desired.

Several imaging techniques for estimating the distribution of nanoparticles in tumors have been explored in recent years. Magnetic resonance imaging (MRI) was first used to image magnetic nanoparticle-labeled molecular targets, as it can provide an enhanced imaging contrast because of its nature and properties significantly shortening T2 relaxation time [62, 63]. The reduced relaxation time of the signal in MRI is seen to depend on the concentration of the magnetic nanoparticles used, and research is ongoing to be able to reliably detect these

nanoparticles under shortened relaxation times at nanoparticle concentration levels in the 1–10 mg Fe/ml range [64]. Using the sweep imaging with fourier transformation (SWIFT) MRI technique, quantitative imaging of up to 3 mg Fe/ml concentration of iron oxide nanoparticles (IONPs) is possible [64, 65]. CT scanning has also been explored as another approach for estimating the distribution of magnetic nanoparticles [66]. The IONP distribution above 10 mg Fe/ml is well recognized in the CT images with the sensitivity limited below this concentration [66]. In addition, the cost of MRI or CT imaging systems represents an economic burden for large scale screening for early cancer detection applications [67]. Another approach that has been explored for detecting MNPs is based on the heating effect [61, 68] which applies alternating magnetic fields and raises the temperature of the MNP labeled tumor. This raises the temperature distribution around the tumor which is then used to estimate its location. However, this technique is limited by its ability to detect superficial tumors at depths of up to 1.5 cm under the surface. It is also limited by the amount of heat applicable to the tissue for diagnostic purposes. On the other hand, ultrasound penetrates soft tissue with imaging depths of tens of centimeters in the current ultrasound systems in the few MHz frequency range [69]; in this frequency range, the imaging resolution is better than 1 mm. In addition, ultrasound based systems could provide a cost-effective imaging alternative to MRI or CT.

Recently, several ultrasound-based imaging techniques have been developed in which a secondary effect of the nanoparticles is being used to indicate their presence. Photoacoustic (PA) imaging is based on the detection of

changes in optical absorption properties due to the presence of nanoparticles. In PA imaging, nano agents with well-characterized absorption spectrums absorb the applied laser pulses. This energy then converts to heat, generating acoustic waves detectable with an ultrasound receiver [70, 71]. In magneto-motive force based nanoparticle detection, an RF magnetic field is applied to the tissue labeled with MNPs experiencing a mechanical force from the magnetic field. The resultant mechanical fields from this force can then be used to image the nanoparticles present in the tissue, which is a diamagnetic medium without such magnetic forces. Imaging methods using these magneto-motive forces, leading to the displacement in MNP labeled tissue, have been proposed for reconstructing these nanoparticle distributions [72-75]. One such technique is based on displacement measurements using optical coherence tomography (OCT) called magneto-motive optical coherent tomography (MM-OCT) [72, 73]. However, MM-OCT has limited detection depth due to the strong scattering of light in tissues. Alternatively, ultrasound based methods using B-mode or M-mode ultrasound measurements of magnetic nanoparticle displacement for deep tissue imaging have been proposed as presented in magneto-motive ultrasound imaging (MM-US) [74, 75]. These previously used imaging methods using magneto-motive force either apply continuous alternating magnetic fields or millisecond long, alternating pulsed magnetic fields to generate tissue displacement images and perform measurement of the displacement which is prominently induced along the direction of the force.

In our new method called magneto acoustic tomography (MAT) [76], we apply a short, microsecond duration magnetic pulse to the tissue with MNP. This leads to a short pulsed magneto motive force acting on the MNP creating acoustic vibrations that spread in all directions throughout the medium. In addition, these acoustic vibrations are at the same frequency as the dynamic magnetic field, which is chosen to match the ultrasound frequency range. This allows recording of these acoustic waves with ultrasound transducers placed around the object in this study. This measured signal can then be used to reconstruct the acoustic source distribution in the object by using possible ultrasound imaging approaches [77, 78] leading to the reconstructed images having a good resolution of ultrasound imaging and good imaging depth in soft tissue. The imaging resolution and depth are primarily governed by the ultrasound system used. The imaging resolution is a function of the ultrasound bandwidth and the imaging depth is governed by the ultrasound attenuation in tissue. In the MAT method the ultrasound transducer is used only in the sensing mode unlike traditional ultrasound imaging where the transducer acts as both transmitter and receiver of acoustic waves. This allows the MAT method to have improved imaging bandwidth, limited mainly by the receiving bandwidth of the transducer, leading to better resolution. Also, as compared to traditional ultrasound imaging, the MAT method has lower ultrasound attenuation due to the tissue from the reduced travel path of the acoustic waves from the MNPs embedded in tissue to the sensing transducer leading to improved imaging depth. The MAT method is similar to magneto acoustic tomography with magnetic induction (MAT-MI), which is being explored for high resolution bioimpedance

imaging [33, 79]. With MAT-MI a combination of pulsed and static magnetic fields is used to generate acoustic fields by using Lorentz force; this acoustic field can be used to estimate the high resolution conductivity distribution of the tissue.

Different magnetic materials such as Fe, Ni, Mn, Co, Cr, and Gd in their metal, metal alloy or oxide forms can be used as magnetic contrast agents [80, 81]. However, because metals and metal alloys are prone to oxidation and corrosion, stable metal oxides are widely used as MNP contrast agents. Toxicity considerations are also a factor in the choice of materials for a contrast agent. The presence of iron in human bodies and the low toxicity profile [82] have led to iron based nanoparticles being actively studied as contrast agents. Other materials that could be highly toxic require proper coating or chelation when used as contrast agent [81].

1.2 Ultrasound Neuromodulation: Actively Transmitting Transcranial Focused Ultrasound Wave for Non-Invasive Brain Stimulation

1.2.1 Non-Invasive Imaging of Brain Networks Perturbed by Low-Intensity Transcranial Focused Ultrasound (tFUS) [83]

Brain activity is distributed over the 3-D space and evolves in time. It is of great importance to be able to image noninvasively brain dynamics and connectomics with high spatial and temporal resolution [84, 85]. Perturbation-based neuroimaging methods [85, 86] combining the light-based or electrical/electromagnetic neuromodulations with a variety of neuroimaging modalities, like electroencephalography (EEG), functional magnetic resonance

imaging (fMRI), and magnetoencephalography (MEG), are valuable tools for understanding the brain networks. Optogenetic neuromodulation, a light-based neuromodulation method, demonstrates excellent spatiotemporal specificity but requires an invasive implantation procedure [87]. Electrical/electromagnetic-based methods, such as the deep brain stimulation (DBS) [88, 89], vagus nerve stimulation (VNS) [90], electroconvulsive therapy [91], transcranial magnetic stimulation (TMS) [86, 92], transcranial direct current stimulation (tDCS) [93, 94], and transcranial alternating current stimulation (tACS) [95] have been pursued to modulate local neural circuits or treat various neurological and mental disorders. Compared to DBS and VNS, TMS and tDCS/tACS have the merit of being noninvasive, but have limited spatial resolution and focality.

Recently, tFUS has been proposed for noninvasive neuromodulation due to its high spatial resolution [96-98]. *In vivo* experiments (in animals) have been reported using a range of ultrasonic parameters achieving either activation or suppression of neural activity. Yoo *et al*. [99] used a rabbit model to demonstrate that tFUS with a fundamental frequency of 690 kHz and spatial-peak temporal-average intensity (I_{spta}) of 6.3 W/cm^2 excites the exposed motor cortex, leading to behavioral manifests such as movement and detectable changes in the recorded electromyography (EMG) signals from subdermal electrodes inserted into forelimb muscle. Blood-oxygen level-dependent signals were already observed through fMRI studies using a lower ultrasound intensity (I_{spta}) of 1.6 W/cm^2, whereas the acoustic stimulation with a spatial-peak pulse-average intensity (I_{sppa}) of 6.4 W/cm^2 lasting for over 7–8 s renders a reduction in the magnitude of the P30 visual evoked

potential (VEP). Low-intensity tFUS (I_{spta}: 300 mW/cm^2) was used by Yoo *et al*. [100] to sonicate the thalamus of anesthetized rats, and as indicated through physiological and behavioral changes, the rats' recovery time was shortened significantly as measured by voluntary movement and pinch response. Using another low-intensity ultrasound stimulation experiment (I_{spta}: less than 13.5±3.8 mW/cm^2, fundamental frequency: 320 kHz), Deffieux *et al*. [101] administered tFUS to the left frontal eye field in two awake macaque rhesus monkeys, and found that tFUS delayed the ipsilateral mean antisaccade latencies compared to the non-sonication case. Most recently, Lee *et al*. [102] targeted the 250-kHz tFUS at the primary sensorimotor cortex and visual cortex of anesthetized sheep, and recorded tFUS-evoked electrophysiological signals using a bilateral EMG and two-channel subdermal EEG system. It was found that the ultrasound intensity I_{sppa} needed to be greater than 6 W/cm^2 to elicit motor evoked potentials and sonication-triggered visual evoked potentials. Minor microhemorrhages in the primary visual cortex were reported which were due to the use of high intensity tFUS, indicating that the ultrasound parameters need to be considered carefully to ensure safe neuromodulatory effects.

In the past years, several groups have applied ultrasound neuromodulation in humans. Hameroff *et al*. [103] harnessed a commercially available ultrasound machine working in standard B-mode to dose chronic pain subjects with transcranial ultrasound (I_{spta}: 152 mW/cm^2 at transducer), and they reported that the subjects' mood were improved for 10 min after the ultrasound mediation. Legon *et al*. [104] examined the effect of pulsed ultrasound stimulation on peripheral

somatosensory circuits by stimulating fingertips. Two ultrasound stimulation waveforms were designed to evoke either mechanical sensation (I_{spta}: 11.8 W/cm^2) or thermal sensation (I_{spta}: 54.8 W/cm^2), and the sonication effects on the neural circuits were indicated by both EEG and fMRI. Later, the group further examined the tFUS (I_{sppa}: 23.87 W/cm^2 at scalp) on sensory-evoked potentials through concurrent EEG recordings [97]. Median nerve stimulations were introduced in this study when the tFUS was administered to the scalp region over the somatosensory cortex. Their EEG recordings showed that tFUS attenuated the amplitudes of the somatosensory evoked potentials, and modulated the spectral content of sensory-evoked brain oscillations. Mueller *et al*. [105] researched the ultrasound-modulatory effect on the EEG phase dynamics of the somatosensory cortex from four-channel EEG recordings. The tFUS (I_{sppa}: 23.87 W/cm^2) altered the phase distribution of intrinsic brain activity in beta-band frequencies and modulated the phase rate of beta and gamma frequencies. Lee *et al*. [106] reported their recent human study, in which tFUS (I_{spta}: 1.5 W/cm^2 at transducer, 350 mW/cm^2 behind the skull) was delivered to the hand region of the somatosensory cortex, using subjects' individual anatomical MR images to guide the transducer over the desired region on the cortex. The participating subjects reported the experienced tactile sensations, while tFUS stimulations were administered. Two-channel EEG recordings from the primary somatosensory cortex revealed that tFUS stimulations were capable of evoking potentials in the hand region of the primary somatosensory cortex, consistent with the subjects' reports (of sensation in the hand).

We will test the hypothesis whether low-intensity tFUS (e.g., I_{spta} < 1 mW/cm^2) can be used as a controlled perturbation to initiate neural activation. We further use electrophysiological source imaging based on multichannel scalp EEG recordings to image tFUS-induced brain activation in an attempt to perturb specific nodes within a brain network under study to determine the role each node plays within the network. The initial results were reported in the BRAIN Investigators Meeting held in December 2015.

1.2.2 Towards the Mechanism of Ultrasound Mediated Neuromodulation through Intracranial Electrophysiological Recordings

For decades, a myriad of brain neuromodulatory approaches, such as deep brain stimulation (DBS) [107], transcranial magnetic stimulation (TMS) [108, 109], transcranial current stimulation (tCS) [110, 111], transcranial focused ultrasound (tFUS) [97, 112, 113], transcranial static magnetic field stimulation (tSMS) [114], optogenetics [115, 116], designer receptors exclusively activated by designer drugs (DREADDS) *etc*., have been developed in order to modulate the brain. Among these methods, optogenetics receives considerable attention for its capacity to selectively stimulation distinct cell-types [117, 118] with high spatial and temporal resolution [116]. However, optogenetics heavily relies on invasive methods such as transgenic approaches or viral vector transfection, which pose practical challenges for translational work in humans [119]. In contrast, TMS utilizes a non-invasive, dynamic magnetic field to achieve facilitation or inhibition of neural activity [109, 120]. A recent pulse shaping technique has also been developed in order to pursue selective neural engagement [121]. Despite the

increasing exploration of therapeutic applications using repetitive TMS [122], the spatial specificity of the applied induced magnetic field is low limiting its precision to modulate specific brain networks. Sharing similar drawbacks, both transcranial direct current stimulation (tDCS) [111], and tSMS [114] have been unable to show elicitation of neuronal action potentials with high spatial precision instead the applied electrical/magnetic field alters the cortical [123] or corticospinal excitability [124]. Recently, transcranial alternating current stimulation (tACS) achieved noninvasive deep brain stimulation when facilitated with a temporal interference technique [125], but its spatial resolution remains to be seen.

As a promising new technique, low-intensity tFUS can be applied in numerous neuromodulation applications due to its high spatial focality (compared to TMS and tCS [126]) and its non-invasive nature [127]. During tFUS neuromodulation, pulsed mechanical energy is transmitted though the skull with high spatial selectivity[97], which can be steered [128] and utilized to elicit activation or inhibition through parameter tuning [129, 130]. Pilot studies have investigated the neural effects of ultrasound parameters, such as ultrasound fundamental frequencies (UFF), intensities (UI), durations (UD), duty cycles (UDC), pulse repetition frequencies (UPRF), *etc*. Besides a few human studies [97, 103, 113], animal models, such as worms [131-133], rodents [83, 112, 130], rabbits [99], swine [134], and monkeys [101], have been utilized to investigate the effects of ultrasonic parameters and acoustic-induced effects through behavioral changes (e.g. motor response), electrophysiological measurements, or blood-oxygenation-level-dependent (BOLD) signal, *etc*. To further achieve selectivity in stimulating

brain circuits or even among cellular populations, focused ultrasound is employed in combination with specific-neuromodulatory-drug-laden nanoparticles [135], cell-specific expression of ultrasound sensitizing ion channels [132] or acoustically distinct reporter genes in microorganisms [136].

Understanding the intrinsic cell-type selectivity of tFUS may be of utmost importance for uncovering the mechanism of ultrasound neuromodulation. Meanwhile, such mechanistic exploration may reduce the tremendous effort in exploring the huge ultrasound parameter space.

1.2.3 The Trends of tFUS-mediated Brain Stimulation

1. Targeting at Deep Brain

As early as 2010, Tufail, *et al*. had successfully demonstrated that low UFF (250 kHz) tFUS with a UPRF of 2 kHz can promote expression levels of brain-derived neurotrophic factor (BDNF) compared to contralateral hippocampal regions [112]. Furthermore, increased neuronal spiking and induced local field potential at the targeted hippocampus provided early but direct evidences of the *in vivo* brain responding to low-intensity tFUS (spatial-peak temporal-average intensity Ispta: 84.32 mW/cm^2). The ultrasound technique allows the tuning of UFF to be higher than 250 kHz, thus achieving a better spatial focus (laterally 1.0 mm, axially 8.5 mm [137]). Kamimura and colleagues [137] targeted 1.9 MHz focused ultrasound (UPRF: 1 kHz, Duty cycle: 50%) to subcortical brain structures, i.e. superior colliculus, pretectal nucleus, and hippocampus *etc*. to trigger reproducible eyeball movement and pupillary dilation. The improved spatial specificity produced by the 7.6-times higher UFF was demonstrated to lead to consistent behavioral

responses comparing to lower UFF scenarios. It was widely recognized that the ultrasound penetration depth largely depends on the skull thickness. Due to this reason, explorations on large animals and humans for targeting ultrasound to the deep brain become highly demanded. Dallapiazza, *et al* administered three UFF levels (1.14, 0.65 and 0.22 MHz) to swine thalamus and demonstrated that low-intensity focused ultrasound (LIFU, 25-30 W/cm^2) can modulate the ventroposterolateral thalamic nucleus and further map the thalamic region with an observed 2-mm spatial specificity evidenced by epidural somatosensory evoked potential (SSEP) as a result of trigeminal, median and tibial stimulations [134]. Continuous 20-Watt power high-intensity focused ultrasound (HIFU) was introduced in this study to verify the ultrasound targeting, and magnetic resonance (MR) thermography was used to monitor the temperature rises in the *in-vivo* brain during both LIFU and HIFU sonications [134]. Legon's group explored the use of tFUS (UFF: 0.5 MHz) modulating human sensory thalamus with scalp SSEP readings [138]. The P14 SSEP amplitude was harnessed as a biomarker of thalamic response to median nerve stimulation (MNS). Both studies reported inhibitory effects induced by the tFUS. Furthermore, researchers have also been exploring the possibility of tagging/modulating the brain signal with ultrasound waves. 2 MHz tFUS (I_{spta}: 1.4 W/cm^2) with a PRF of 1050 Hz was used to tag the living brain signal [139]. Furthermore, demodulated EEG signals share a common feature in gamma band as the signal from direct recordings. The non-invasive acousto-modulated electrophysiological imaging for the human brain has also been conceptualized with EEG/MEG detections [140]. These efforts are expected

to pave a new pathway to map the (deep) brain activity with high spatio-temporal resolution.

2. Pursuing High Spatial Definition

Another trend of the ultrasound neuromodulation investigation is to pursue high ultrasound frequency, thus benefiting the spatial resolution for ultrasound intervention. Among these efforts, 2.9 MHz UFF was directed by Ye, *et al*. [130] to achieve a smaller focal spot of 0.65 mm onto mice motor cortex, and the efficacy of tFUS was evaluated by electromyography (EMG). It was reported that such high frequency ultrasound can still elicit motor responses with increased demand of transcranial ultrasound energy, but the motor outputs were not consistently improved in terms of spatial selectivity as a result of the increased spatial resolution. Two months later, Li and colleagues [141] published their demonstration that 5 MHz tFUS successfully evoked brain activation evaluated with EMG and motion response. With this high UFF, the “equivalent diameter of the the stimulation region” can be further decreased to 0.29 ± 0.08 mm. When comparing to 1 MHz ultrasound, the brain was observed to have shorter response latency for 5 MHz UFF. Undoubtedly, the skull turns to be a significant barrier for the high frequency tFUS. Mehić, *et al*. [98] innovated the ultrasound transducer design to allow two independent elements to be driven by 2.25 MHz and 1.75 MHz UFFs, respectively, and at the focal spot, a beat frequency at 500 KHz carried by a 2 MHz ultrasound wave with 1.5 kHz PRF was eventually utilized to stimulate mice brains in a stepwise scanning fashion. Such modulated focused ultrasound (mFU) were shown to induce a variety of movements with a 1-mm spatial selectivity.

When comparing to another single-element 500 kHz UFF transducer, the mFU was reported to achieve higher fluidity and robustness, but less consistency in triggering the motor movements. This mFU study proposed a temporal interference technique that is able to balance the spatial resolution and acoustic penetration efficiency. On large animals and human subjects, Lee and his colleagues extensively explore the applications of tFUS with the UFF lower than 300 kHz for a better skull penetration. Excitatory effects of the tFUS observed through electrophysiological recordings, functional MR images, participants' reports were achieved on sheep sensorimotor and visual cortices [102], human primary visual [113], primary [106] and secondary somatosensory cortices [142]. tFUS was also harnessed by the group as a medium to transmit sensations between human subjects for composing a brain-to-brain interface. Legon, *et al*. [97] utilized a slightly higher UFF (500 kHz) tFUS aiming at primary somatosensory cortex to modulate the SSEP observed through EEG. An inhibitory effect of this tFUS (spatial-peak pulse-average intensity I_{sppa}: 23.87 W/cm^2) was reported, in which the MNS-induced SSEP's amplitude was attenuated by the mechanical energy. 1-cm spatial specificity was presented, and comparing to the human brain size, the lateral resolution of 4.9 mm was observed to be sufficient for modulating the cortical functional circuits. In contrast, Hameroff, *et al*. [103] reported their pilot study using B-mode low-intensity transcranial ultrasound (unfocused) at 8 MHz to modulate human mental states through the temporal window, and chronic pain subjects' mood and pain scale were improved for at least 10 minutes using such trans-temporal ultrasound.

Chapter 2: High-frequency Magnetoacoustic Tomography with Magnetic Induction (hfMAT-MI) for *In vivo* Cancer Detection

2.1 Introduction

In MAT-MI, a pulsed electromagnetic field is delivered by radio-frequency (RF) coils to induce eddy current in a target volume of conductive tissues. In the presence of an external static magnetic field, the induced current leads to a Lorentz force that drives mechanical vibrations within the ultrasound frequency spanning from hundreds of kilohertz to several megahertz. Such vibrations induce acoustic signals, being subsequently detected by ultrasound transducers. The conductivity distribution can be further retrieved by solving a conductivity reconstruction problem from the acoustic measurement [33, 38], including vectorizing the measurement [143], beamforming the collected ultrasound [45] or modifying the coil setup in a multi-excitation scheme (meMAT-MI) [44]. A series of pilot studies have been conducted on saline phantoms [144] and biological tissues [43], as well as tumor specimens [42]. A reported *ex vivo* experiment on freshly-procured liver tumor specimens has demonstrated the capability of MAT-MI, for the first time, to discriminate the cancerous tissue from its surrounding tissue through conductivity contrast imaging [42]. Despite significant progresses made on MAT-MI, challenges remain, including the limited spatial resolution and the background artifacts.

In this study, we have developed a system for high-frequency magneto-acoustic tomography with magnetic induction (hfMAT-MI) by redesigning the time response function of the conventional MAT-MI system. This function can be

formulated as a convolution of the profile of an electromagnetic pulse and the frequency response function of an ultrasound transducer [40, 41, 145]. Based on this theory, a high-frequency electromagnetic stimulator and an RF coil with low inductance were introduced to shorten and reshape the pulse waveform. Hence, both the center frequency of the pulsed magnetic field and the −6 dB bandwidth were increased by more than three times at the emitting side; these spectral features were then matched by those of the ultrasound transducer at the receiving side. By decreasing the wavelength of both the EM stimulation and its induced ultrasound signal, the axial resolution was enhanced to one millimeter. Besides the improvement of the frequency response, a high lateral resolution was also achieved using a rotational scanning regime with an increased equivalent acoustic receiving aperture of the hfMAT-MI system for *in vivo* applications.

We apply this hfMAT-MI to the *in vivo* imaging of nude mice bearing human breast cancer xenograft hindlimb tumors. We have demonstrated that a 1-mm spatial resolution for electrical conductivity contrast imaging has been achieved by means of hfMAT-MI, largely benefiting inhomogeneous tissue discrimination and early stage tissue anomaly detection [146].

2.2 Imaging Theory

2.2.1 Underlying Physics

Fig. 1 illustrates a conceptual model of MAT-MI. To deliver the stimulation through magnetic induction, a stimulator feeds a coil with a pulsed electrical current $\mathbf{I}(t)$, and a pulsed magnetic field $\mathbf{B}_1(\mathbf{r}, t)$ is thus induced by $\mathbf{I}(t)$ through the object

along the z-direction. According to the Maxwell-Faraday equation, $\nabla \times \mathbf{E}(\mathbf{r},t) = -\partial \mathbf{B}_1(\mathbf{r},t)/\partial t$, this magnetic field leads to an electric field **E**(**r**, *t*) that drives a rotational eddy current **J**(**r**, *t*) in the object depending on the spatial distribution of electrical conductivity σ(**r**). According to Ohm's law, the eddy current is calculated as **J**(**r**, *t*) = σ(**r**) **E**(**r**, *t*), and its spectrum features, including the center frequency and the bandwidth, are determined by those of **I**(*t*). Due to an ignorable displacement current comparing to the magnetic induction current in biological tissues, this magnetic induction process can be described by (1) for a conductive medium based on Ampère–Maxwell equation [33, 34]:

$$\nabla \cdot \mathbf{J}(\mathbf{r},t) = \sigma(\mathbf{r})\nabla \cdot \mathbf{E}(\mathbf{r},t) + \mathbf{E}(\mathbf{r},t) \cdot \nabla \sigma(\mathbf{r}) = 0 \quad (1)$$

where ∇· and ∇ are the divergence and gradient operators respectively. The Lorentz force resulting from the eddy current in the object is given by $\mathbf{F}_L(\mathbf{r},t) = \mathbf{J}(\mathbf{r},t) \times [\mathbf{B}_0(\mathbf{r}) + \mathbf{B}_1(\mathbf{r},t)]$, where $\mathbf{B_0}(\mathbf{r})$ is the z-directional magnetic field by a static magnet [147]. This force translates the electromagnetic pulse into detectable

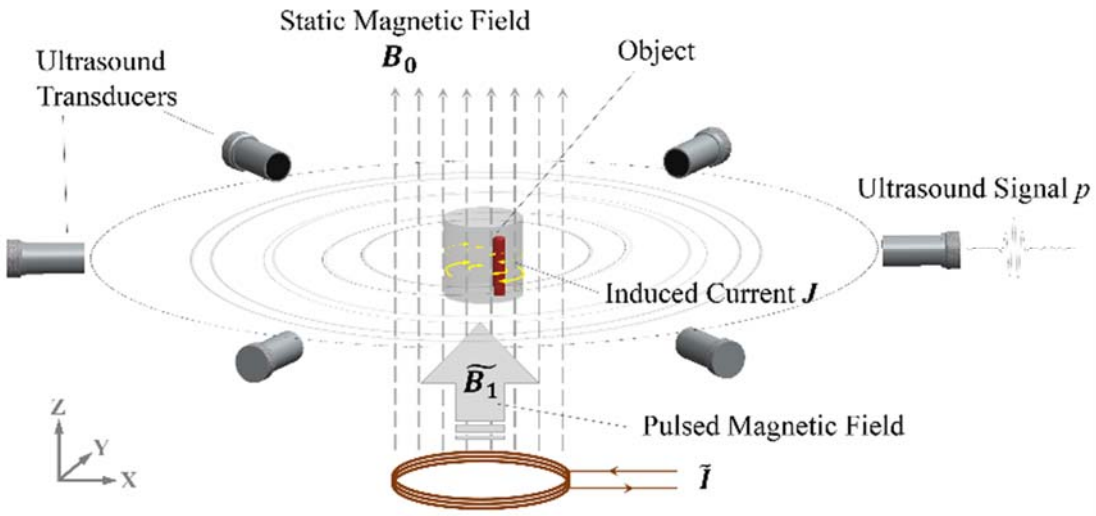

Figure 1. The conceptual model of MAT-MI. (© 2016 IEEE)

mechanical vibrations within an ultrasonic frequency band, which further generate acoustic pressure, $p(\mathbf{r},t)$, detected by ultrasound transducers scanning around the object. In MAT-MI, due to the fact that the physical size of an imaging object (a few centimeters) is far less than the wavelength (on the scale of meters) of the pulsed magnetic field $\mathbf{B_1}(\mathbf{r}, t)$, this magnetic field satisfies the quasi-static condition, allowing the separation of the spatial ($\mathbf{r}$) and temporal (t) components of the aforementioned vector fields [43]. Hence, the wave propagation is described in (2) as:

$$\begin{aligned}\nabla^2 p(\mathbf{r},t) - \frac{1}{c_s^2}\frac{\partial^2}{\partial t^2} p(\mathbf{r},t) &= \nabla \cdot \mathbf{F}_{\mathrm{L}}(\mathbf{r},t) \\ &= \nabla \cdot \left\{ \mathbf{J}(\mathbf{r}) \times \left[\mathbf{B_0}(\mathbf{r}) + \mathbf{B_1}(\mathbf{r}) \right] \right\} f(t)\end{aligned} \tag{2}$$

in which the acoustic source locates at point $\mathbf{r}$, and c_s is the speed of the sound. $f(t)$ is employed here to represent the MAT-MI's time response function. This temporal function can be considered a delta function δ(t) with an unlimited-band hypothesis [143]. In a limited-band system, however, $f(t)$ is the convolution of the magnetic stimulation's waveform $S(t)$ and the ultrasound transducer's impulse response $R(t)$, i.e. $f(t) = S(t) * R(t)$ [40, 41, 145]. The observed pressure signal at the detecting location $\mathbf{r_d}$ can be obtained by solving the differential equation (2) using the Green's function [148] as in:

$$\begin{aligned}p(\mathbf{r_d},t) = -\frac{1}{4\pi}\int_{\mathrm{V}} \nabla_{\mathbf{r}} \cdot \left\{ \mathbf{J}(\mathbf{r}) \times \left[\mathbf{B_0}(\mathbf{r}) + \mathbf{B_1}(\mathbf{r}) \right] \right\} \cdot \\ \cdot \frac{f(t) * \delta(t - |\mathbf{r_d} - \mathbf{r}|/c_s)}{|\mathbf{r_d} - \mathbf{r}|} d\mathbf{r}.\end{aligned} \tag{3}$$

As a solution for the forward problem of MAT-MI, (3) can be used to simulate the pressure temporal profiles at different detecting locations. After either calculating the pressure signals using (3) in computer simulations or collecting

those signals using ultrasound transducers in experiments, the inverse problem can be solved using a time reversal approach in order to reconstruct the acoustic sources [33], as shown in:

$$\nabla \cdot \mathbf{F}_{\mathrm{L}} \approx -\frac{1}{2\pi c_s^3} \iint_{\Omega} \frac{\cos\theta}{|\mathbf{r_d} - \mathbf{r}|} p''(\mathbf{r_d}, |\mathbf{r_d} - \mathbf{r}|/c_s) d\Omega \tag{4}$$

Ω is the ultrasound detection surface, θ is the angle between the normal vector of Ω at $\mathbf{r_d}$ and ($\mathbf{r_d}$ **-** $\mathbf{r}$), and p'' is the second time derivative of acoustic pressure collected at a transducer location. With (4), the acoustic source can be reconstructed and further used to delineate the conductivity contrast in the object.

2.2.2 Spatial Resolution

For a two-dimensional image, its spatial resolution comprises of lateral and axial components. In a conventional ultrasound imaging approach, the 3 dB lateral resolution depends on the acoustic wavelength and the system's F-number [149]. In MAT-MI, a circular scanning method is used, and when the stepping angular distance is less than or equal to the diameter of the transducer, the lateral resolution of the MAT-MI imaging system can be determined by:

$$w_{3\mathrm{dB}} = \lambda \cdot F\# = \lambda \cdot 1/\varphi \tag{5}$$

in which φ is the scanning view measured in radians, and λ is the acoustic wavelength. The circular scanning approach used in MAT-MI leads to a much smaller *F#* than that of conventional ultrasound imaging. Using a scanning angle larger than 60° in MAT-MI, the calculated 3 dB lateral resolution is better than one wavelength.

For the axial resolution, unlike the pulse-echo regime in conventional ultrasound systems, MAT-MI passively detects acoustic signals with ultrasound transducers. Thus, its axial resolution can be calculated by [149]:

$$d_{ax} = \lambda \cdot M \tag{6}$$

in which *M* is the number of oscillations of the emitting EM stimulation that contributes to the center frequency, and in pulse-echo ultrasound imaging, *M* would be more than one to have this axial resolution equal to several wavelengths. In order to improve the axial resolution, the system's time response needs to be shortened. By further applying the quasi-static condition and the Biot-Savart law integrated over a circular current loop [150] with a diameter of *D*, for a specific location *a*, (7) shows a dependence of the time response function on the waveform of the pulsatile electrical current **I**(*t*) flowing through the coil and the transducer's impulse response:

$$f(t)\big|_{a,D} = \frac{\partial B_1(t)\big|_{a,D}}{\partial t} * R(t) = Q(a,D)\frac{\partial I(t)}{\partial t} * R(t) \tag{7}$$

where Q(*a*, *D*) incorporates the first and second kind of complete elliptic integral functions [151]. The oscillation number *M* should be as small as 1.

2.2.3 Computer Simulations

To test the image resolution that can be achieved by hfMAT-MI through computer simulations, as indicated in Fig. 1, the static magnetic field is pointing in the z-direction and assumed to be uniform through the imaging area with the flux density of 1 Tesla. One set of Helmholtz coils with a diameter of 100 mm and 4 turns is located in the xy plane at z = 50 mm and z = -50 mm respectively. The transient current amplitude is set to be 10 kA/s and the scanning radius is 200 mm.

The center frequency of the transducer is 2.25 MHz, and the data sampling frequency is set to be 20 MHz. Simulated impulse response for 2.25 MHz ultrasound transducer in both time and frequency domains are illustrated in Fig. 2a-b. To test the capability of the high-frequency MAT-MI in resolving small objects and discriminating adjacent regions assigned with different conductivities, a simulated phantom is shown in Fig. 2c for finite element analysis (FEA, based on PDE toolbox in MATLAB), with the smallest structure and gap between structures having the size of 1 mm. From the comparison of acoustic source reconstructions in Fig. 2d-e, the detail structures are seen to be better resolved by the 2.25 MHz hfMAT-MI than the image results produced by 500 kHz system, in regard of reconstructing original object sizes with high fidelity and separating structures close to each other (Fig. 2f). The better spatial resolution achieved by the hfMAT-MI would further allow itself to be applied as a diagnostic tool for breast cancer.

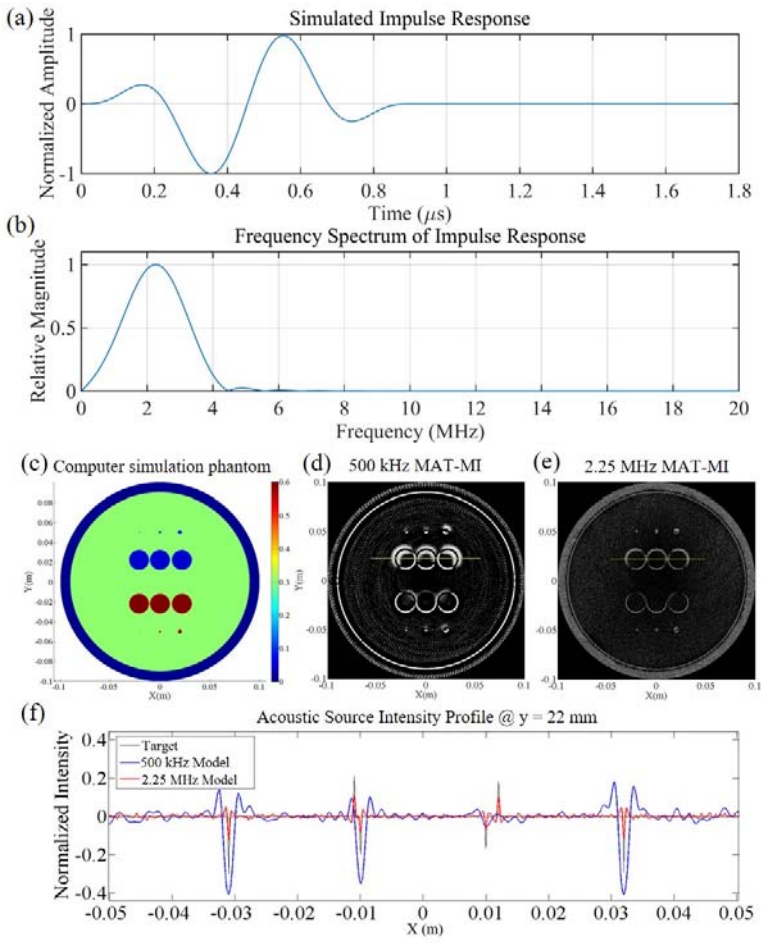

Figure 2. Computer simulations of high-frequency MAT-MI (hfMAT-MI). (a)-(b) The simulated impulse response of 2.25 MHz ultrasound detection; (c) Simulation phantom with its conductivity (S/m) distribution for spatial resolution test; (d)-(e) Regular MAT-MI (500 kHz) and 2.25 MHz hfMAT-MI acoustic source reconstructions; (f) Line profiles of the acoustic source intensities along y = 22 mm indicated by green lines in (d) and (e).

The hfMAT-MI concept can also be integrated with the multi-excitation scheme. In such an integration (Fig. 3b), besides the conventional Helmholtz coils, another two sets of figure-8 coils are needed to generate the pulsed magnetic field (B_1) along x and y axes and meanwhile the injected current I ($1x10^4$ A/s) is required to be shorter. This shortened current waveform will increase the center frequency

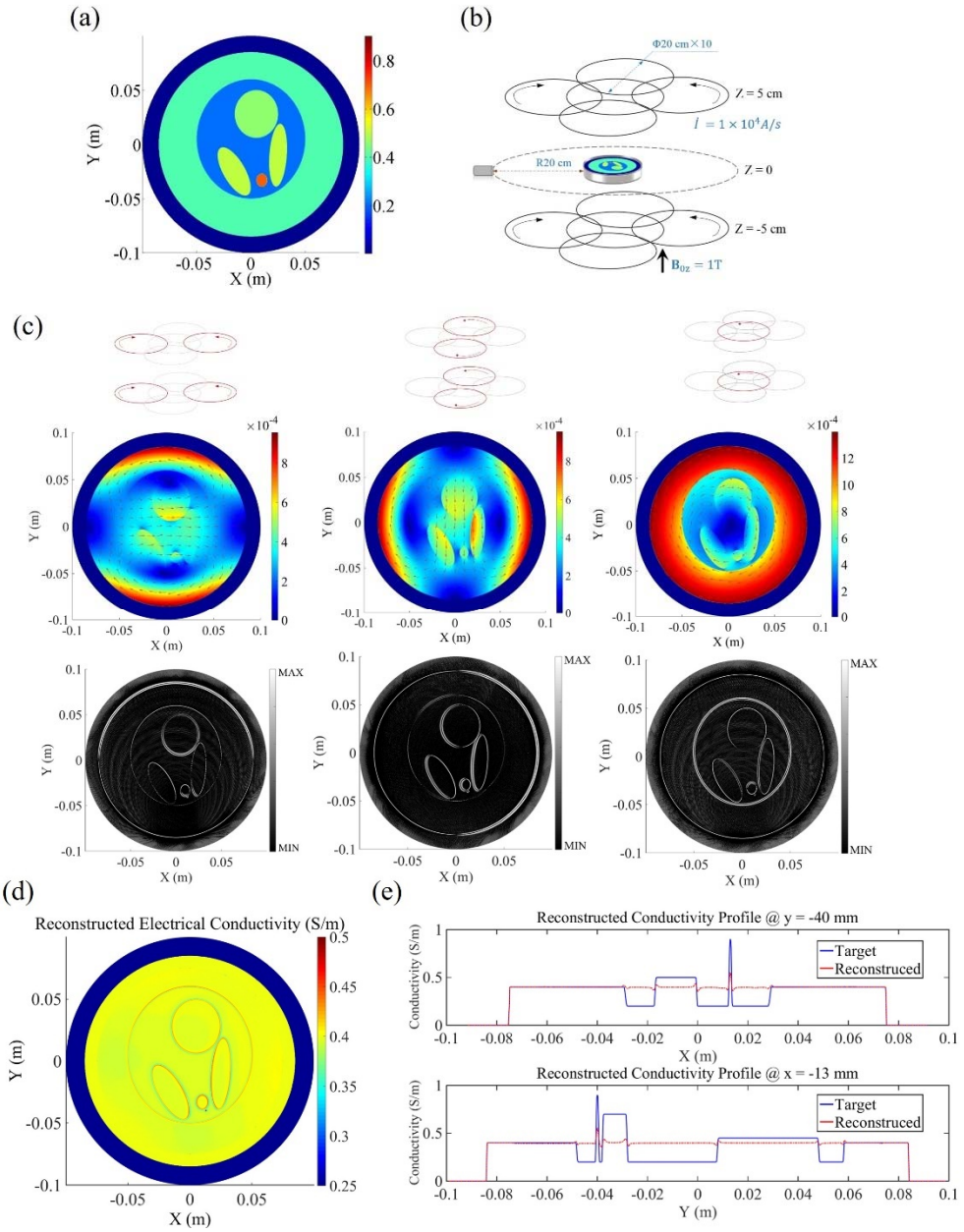

Figure 3. Computer simulations of high-frequency multi-excitation MAT-MI (hf-meMAT-MI). (a) Original simulation phantom to test hf-meMAT-MI. (b) The imaging setup of hf-meMAT-MI. (c) Three stimulation patterns and their corresponding induced eddy current distributions, and respective acoustic source reconstructions. (d)-(e) The reconstructed electrical conductivities and line profiles.

of the induced B_1, and further require a high-frequency, matched ultrasound detections. To elucidate how the hf-meMAT-MI works, Fig. 3c depicts the

stimulation patterns along three axial directions, the induced eddy current distributions, and respective acoustic source reconstructions (all based on FEA). Based on these intermediate computations, the electrical conductivities of the simulation phantom (Fig. 3a) are subsequently reconstructed as in Fig. 3d. The line profiles compare the original and the reconstructed results, and it can be observed that the hf-meMAT-MI can still detect the boundaries of conductivity

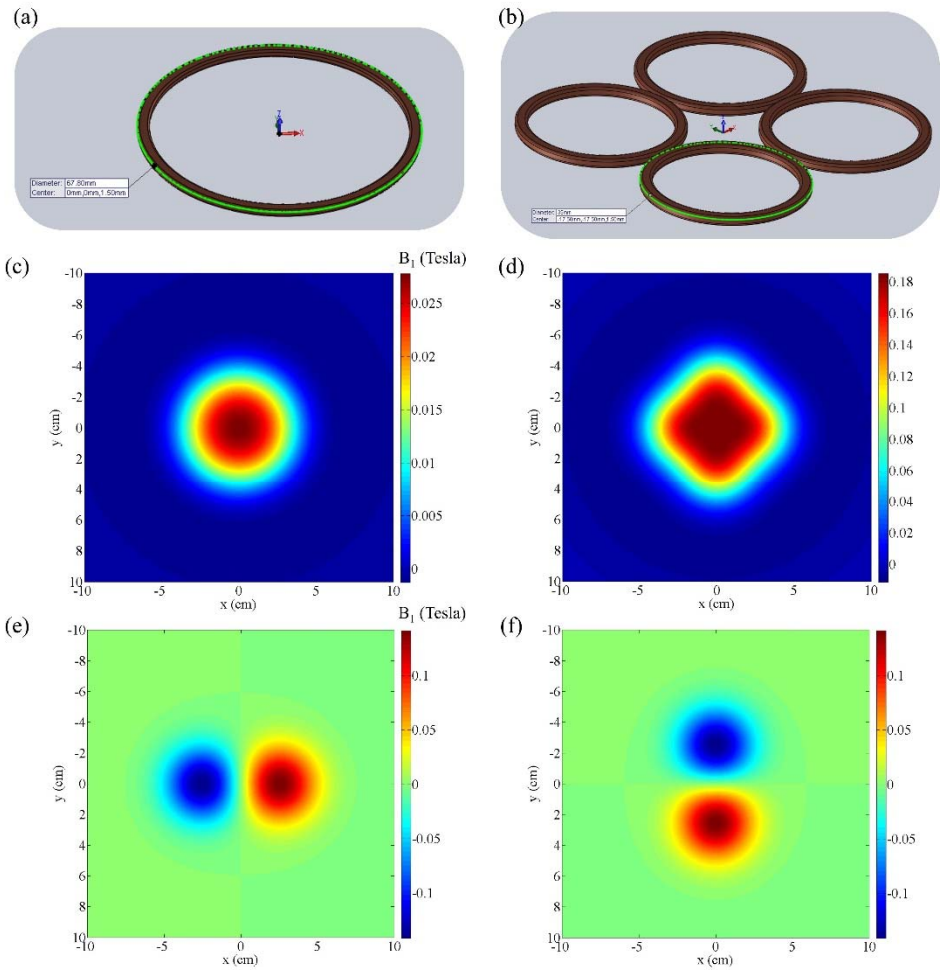

Figure 4. Computer simulations for coil geometries. (a) A single coil with a diameter of 67.8 mm. (b) A coil array constitutes of 4 small coils with a diameter of 35 mm. (c-d) The magnetic flux densities generated by corresponding coil(s) at 30 mm away from the coil planes. (e-f) The multi-excitation capability by the coil array.

change, but the reconstruction of boundary-enclosed region suffers the major relative error (0.21). Overall, the correlation coefficient is 0.94. These results indicate that to recover the internal conductivity distributions may still need further adjustments on, for instance, the relative sizes between the coil and the object. The sizes of these simulation phantoms are designed to be commensurate with human breasts, whereas making the coils large enough to cover the region of interest may raise a practical challenge of a dramatically increased inductance as stated by the Wheeler formula,

$$L = \frac{r^2 \cdot n^2}{8r+11w} \tag{8}$$

in which r is the radius to center of windings, n is the turns, w is the width of widings, and L is the inductance of the coil. Hence, this would further challenge the pulsed current source unit and high-voltage switch. For an application in the hfMAT-MI, the size of a coil needs to be balancing between imaging coverage and the coil inductance. A coil array configuration may be a solution to meet such needs (Fig. 4b, d) and additionally, the array may also provide multiple excitations (Fig. 4e, f) shown as in Fig. 3c.

2.3 Materials and Methods

From the computer simulations, the major advantage of hfMAT-MI is its unprecedented spatial resolution in the magnetoacoustic imaging. In order to validate the imaging resolution in physical gel phantom, we compare the boundary-resolving capabilities between a hfMAT-MI system (2.25 MHz) and the previously utilized 500 kHz system [38, 41, 152]. The reconstructed acoustic source images

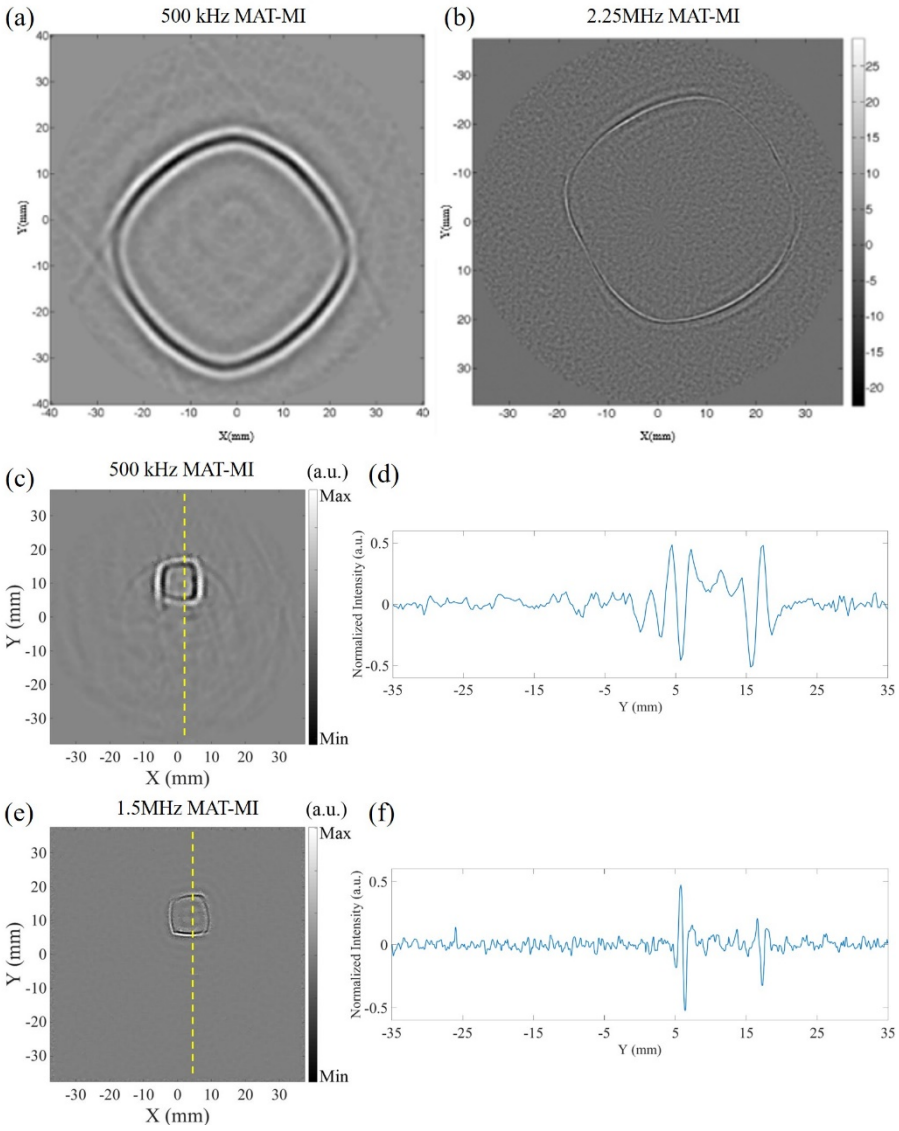

Figure 5. Comparisons on imaging spatial resolutions. (a-b) A resolution comparison between 500 kHz MAT-MI (a) and 2.25 MHz hfMAT-MI models (imaging object is a 20% saline agar phantom). (c-f) A comparison on imaging spatial resolutions provided by 500 kHz MAT-MI (c) and 1.5 MHz hfMAT-MI (e) (imaging object is a square-column phantom with 1.5% salinity). The edges of the object are resolved with a 3-mm (d) and 1-mm (f) spatial resolutions respectively. (c-f © 2016 IEEE)

from the same saline agar phantom are shown in Fig. 5a-b. It can be observed that the 2.25 MHz MAT-MI, with its spatial resolution of about 0.7 mm, resolves the

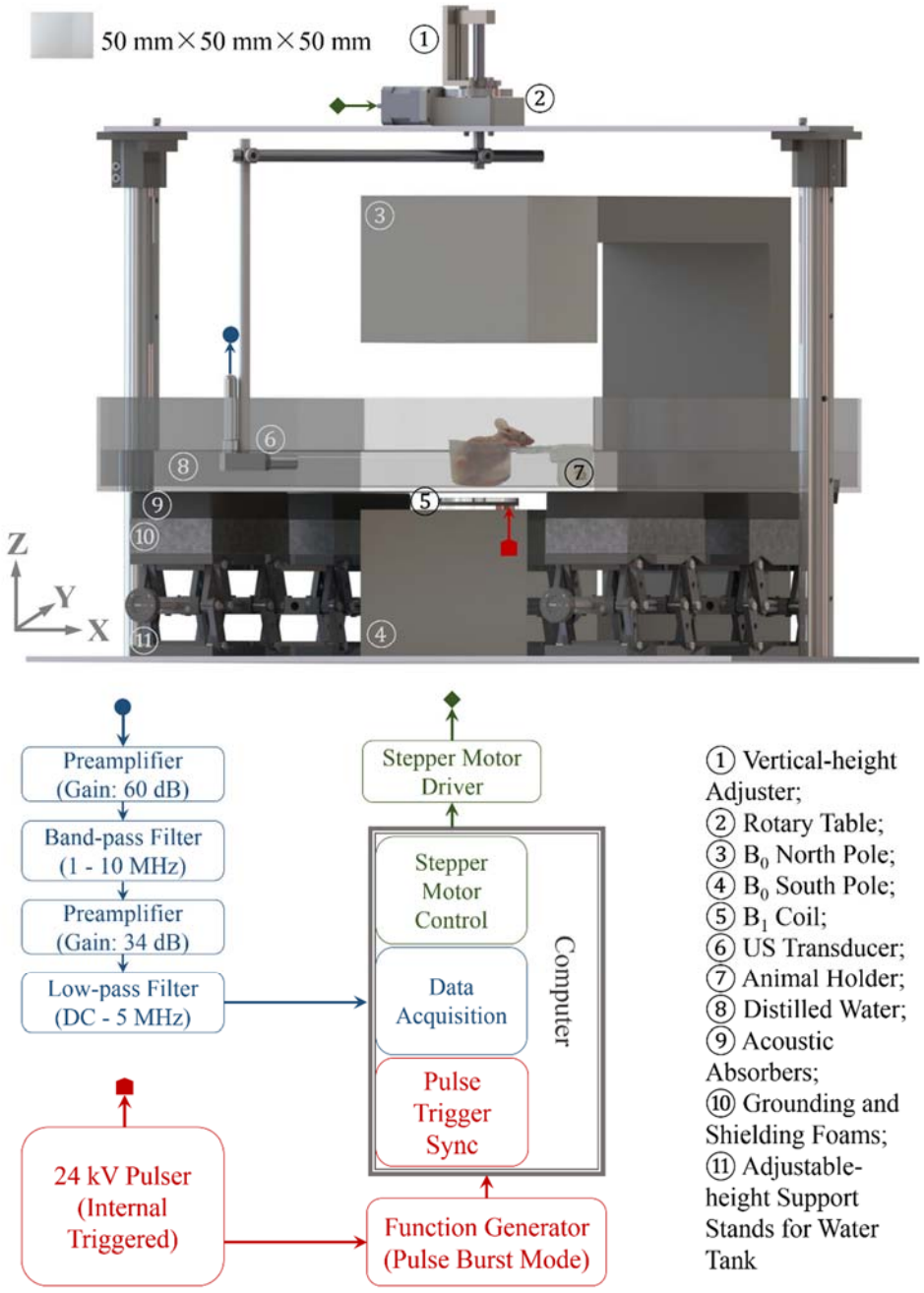

Figure 6. The experimental system of the hfMAT-MI. (© 2016 IEEE)

phantom boundary more precisely than that from 500 kHz system. From Fig. 5a-b, it can be also seen that the image contrast of 2.25 MHz MAT-MI image is lower than that produced by the 500 kHz system (both systems are powered with 440V

current source), and this is due to the increase in center frequency of magnetic induction, the pulsed current in the coil decreases which reduces the magnetic stimulation significantly according to the Biot and Savart law. For this reason, 1.5 MHz hfMAT-MI imaging system was developed to pursue biological tissue imaging while receiving benefits from improved spatial resolution without sacrificing excessive image contrast. A high voltage source, 25 kV is designed to power this 1.5 MHz hfMAT-MI for a stronger B_1 field and reduced averaging times, thus shortening the scanning duration, particularly in the *in vivo* imaging applications.

2.3.1 Imaging System

Fig. 6 presents the hardware setup for the hfMAT-MI experiments. The sample is placed on the x-y plane and is immersed in distilled water serving as the acoustic coupling medium ($c_s \approx 1.5$ mm/μs). To produce the high-frequency pulsed magnetic induction for biological tissue imaging, a customized high-power high-frequency stimulator (Applied Pulsed Power, NY, USA) equipped with half-cycle stimulation technique (Fig. 7(a)) is used to feed a low-inductance coil (65 mm diameter, 800 nH inductance) up to 25 kV, and to minimize ringing effects. As presented in Fig. 7(a), the duration of each current pulse is configured to be 680 ns by the stimulator in order to have a -3 dB bandwidth of 1.3 MHz with a center frequency at 1.5 MHz for $\partial B_1(t)/\partial t$, i.e. the induced rotational electrical field (Fig. 7(b)), in spectrum. The stimulator initiates triggering and synchronizes with a high-speed, multi-channel data acquisition card (CSE8482, Dynamic Signals LLC, IL, USA), which collects ultrasound signals at sampling frequency of 12.5 MHz to

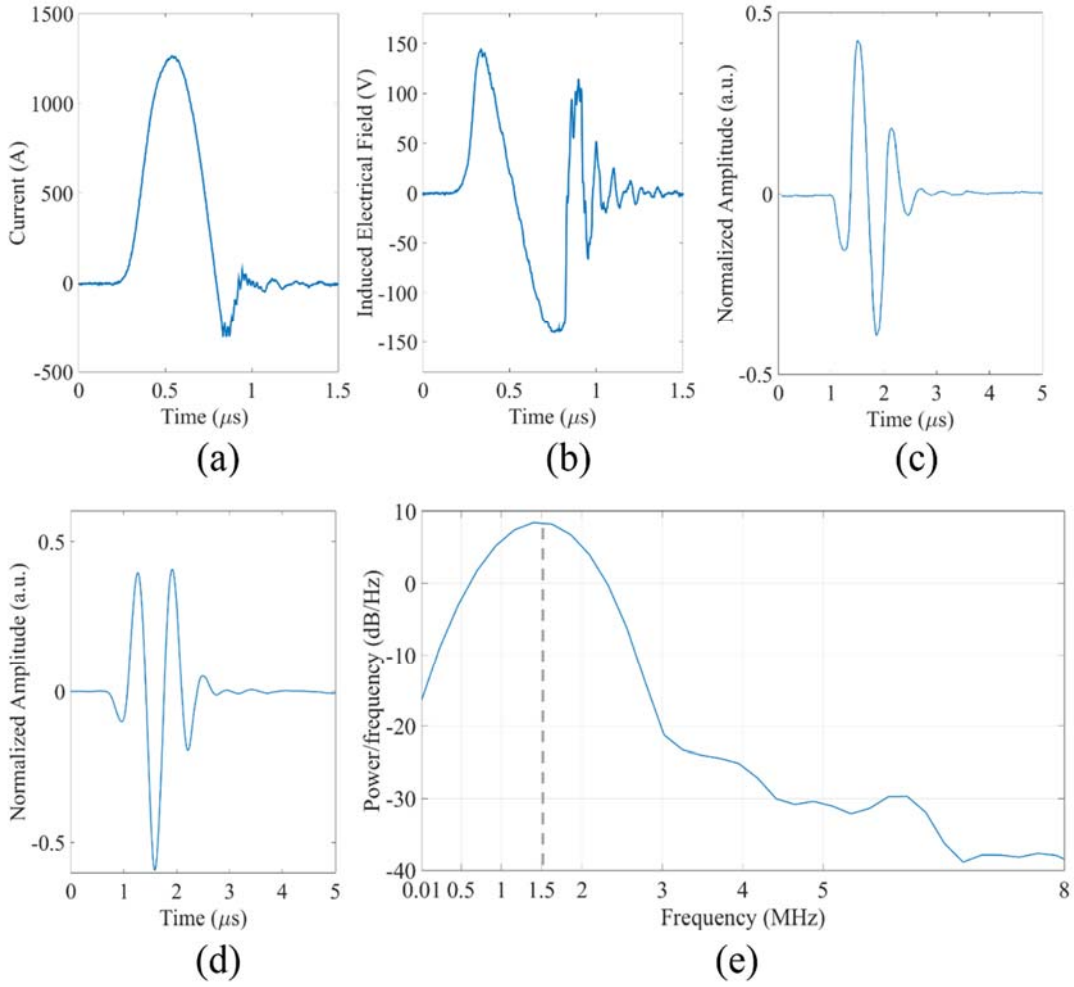

Figure 7. Characterizations of electromagnetic stimulation and ultrasound detection. (a) The waveform of the injected pulsed current **I**(t) having a pulse duration of 680 ns; (b) the waveform of the induced electrical field detected by a probing coil (radius: 10 mm) at a transverse plane 30 mm away from the coil; (c) the normalized waveform of the ultrasound transducer's impulse response; (d) the calculated time response function f(t) of the hfMAT-MI system; (e) the Welch's power spectral density estimate of f(t), whose center frequency is located at 1.5MHz. (© 2016 IEEE)

record 4096 data points at each sampling. To detect the MAT-MI signals, the ultrasound transducer of the hfMAT-MI system is a customized single-element flat-immersion type with a diameter of 14.2 mm, a nominal center frequency of 1.5 MHz, and a -6 dB fractional bandwidth of 76.85% (Olympus NDT, MA, USA). Fig.

7(c) presents the impulse response of the ultrasound transducer, and the detected acoustic signal is amplified by two-stage ultra-low noise ultrasonic preamplifiers with a -3 dB bandwidth of 0.05-2 MHz (5662, Olympus NDT, MA, USA), then is filtered by a homemade band-pass filter (1-10 MHz) and a low-pass filter (BLP-5+, Cain-Forlaw, NY, USA). The transducer mechanically scans around the sample driven by a rotary table (B5990TS, Velmex, NY, USA). This rotational actuator is fed by a programmable stepper motor controller (VXM-1, Velmex, NY, USA). In addition to steering of the rotary table in the x-y plane, the transducer's vertical location is set by a manual adjuster to align the detecting aperture with the ROI. The hfMAT-MI system console software is programmed using LabVIEW 2013 (National Instruments, TX, USA).

In Fig. 8(a), the ultrasound gain map [152] is simulated by the Field-II software [153]. In order to use a uniform ultrasound gain and also create time delay for MAT-MI signals separated from the electromagnetic pulse, the ultrasound scanning radius is set to be 160 mm in experiments, and the line profile in Fig. 8(b) depicts the gain along the lateral direction 160 mm away from the surface of the transducer. Further, using the current amplitude shown in Fig. 7(a) and the coil's inductance value, a simulated magnetic flux density of this pulsed magnetic field 30 mm away from the coil based on the Biot-Savart law is demonstrated in Fig. 8(c) and its center line profile is shown in Fig. 8(d). With regards to the static magnetic field, a customized NdFeB permanent magnet dipole (Dexter Magnetic Technologies, IL, USA) is used to provide a static magnetic field of 0.3-0.6 Tesla in a 160 mm × 200 mm × 180 mm sample space, as shown in Fig. 8(e)(f).

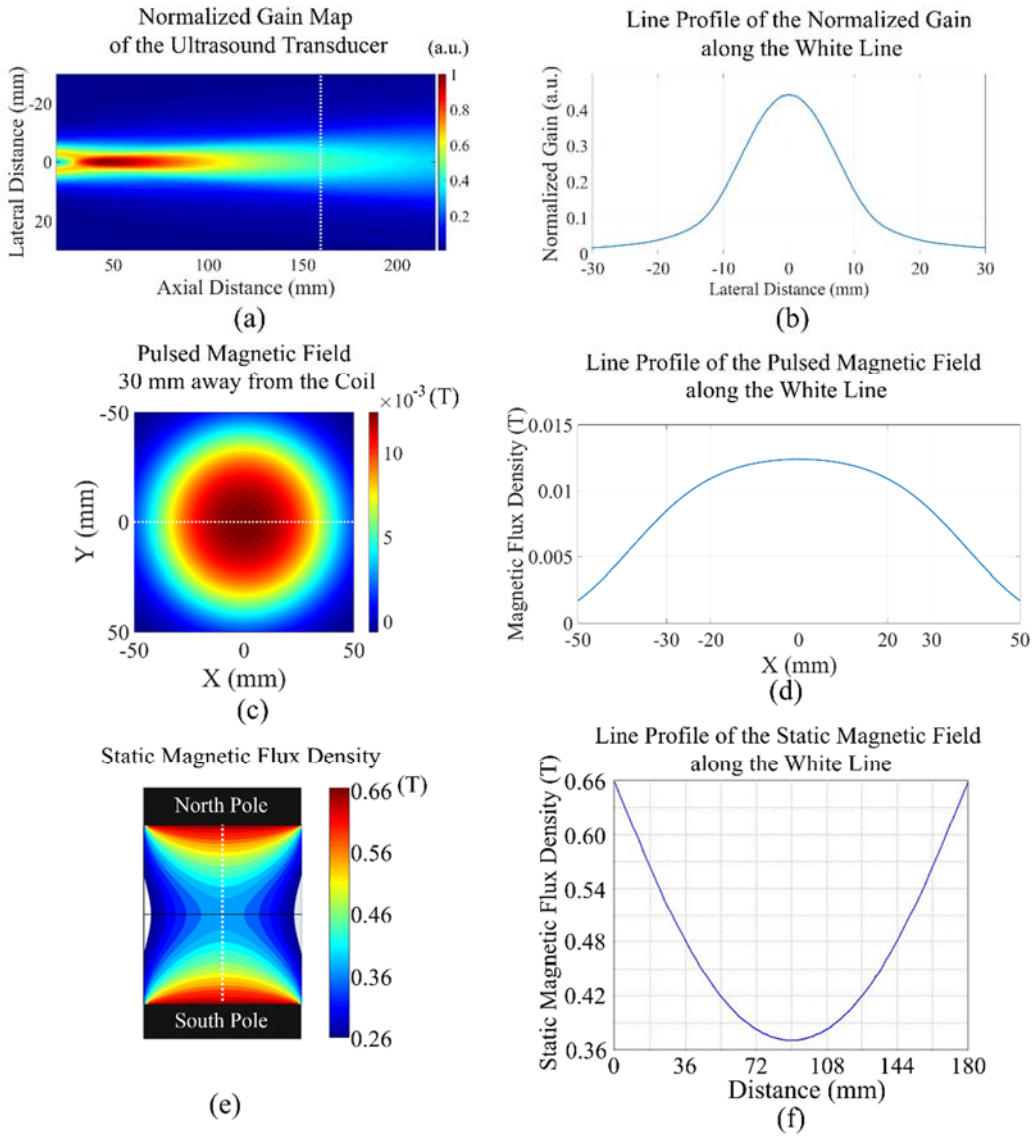

Figure 8. Characterizations of major physical fields in hfMAT-MI. The simulated gain map of the ultrasound transducer is shown in (a) and (b); the simulated pulsed magnetic flux density B1 30-mm away from the coil is shown in (c) and (d); and the simulated static magnetic field B0 formed by the dipole is presented in (e) and (f). (© 2016 IEEE)

2.3.2 Image Co-registration

For anatomical referencing, a 64-channel pulse-echo ultrasound system (OPEN system, Lecoeur Electronique, Chuelles, France) was employed to image the region of interest, including the tumor region, at different heights within the animal. This ultrasound system incorporates a 64-element phased-array transducer (P7-4, ATL), whose center frequency and bandwidth are 5 MHz and 3 MHz respectively. The ultrasound data were then acquired with a synthetic aperture (SA) method. Using SA beamforming and time-reversal algorithms [154, 155], an ultrasound pulse-echo image of a corresponding cross section was obtained. Considering the ultrasound images as reference, feature-based method was used to register the images obtained from hfMAT-MI, and this feature was the visible animal plastic holder in both imaging modalities.

To further delineate internal structures within the tumor, histology was conducted after the *in vivo* imaging studies. The histology images were used to co-register the electrical conductivity contrast images obtained from the hfMAT-MI by aligning affiliated skin tissues. After the mouse was euthanized, the tumor was excised together with its surrounding tissues, and was fixed in 10% formalin solution for 48-72 hours before transferring to 70% ethanol. The sample was then sent to the Biological Materials Procurement Network at the University of Minnesota for further dehydration, paraffin embedding, and sectioning. Hematoxylin and eosin (H&E) stain was thereafter applied to blue cell nuclei and pink cytoplasm. After the preparation of multiple slides, 40× magnification images were obtained by a digital microscope (ScanScope XT digital slide scanner, Leica

Biosystems, IL, USA). The histologic images were then processed by Aperio ImageScope (Leica Biosystems, IL, USA).

2.3.3 Mouse Tumor Model

Metastatic human breast carcinoma cell line MDA-MB-435A was used in this study. The cells were cultured in Dulbecco's DMEM (Modified Eagle Medium, with 584 ml/l L-Glutamine, 4500 mg/l D-Glucose and 110 mg/l Sodium pyruvate, Corning Inc., USA), supplemented with 10% FBS (Fetal Bovine Serum, Gibco, USA), Pen Strep (100 U/ml penicillin and 100ug/ml streptomycin, Gibco, USA) and 0.0675 μg/ml human insulin (Sigma-Aldrich, USA). Cells were maintained under 37°C and 5% CO_2. Next, cells were sub-cultured by applying 0.05% trypsin-0.53 mM EDTA (Invitrogen, USA) for 5 minutes to detach the cells when reaching 70% in flasks. Cells in log phase of growth (50-60% confluent) were then harvested for tumor inoculation. These cells were rinsed, centrifuged and re-suspended by IMEM (Improved MEM without phenol red, serum or other supplements, Gibco, USA) twice, onto 2×10^7 cells/ml cell suspensions.

All animal procedures and care were approved by the University of Minnesota Institutional Animal Care and Use Committee (IACUC) in accordance with federally approved guidelines. Female nude mice (6-8 weeks, Athymic Nude-Foxn1nu, Harlan Laboratories Inc., USA) were injected with 5×10^6 cells subcutaneously over the dorsal flanks near the hind limbs under general anesthesia. Experiments were performed throughout the 1-8 weeks after tumor seeding when tumor diameter was between 2-15 mm.

2.3.4 *In vivo* Experiments

After anesthetized by intraperitoneal injection with a mixture of Ketamine and Xylazine (100 mg/kg and 10 mg/kg respectively), 1/2 original volume dose was given immediately before the hfMAT-MI imaging to extend the sedation period. The mouse was placed in a sitting posture inside an equivalent-sized plastic holder. 37℃ agar gel was then used to fill the plastic holder to provide good ultrasound coupling, maintain the animal's position, and situate the tumor region 1.5-2 cm away from the coil. 1.5% salinity [43] was introduced into this agar gel, so the animal holder could be also seen in hfMAT-MI images, facilitating co-registration with ultrasound pulse-echo images.

During hfMAT-MI imaging, the ultrasound transducer scanned around the animal with a step size of 1.2°, covering a 180° imaging view. At each detecting channel, the signal was averaged over 175 acquisitions using a pulse repetition rate of 8.5 Hz. Thus, one *in-vivo* imaging trial with hfMAT-MI took approximately 60 minutes. A heating system including a submersible aquarium heater, an air vortex heater, and a thermostat was employed to achieve an ambient temperature of approximately 36 ℃, to keep the mouse from losing body temperature during anesthesia. After the *in vivo* imaging with hfMAT-MI, the 64-channel ultrasound system was used to conduct SA scans for the mouse in the plastic holder at a series of layers with increments of 1.5 mm along the z direction, i.e. Δz = 1.5 mm. Then, the mouse was taken out from the plastic holder, wiped dry and placed on a heater pad. Next, the tumor size was measured using a caliper before the mouse

was recovered from anesthesia. This mouse was then sent back to its cage after restoring its motion capability.

2.3.5 Electrical Conductivity Measurement

A homemade device, as shown in Fig. 9, was developed to directly measure the electrical conductivity of biological tissues at the same center frequency of hfMAT-MI. The device employed four unipolar needle electrodes [43, 156] (EL450, BIOPAC Systems, CA, USA) with 1-mm tips exposed without polytetrafluoroethylene (PTFE) coatings. These electrodes were linearly and equally distributed (Spacing: 1.1 mm) on a PTFE beam. The conductivity measurement is based on Ohm's law. After the motion system physically inserts

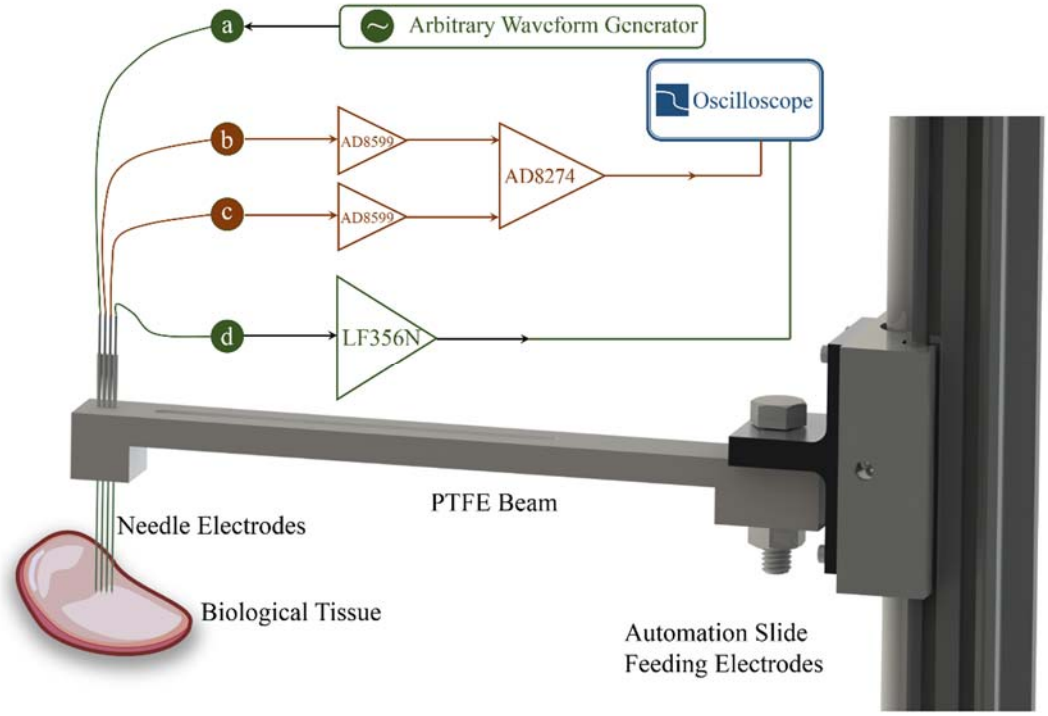

Figure 9. The schematic diagram of the four-electrode device for electrical conductivity measurement of biological tissues. (© 2016 IEEE)

the electrodes into a specific location of the tissue, an arbitrary waveform generator (33220A, Keysight Technologies, CA, USA) was then used to inject sinusoidal electrical current (P-P Voltage: 200 mV, frequency: 1.5 MHz) via electrodes *a* and *d* into a target location of the tissue. This current was monitored by a current-to-voltage converter, employing a JFET input operational amplifier (LF356N, Texas Instrument, TX, USA). Simultaneously, the voltage across the electrodes *b* and *c* was detected by a high-speed instrumentation amplifier incorporating a dual-channel ultralow-noise operational amplifier (AD8599, Analog Device, MA, USA) and a precision difference amplifier (AD8274, Analog Device, MA, USA). Thus, both the amplitudes of the current and voltage were displayed and measured with a digital oscilloscope (DSO7014A, Keysight Technologies, CA, USA). As a result, the local conductivity was estimated. Before measuring conductivity values in the animals of interest, the device had been calibrated using saline solutions with known conductivities. Invasive conductivity measurements were taken immediately after euthanizing the mouse through cervical dislocation.

2.4 Results

2.4.1 Imaging Quality

The spatial resolution can be represented by the lateral and axial resolution, both of which depend on the acoustic wavelength of hfMAT-MI from equations (5) and (6). This wavelength can be calculated from $\lambda = c_s / f_0$, where f_0 is the center frequency of the acoustic pressure field $p(\mathbf{r_d}, t)$. This center frequency, 1.5 MHz, is

determined by the Fourier transform of the time response function $f(t)$ as shown in Fig. 7(e), leading to the acoustic wavelength $\lambda = 1$ mm.

In our *in-vivo* experiment using 1.5 MHz hfMAT-MI, the ultrasound transducer scanned 180° ($\varphi = 3.14$ rad) around the object of interest, resulting in a lateral resolution w_{3dB} of 0.32 mm, whereas from Figure 3(b), the oscillation number (M) of the EM stimulation that contributes to the center frequency is 1. This leads to an axial resolution of $d_{ax} = 1$ mm. Therefore, the overall imaging spatial resolution is determined by this 1-mm axial resolution. To compare the spatial resolutions of the 1.5 MHz hfMAT-MI and previous 500 kHz MAT-MI [34, 38, 43, 157], Fig. 5(c)(e) demonstrates each method's performance in imaging an identical agar phantom prepared in a square column. As indicated in this comparison, not only can the imaged edges of the object be reduced from 3 mm to 1 mm as shown in Fig. 5(d) and (f), but the EM artifacts were also suppressed approximately 6 dB more using the hfMAT-MI, compared with conventional MAT-MI. Both improvements are essential for reliable conductivity imaging of biological tissues. The capability of EM artifacts suppression is mainly due to engineering upgrades in ultrasound detection, magnetic stimulation, and power system design.

2.4.2 *In vivo* Tumor Imaging

Fig. 10 presents an *in-vivo* imaging study for a tumor bearing mouse. The tumor has been propagated at one of the mouse's hindlimbs for 8 weeks, with the size reaching about 1.5 cm^3. The sedated mouse maintained a sitting posture in the plastic holder as shown in Fig. 10(a) and (b). Three slices in the z-direction marked with three dashed lines were selected and imaged by the ultrasound with

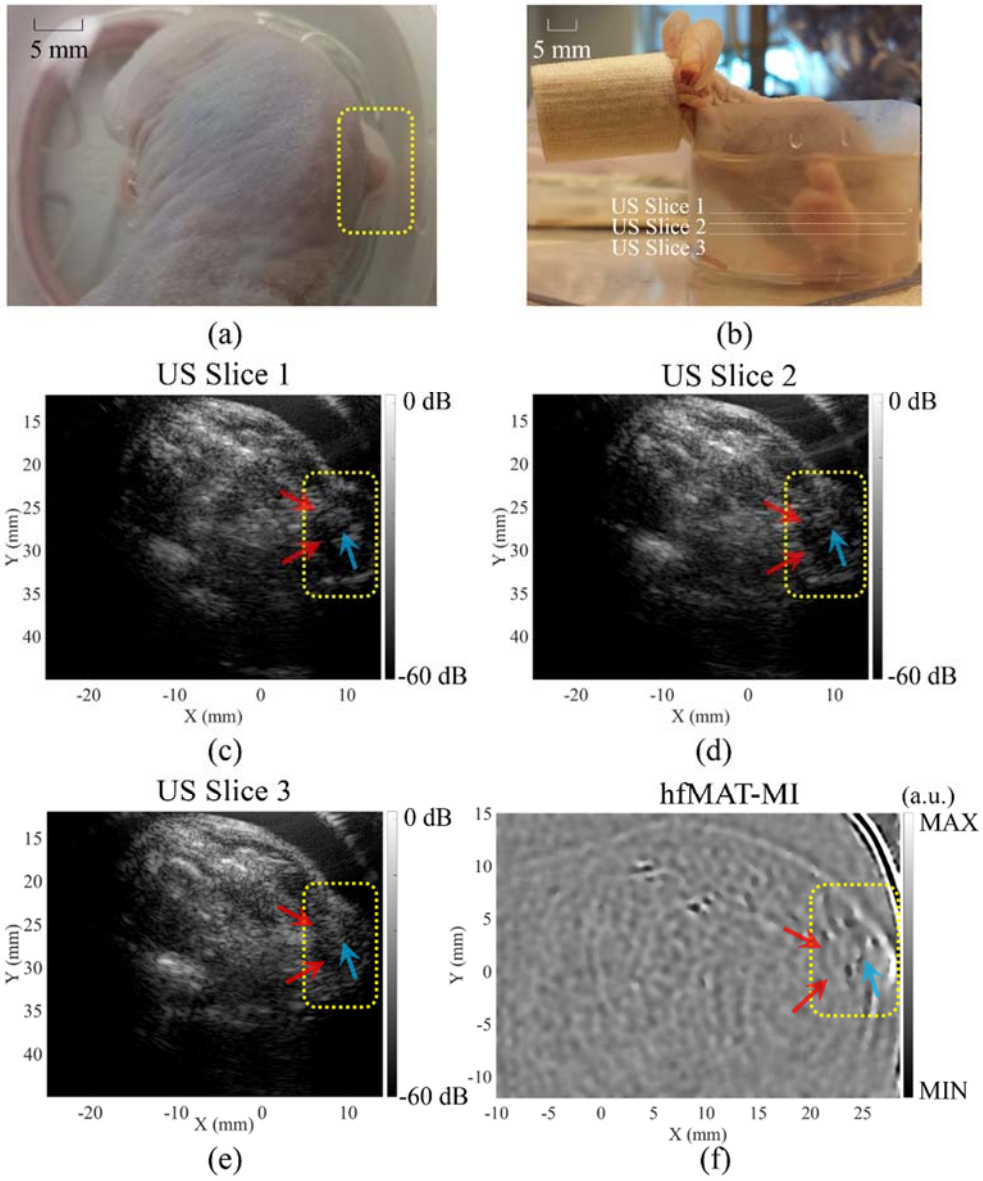

Figure 10. An *in-vivo* imaging study of a tumor-bearing mouse. (a) The top view; (b) the side view, with three ultrasound scanning slices (c)(d)(e) indicated by three white lines; (f) the *in-vivo* image produced by the hfMAT-MI. The yellow boxes represent the propagated tumor region, the red arrows indicate the tumor-muscle interfaces, and the blue arrows indicate the tumor's inner structures, e.g. necrotic core. (© 2016 IEEE)

a phased-array probe, which is also covered by the piston transducer in the hfMAT-MI. A two-millimeter space step among those slices was achieved by controlling

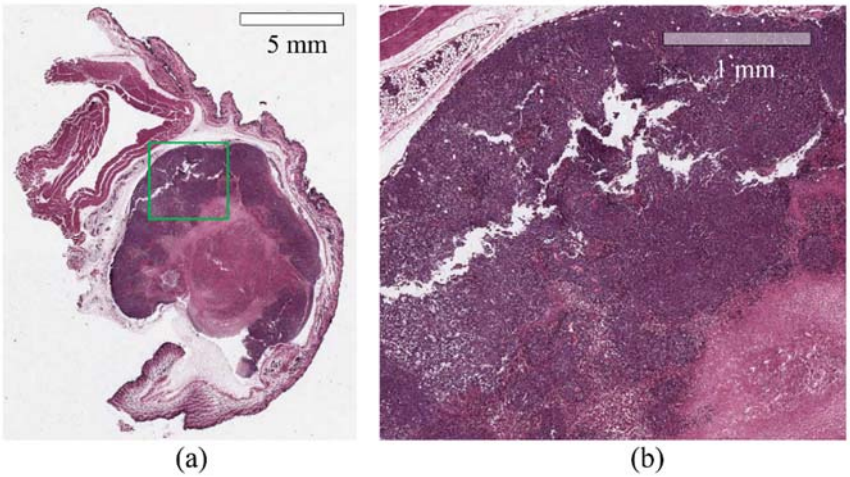

Figure 11. Histological studies of a tumor sample. (a) A histological slide of the tumor using the H&E stain; (b) an enlarged view of the histological region marked by the green box in (a), in which the purple region shows distinguishable features from its surrounding region in pink. (© 2016 IEEE)

the translation stage. The corresponding ultrasound SA images in Fig. 10(c-e) represent cross-sectional views at different heights (z direction) of the same tumor-bearing mouse. The tumor regions are enclosed with yellow boxes, while inner boundaries (i.e. the boundaries between the tumor and internal structures of the rest of the mouse body) of the tumor are detected by the ultrasound system and indicated by red arrows. Fig. 10(f) is an electrical-conductivity contrast image using the hfMAT-MI, in which a complete contour of the same tumor is depicted. Taking the advantage of its 1-mm spatial resolution, conductivity variations inside the tumor are visualized by the hfMAT-MI image as well. These internal tumor structures can also be observed in the ultrasound images, as indicated with blue arrows. To further co-register these variations, a histology study of the tumor sample followed the hfMAT-MI and ultrasound imaging experiment. Fig. 11 shows

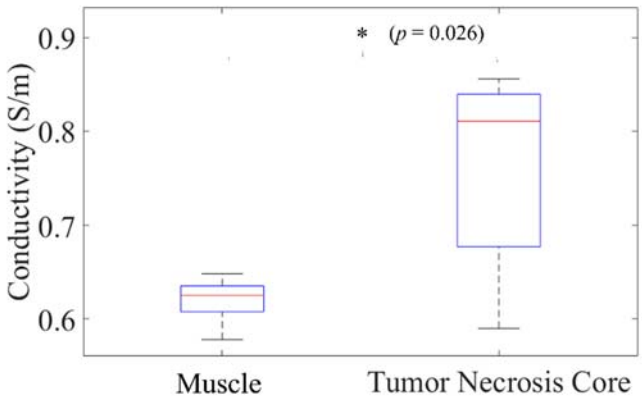

Figure 12. The conductivity (measured by the four-electrode device at 1.5 MHz) comparison between the mouse muscles and the tumor necrosis core. (© 2016 IEEE)

the histological slides using the H&E stain. A necrotic core as the pink, surrounded by a "ring-shaped" dark-purple region, can be seen in Fig. 11(a).

Electrical conductivity measurements at 1.5 MHz using the four-electrode device gave a mean of 0.76 S/m (five sample locations) for the necrotic core, compared to a mean of 0.62 S/m (five sample locations, measured along a transverse direction to the muscle fibers) for the tumor's adjacent muscle, shown in Fig. 12, with a statistically significant difference between the two groups ($p < 0.05$) based on a paired sample *t*-test. As shown in the dark purple in Fig. 11(b), which is an enlarged view from an ROI marked by the green box in Fig. 11(a), the tumor's ring-shaped peripheral solid layer, due to its limited thickness, only one sample location can be identified and measured by inserting the four electrodes. And the measured electrical conductivity for this peripheral layer is 0.44 S/m. From these measurements, the conductivity contrast inside the tumor was greater than that of the muscle-tumor interface.

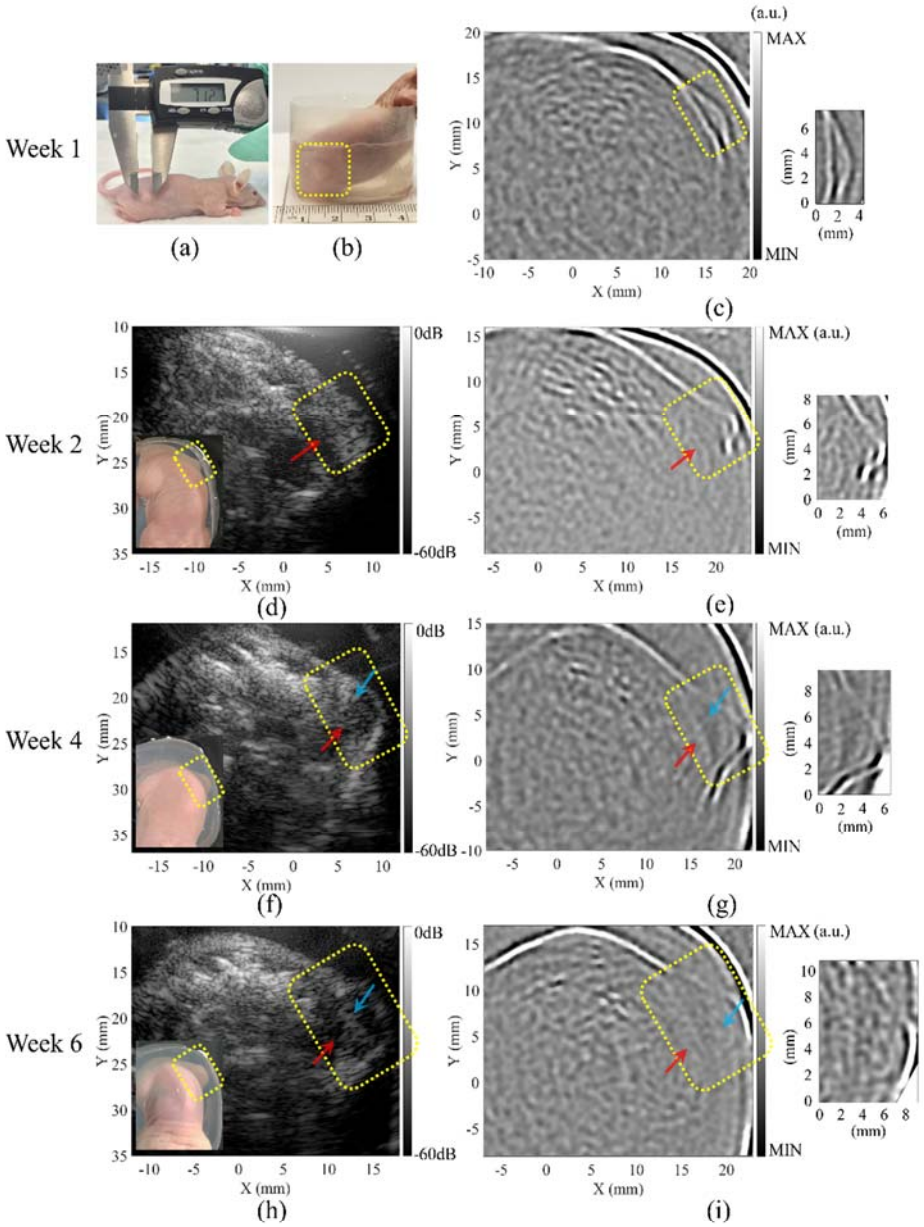

Figure 13. An *in-vivo* mouse model study tracking the tumor growth. (a)(b) The tumor appearance in the 1st week after a transplantation of the human cancer cell line. (d)(f)(h) are the ultrasound images of the tumor-bearing mouse in the 2nd, 4th, 6th weeks, and the insets in these three images show the tumor growth in top views. (c)(e)(g)(i) are the hfMAT-MI images of the mouse abdomen and its growing tumor in the 1st, 2nd, 4th, 6th weeks respectively, and more specifically, the sizes of the growing tumor can also be estimated. The yellow boxes represent the regions of the growing tumor, the red arrows indicate the tumor-muscle interfaces, and the blue arrows indicate the tumor's internal structural change, e.g. necrosis. (© 2016 IEEE)

2.4.3 Tumor Growth Monitoring

In order to leverage its improved spatial resolution, we used hfMAT-MI to image and monitor a growing tumor in a separate mouse over the course of several weeks. Yellow boxes are used to mark the tumor regions in Fig. 13. As shown in Fig. 13(a), the tumor grew into a “disk-like” protrusion two weeks after the transplantation of the breast cancer cells. At this early stage, the diameter of the protrusion was about 7 mm, and the height was less than 2.5 mm. Preparation of the mouse (1 week after the tumor implantation) for *in-vivo* imaging with hfMAT-MI is shown in Fig. 13(b), with the resulting image shown in Fig. 13(c). This image highlighted the small tumor at one hindlimb of the mouse. A significant electrical-conductivity contrast can be seen between this newly developed tumor and its adjacent muscle tissues. This distinct electrical-conductivity boundary (blue arrow) indicates that the propagated tumor is restricted subcutaneously. The 2-mm height of the tumor can be also estimated from the reconstructed image.

Along with tumor growth, we started to use the ultrasound SA image to co-register the electrical-conductivity boundaries detected by hfMAT-MI for the same mouse. Fig. 13(d) and (e) display *in-vivo* images of the mouse tumor during the second week. An inset at the left-bottom side of Fig. 13(d) is a top-view of the mouse during imaging, and a yellow arrow indicates the tumor region. The geometry of the tumor changes and becomes a small “lump”. However, the ultrasound pulse-echo imaging appears less sensitive to the second-week tumor compared with hfMAT-MI, because the ultrasound image does not explicitly differentiate the tumor region from its surrounding soft tissues, while the image

from hfMAT-MI preserves and highlights the tumor “lump”. Moreover, Fig. 13(e) shows that the tumor-muscle interface (blue arrow) starts to lose the high contrast obtained in images from the first week. When the tumor entered into its fourth week, its size had approximately doubled compared to the two-week mark. In Fig. 13(f), some of the tumor boundaries start to evolve in the ultrasound image, whereas a sharp boundary is detected using hfMAT-MI, depicted in Fig. 13(g). In addition, both sets of images reveal that the tumor gets less homogeneous over time in terms of both the acoustic characteristics and the electrical properties of the tumor tissue, reflecting internal structural change related to tumor necrosis. The red arrows in Fig. 13(f) and (g) point to the suspected necrotic region of interest. At the sixth week, boundaries of the tumor were more apparent than previous observations in the ultrasound image shown in Fig. 13(h). However, similar to the weak signal from the tumor-muscle interface introduced in Fig. 10(f), the electrical-conductivity contrast was decreased on the margin (blue arrow), shown in Fig 13(i). By the fourth week, besides the expansion of the tumor’s external geometry, its internal structure had become even more complicated, as more conductivity variations are apparent in the hfMAT-MI images. At this late stage, a necrotic core (red arrow) had developed inside the tumor, which was also co-registered with histology. The electrical conductivity of the tumor was also measured using the four-electrode device before the tumor sample was sent for the histology study. By taking three measurement sites in the tumor, the conductivity ranged 0.53 – 0.6 S/m.

2.5 Discussion

Tissue conductivity imaging using MAT-MI was proposed in 2005 [33] with a sonography-comparable spatial resolution. In the present study, for the first time, we present the equations for quantifying the 2-D MAT-MI imaging spatial resolution. Previously, by applying Rayleigh criterion, a spatial resolution of 1.51 mm was claimed through parallel-line-source phantom experiments, which used a high-power magneto-acoustic system with a center frequency of 460 kHz [41]. In the present study, we have demonstrated that by using high-frequency pulsed magnetic induction and its coupled acoustics, we can achieve a spatial resolution of 1-mm while obtaining reasonable contrast measurements compared with existing MAT-MI methods [41-43, 76]. To compare the spatial resolution with the reported value in [41], the minimum resolvable spatial detail using hfMAT-MI is as small as 0.53 mm if applying Rayleigh criterion. More specifically, the 2-D MAT-MI imaging spatial resolution is divided into the axial and lateral resolutions. We show that both of them depend on the frequency response of the imaging system. Furthermore, by using rotational scanning in MAT-MI, the 2-D imaging spatial resolution appears to be determined only by the axial resolution. This may not be true for applications using limited views, in which the lateral resolution may become the “bottle neck”. It is also worthwhile to note that both the element size of an ultrasound transducer and the distance from this transducer to an imaging object can affect the sensitivity and the imaging resolutions, among which the elevational resolution is another fixed property of the transducer to resolve structures in the z-

direction and should be considered in a 3-D imaging case. In our 2-D imaging work, as the transducer uses a single round, flat sensing element, its elevational specification is similar to the simulated line profile in Fig. 4(b) (W_{3dB} = 12 mm). This 12-mm specification is used to align the transducer with the ROI, i.e. transplanted tumors. To improve this z-directional resolution, focused ultrasound transducers or an acoustic lens [158] can be used. In summary, this work addresses significant technical challenges of *in vivo* magneto-acoustic imaging and paves the way for future work in early detection of cancer using hfMAT-MI.

In this *in-vivo*, small-animal breast-cancer model study, we have shown the capability of MAT-MI in discriminating tumors from normal tissues, identifying internal tissue structures and tracking tumor growth for the first time. The imaging contrast mechanism (i.e. conductivity difference) was verified by measuring fresh tumor and its neighboring muscles with our lab-made device. The propagated tumor in Figs. 8 and 9 had been grown for 8 weeks on one mouse subject, and the resulted tumor in Fig. 10 was on another mouse, with Figs. 10(h)(i) and 11(a) showing the tumor images in week 6. Comparing these two cases, the late stage of the tumor was proved to have high inhomogeneity of electrical conductivity, and the tumor necrotic core expressed much high conductivity value due to its fluidic state with decreased cell membrane structures seen from histology results and increased ion concentration in extracellular space. Besides, we also found that when the tumor was grown for 6 weeks as imaged in Fig. 10(h)(i), the electrical conductivity contrast decreased at the tumor-muscle interface. This phenomenon may be explained by an observation when doing tumor anatomy after euthanizing

the mouse subject; as a result, we noticed that the tumor had very close tissue connections to the adjacent muscle (photos not included), whereas such tissue connection was relatively loose, and gradually getting close during the initiative four weeks after tumor transplantation, and this was verified using another two mice respectively sacrificed in week 2 and week 4. Further cancer biology study is needed to understand the mechanism.

Through the *in vivo* experiments, as small as a 20% conductivity difference was able to be imaged with our hfMAT-MI system. In clinical breast cancer imaging, better contrast (the conductivity measured at 1.5 MHz of a developing breast tumor is 10 times higher than that of normal breast adipose tissues [4]) may be presented, which would make our magneto-acoustic imaging method more sensitive in depicting the margin of a breast tumor. However, further tests are needed to address more complicated structures in the human breast than those in an animal model. Despite this challenge, the potential of distinguishing breast cancer tissue from healthy tissues makes hfMAT-MI a promising imaging tool for assisting diagnosis of early-stage human breast cancer. One significant improvement of hfMAT-MI compared with conventional methods is its increased sample space (Fig. 2) between the magnetic dipole, allowing one human breast to be fit into the imaging setup without any difficulties. Moreover, an improved hfMAT-MI system employing multiple receiving ultrasound transducers is also being developed to dramatically shorten the 2-D imaging time down to 10 minutes, which is beneficial when considering subject's comfort in potential clinical applications. Overall, besides the intrinsic merits of MAT-MI, such as being non-invasive, good imaging

depth, and inherent immunity to the “shielding effect” [33], this work demonstrates the integration of tissue electrical-conductivity imaging with pulse-echo ultrasound imaging to provide both structural and functional information for the first time. This combination suggests the feasibility of integrating hfMAT-MI with conventional ultrasound imaging for multi-modal, early diagnosis of human breast cancer. The high-frequency technique introduced in hfMAT-MI also lays a foundation for further detecting the anisotropic property of biological tissues with the 1-mm spatial resolution. The multi-excitation MAT-MI technique have been validated through 2D experiments [44] and 3D trials [158]. Besides reconstructing the conductivity distribution, the multiple coil sets and the corresponding algorithms introduced by the multi-excitation research can also be used to compute the conductivity gradients along both x and y directions, and potentially along z direction if ultrasound elevational resolution can also be further improved.

Compared to other clinically-available imaging modalities, the imaging contrast of hfMAT-MI still needs to be further improved. One approach would be to introduce a strong static magnetic field to address this issue. In fact, several pilot imaging tests on pork phantoms have been conducted employing a 9.4T MRI magnet and a 500 kHz high-power stimulator [159]. Besides the increased costs, the system assembly of MAT-MI in an MRI machine is still challenging for *in vivo* experiments. Another potential approach is to redesign the RF coil that generates the pulsed magnetic field. hfMAT-MI could utilize low-inductance coils to form a large coil array, allowing an even higher current amplitude flowing through than that achieved in Fig. 3(a). This improvement on the coil engineering is believed,

on the one hand, to increase the pulsed magnetic flux density, thus inducing a stronger instantaneous electrical field than that presented in Fig. 3(b). On the other hand, this would expand the effective imaging area, effectively reducing the inhomogeneity of the pulsed magnetic field. Due to the short rise time (less than 1 μs) and the low peak magnetic flux density (less than 0.1 T at 30 mm away from the coil), the current level and waveform employed in hfMAT-MI is believed to be safe avoiding nerve stimulation.

In the present study, breast cancer bearing mice were used as a cancer model. Tumors were induced by injecting MDA-MB-435A (LCC6) cells into the hindlimbs of the mice. This cell line is an ascites model of MDA-MB-435, which was derived at M.D. Anderson Cancer Center, Houston, TX, USA in 1976 from the pleural effusion of a 31-year-old female with metastatic, ductal adenocarcinoma of the breast [160]. Ever since, the MDA-MB-435 cell line has been in extensive worldwide use among established laboratories as a model for human breast cancer. The xenograft tumor formed in immune-deficient rodents (e.g. T-cell deficient athymic nu/nu mice) not only retains genetic and phenotypic properties of its human counterparts, but also serves as a cost-effective *in vivo* model for understanding tumor biology and mimicking critical elements of disease progression [161, 162]. However, even though breast cancer cell lines and their *in vivo* studies provide considerable insights into breast carcinoma, a few cell lines are not enough to characterize all types of human breast cancer with distinct features [163]. As for the MDA-MB-435 cell line used in this study, questions have been raised that gene expression analysis of the cells produced some microarrays

in which MDA-MB-435 clustered with cell lines of melanoma origin [164-166]. We are aware of the debate about the origin of this cell line [167] and despite these speculations, strong evidence has been presented reiterating that MDA-MB-435 is of breast cancer origin [168] and may be used as “an excellent model for studies of highly malignant and dedifferentiated breast cancers” [165]. However, we realize that discussions concerning the cell line’s genetic origin are outside the scope of this paper, which focus more on demonstrating the capability of high-resolution *in vivo* imaging of cancer using conductivity contrasts. More work has been planned on testing with *in-vivo* models using different cancer cell lines as well as procured human breast cancer samples.

Chapter 3: Contrast-enhanced Magnetoacoustic Imaging with Magnetic Nanoparticles

3.1 Introduction

The contrast presented by MAT-MI can be further enhanced by introducing the magnetic nanoparticles, thus leading to a high sensitive detection of cancerous tissue. Recently, several ultrasound-based nanoparticle imaging techniques have been introduced in which a secondary effect of the nanoparticles is being used to indicate their presence. Magnetoacoustic tomography (MAT) is an imaging modality used to reconstruct the distribution of magnetic nanoparticles (MNPs) based on acoustic pressure induced from magneto motive force. In this method, we apply a short, microsecond duration magnetic pulse to the tissue with MNsP. This leads to a short pulsed magneto motive force acting on the MNPs which gives rise to acoustic vibrations that spread throughout the medium. These acoustic vibrations are at the same frequency as the dynamic magnetic field, which is chosen to match the ultrasound frequency range. This allows recording of these acoustic waves with ultrasound transducers which are placed around the object. This measured signal can then be used to reconstruct the acoustic source distribution in the object by using possible ultrasound imaging approaches which leads to the reconstructed images having a good resolution of the ultrasound imaging method and good imaging depth in soft tissue. In the present study, we demonstrate our work on *in-vivo* imaging of the iron oxide based nanoparticles (IONP). The particles are chosen to be small (10 nm) which leads to these particles

having superparamagnetic properties. This allows the particles to have good stability in colloidal solutions. Using these particles with a concentration of 4 mg Fe/ml injected into the LNCap prostate tumor propagated over the hind limb of the mouse, we have performed *in-vivo* imaging of these nanoparticles. These *in-vivo* tumor images are co-registered with ultrasound imaging and demonstrated the MAT method's capability to assess IONP's presence and distribution in the tumor.

3.2 Imaging Theory

3.2.1 Magneto-acoustic Signal Generation

In magneto acoustic tomography based iron oxide nanoparticle detection, a time varying magnetic field $\boldsymbol{B_1}(\boldsymbol{r}, t)$ is applied over the object space Ω. This field is generated by applying a pulsed current through coils placed in the xy plane as seen in Fig. 14, and this gives rise to magnetic fields which are primarily along the z direction over the object space. Also, when the applied current pulse duration is in the micro second range, the corresponding magnetic field is in the MHz frequency range. In biological tissue, such a field can uniformly penetrate through the object and can be considered to be quasi static [45, 169] and fully determined by the coil geometry carrying the pulsed current. This allows the separation of the spatial and temporal components of the magnetic field as follows

$$\boldsymbol{B_1}(\boldsymbol{r}, t) = \boldsymbol{B_z}(\boldsymbol{r})\, f(t) \tag{9}$$

Where $\boldsymbol{B_z}$ is the magnetic field acting along the z direction in space, $f(t)$ is the time dependence of the field. The magnetic nanoparticles present in such a field

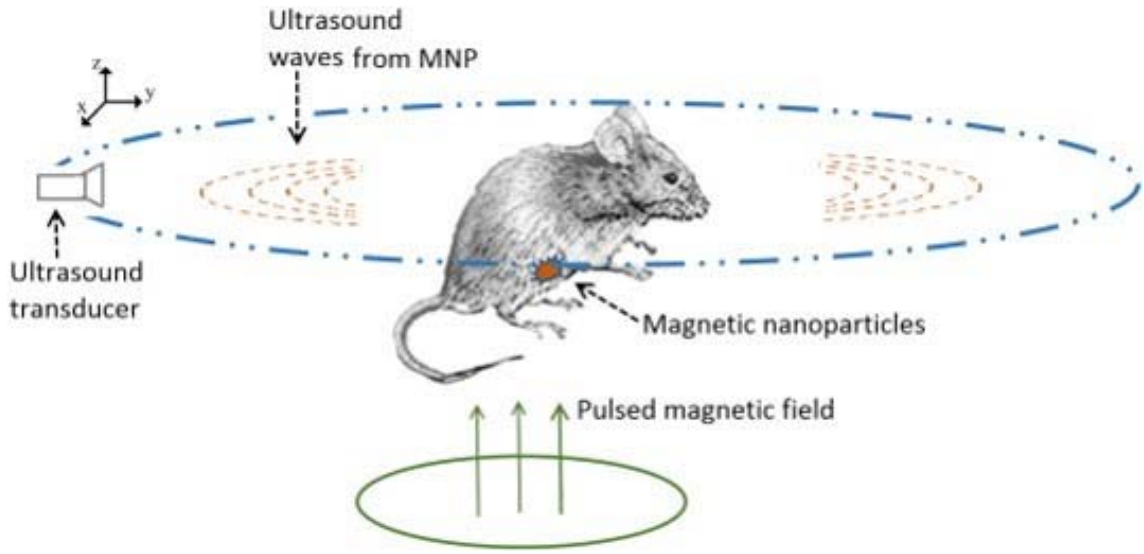

Figure 14. Schematic diagram of magnetic nanoparticle imaging using magneto acoustic tomography method with a short pulsed magnetic field. (© 2016 Elsevier)

experience the magneto-motive force along the **z** direction as described by the following equation [74, 170]:

$$\boldsymbol{F_m} = \frac{\chi_{np} V_{np} f_{np}}{\mu_0} B_z \frac{\partial \boldsymbol{B_z}}{\partial z} f(t), \tag{10}$$

Where χ_{np} is the magnetic susceptibility of the particles, V_{np} is the volume of the nanoparticles and f_{np} is the volume fraction of the nanoparticles and μ_0 the magnetic permeability constant.

For a biological tissue medium behaving as a inviscid fluid, the linearized Navier-Stoke's equation describing the relationship of the pressure wave and the applied force is as follows [22, 39, 69]:

$$\rho_0 \frac{\partial \boldsymbol{v}}{\partial t} = -\nabla p + \boldsymbol{F_m} \tag{11}$$

where $p(\boldsymbol{r}, t)$ is the pressure, $\boldsymbol{v}(\boldsymbol{r}, t)$ is the velocity at a point $\boldsymbol{r}$ in the medium, ρ_0 is the density of the medium.

Taking the divergence of the above equation and combining it with the continuity equation in the medium for such an acoustic wave, $\beta_s \frac{\partial p}{\partial t} + \nabla \cdot \boldsymbol{v} \approx 0$ gives the wave equation describing the pressure distribution:

$$\nabla^2 p - \frac{1}{c_s^2}\frac{\partial^2 p}{\partial t^2} = \nabla \cdot \boldsymbol{F_m} \tag{12}$$

Where β_s is the compressibility of the medium, $c_s = \frac{1}{\sqrt{\rho_0 \beta_s}}$ which is ~ 1500 m/s for biological soft tissue.

The pressure in the medium is given by the Green's function solution to Equation 12:

$$p(\boldsymbol{r}, t) = -\frac{1}{4\pi}\iiint d^3 r' \nabla_{r'} \cdot \boldsymbol{F_m}(\boldsymbol{r}', t)\, G(\boldsymbol{r}, \boldsymbol{r}', t) \tag{13}$$

Where $\boldsymbol{r}'$ is the location of the acoustic source, $\boldsymbol{r}$ is the location detector, $\nabla_{r'}$ implies derivative with respect to source space $\boldsymbol{r}'$, the Green's function for this solution $G(\boldsymbol{r}, \boldsymbol{r}', t) = \frac{\delta\left(t - \frac{R}{c_s}\right)}{R}$ where $R = |\boldsymbol{r} - \boldsymbol{r}'|$. The volume integration is carried out over the acoustic source distribution in the object space Ω. This equation gives the observed pressure for an impulse source, i.e., a source with its time function as $\delta(t)$. An induced acoustic source field with time dependence $h(t)$ and the transducer impulse response $r(t)$ gives rise to an observed pressure $p(\boldsymbol{r}, t) \otimes h(t) \otimes r(t)$, where $\otimes$ is the convolution operator. The Green's function for this time dependence can be written as $G(\boldsymbol{r}, \boldsymbol{r}', t) = \frac{hr\left(t - \frac{R}{c_s}\right)}{R}$, where $hr(t) = h(t) \otimes r(t)$ [152].

3.2.2 Image Reconstrcution

Equation 13 shows the pressure signal received by an ideal point receiver. With such a receiver collecting pressure signals on an aperture enclosing the object (Σ) in an acoustically homogeneous medium, the initial pressure distribution is related to the acoustic source as $-\frac{1}{c_s^2}\frac{\partial p}{\partial t}\Big|_{0+} = \nabla \cdot \boldsymbol{F_m}$ [28], can be determined by time reversing the acoustic waves [19]. This gives the acoustic source distribution in the medium as:

$$\nabla \cdot \boldsymbol{F_m}(r) \approx \frac{1}{2\pi c_s^3} \iint_{\sum} dS_d \boldsymbol{n} \cdot \frac{\boldsymbol{r_d} - \boldsymbol{r}}{|r_d - r|^2}\, p''(\boldsymbol{r_d}, |r_d - r|/c_s) \tag{14}$$

where $\boldsymbol{r_d}$ is a point on the detection surface, $\boldsymbol{r}$ is a point in the object space, and the double prime represents the second derivative over time. In this equation a term corresponding to the first derivative is neglected as its contribution is negligible compared to the second derivative term [33, 39].

3.3 Materials and Methods

3.3.1 Imaging System

Fig. 15A shows the schematic diagram of the magneto acoustic tomography imaging system for the mouse experiment. In this setup, a coil consisting of 3 turns of wire placed in the same plane, with a maximum outer diameter of 70 mm and 2 mm thickness (APP Inc., Freeville, NY, USA), is used to apply a microsecond long magnetic pulse to the object region. This coil is placed horizontally very close to the tank wall to maximize the magnetic field in the object region. It is driven by a customized magnetic stimulator using a capacitor and high

power switch to apply a pulsed current to generate the magnetic field. This capacitor in the stimulator can be charged from 0 to 24 kV applied to the coil by the solid state switch (APP Inc., Freeville, NY, USA). Fig. 15B shows the current through the coil at 24 kV capacitor voltage. The force contribution due to the magnetic field at this voltage is $\mathrm{B_z}\,\frac{\partial \mathrm{B_z}}{\partial \mathrm{z}} \approx 26\,\mathrm{T^2/m}$ leading to a force of $\sim 2.6 \times 10^{-20}\ N$ per particle giving rise to a pressure of ~ 1.5 Pa in the medium from the previously described method in Hu and He [76]. However, due to the large current through the coil, electromagnetic interference is observed at the ultrasound signal measuring transducers. In the imaging experiments the charging voltage is set to 16 kV giving optimum SNR for the ultrasound recording.

The imaging region of the object and the transducer with a diameter of 25 mm and a nominal peak frequency of 0.5 MHz (TRS ceramic, PA, USA) were immersed in the plastic tank of distilled water. The transducer has a bandwidth of 60% around the center frequency and the scanning performed using a rotational stage (B5990TS, Velmex Inc., USA) over 180 degrees with a step size of 2 degrees around the object. Piezoelectric signals collected by the transducer were amplified with a low-noise ultrasound amplifier and a bandpass filter with 75 kHz to 1 MHz cutoff frequencies (5660B, Olympus, MA, USA, and VP2000, Reson, Denmark) before entering the data acquisition system which acquired 2048 data points for each channel with a 5 MHz sampling rate. The data are averaged 200 times for each channel and recorded in the PC also synchronizing the magnetic stimulation, the data acquisition timing and the motor's position.

Additionally, after the magneto acoustic imaging experiment, pulse echo imaging of the object is performed with a commercial ultrasound scanner, a 64-channel US system (OPEN system, Lecoeur Electronique, Chuelles, France). The US system was connected to a 64-element US phased-array transducer (P7-4, ATL) with the elements arranged in a linear array configuration with interelement spacing of 0.18 mm. The center frequency of the transducer is 5 MHz; its

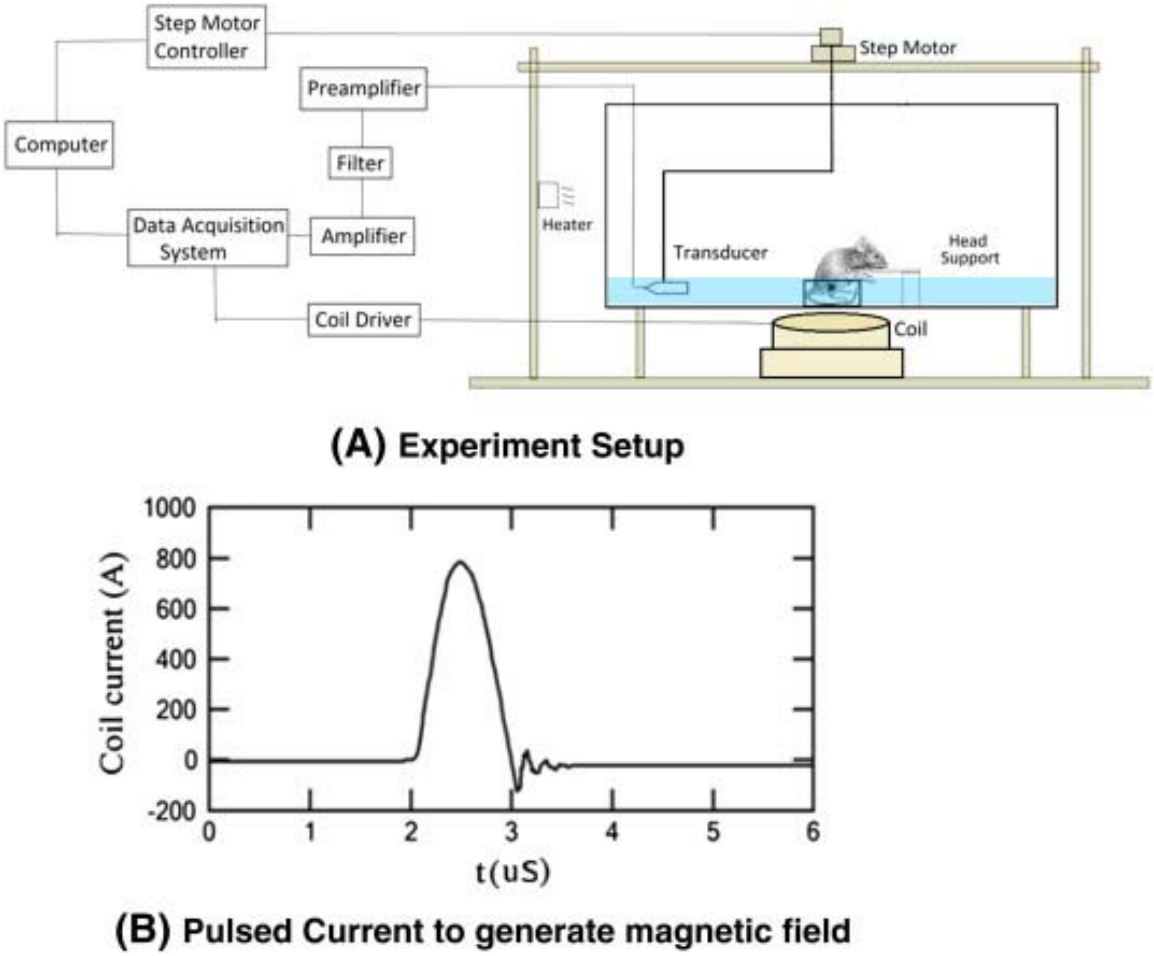

Figure 15. Experimental Setup of Magneto-acoustic Tomography. (A) Schematic diagram of the MAT imaging setup. The coil placed close to the tank is used to deliver the pulsed magnetic field to the imaging object. **(B)** The waveform of the applied current to the coil generates the *micro second* long magnetic pulse. (© 2016 Elsevier)

bandwidth is 3 MHz. This system is operated in the pulse echo mode with transmission from each channel and corresponding echo recording from all channels forming one measurement then repeated for all 64 elements. These data are then beamformed using the synthetic aperture based back-projection algorithm to reconstruct the ultrasound image corresponding to the imaging cross section of the MAT method [69, 171].

3.3.2 Mouse Tumor Model Preparation

For the *in-vivo* imaging experiments, prostate tumors are introduced over the hind limb of seven-week old nude mice by injecting LNCap cells into the limb. These LNCap cell lines commonly used in cancer research come from human prostate adenocarcinoma [172]. For inducing the tumor, 1 million cells suspended in 0.1 mL Matrigel matrix (50% Matrigel and 50% LNCaP growth medium) are subcutaneously injected into the hind limb of each of the nude mice weighing ~ 24 g. The tumors grow for 4 to 6 weeks and approximately reach a diameter of 5–10 mm. These mice are then used for the experiments.

3.3.3 Magnetic Nanoparticles and *In vivo* Imaging Experiment

For the experiments, we use commercially available, water soluble ferrofluid superparamagnetic nanoparticles, EMG 308 (Ferrotec, NH, USA). The EMG 308 (X_{np} = 0.5) consists of Fe_2O_3 with a particle diameter of ~15 nm in the suspension [76](https://ferrofluid.ferrotec.com/products/ferrofluid/emg). Transmission electron microscopy (TEM) image of aqueous EMG-308 is shown in Fig. 16A and the histogram of the particle size distribution is shown in Fig. 16B. For the mouse

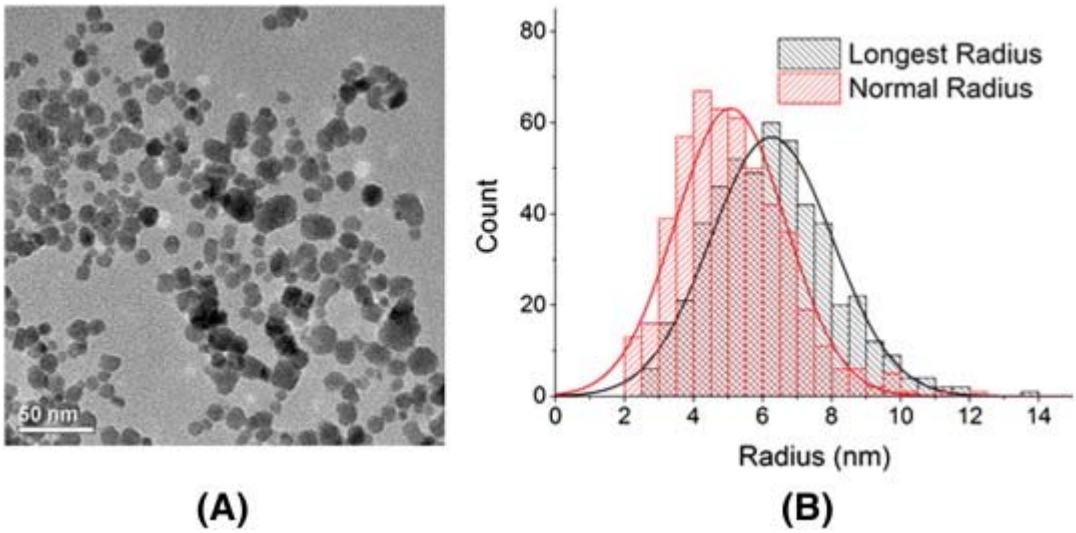

Figure 16. Characterization of the magnetic nanoparticles. (A) Room temperature transmission electron microscopy (TEM) images of aqueous EMG-308 IONPs were acquired with ab FEI Tecnai T12 microscope (FEI, Inc., Hillsboro, OR) operating at 120 kV. A 200 mesh copper grid with formvar and carbon supports was dipped into a ~ 1 mg Fe/ml IONP suspension, then removed and allowed to dry before imaging. **(B)** The histogram of the longest radius and the radius normal to it were measured using Image J (NIH). (© 2016 Elsevier)

imaging experiments, an aqueous solution of EMG 308 is used with an IONP concentration of 4 mg Fe/mL; a volume of 50–75 µL is injected into the center of the tumor with a single application.

The mouse in the imaging experiment setup is seen in Fig. 15A. As seen in this figure, the anesthetized mouse with the tumor is placed inside a cup, in a sitting position, and fixed with a cooled agar gel placed around the tumor region in the cup. Also, since the tumors are present over the hind limbs, they are less affected by the cardiac motion. The cup region with the tumor is immersed under warm water for coupling of the acoustic signal with the ultrasound transducer, while the head of the mouse is held outside the water to allow for breathing. Additionally, a

heater with a thermostat is used to maintain the temperature (~36 °C) in the tank during the experiment. The mouse is anesthetized using IP injection of mixture of ketamine 100 mg/kg and xylazine 10 mg/kg for the imaging experiments. After the imaging experiment, the mouse, under anesthesia, is sacrificed by cervical dislocation and the tumor excised for histological analysis. The histological section is stained with Prussian blue stain and counter stained with nuclear fast red. These experiments have been approved by the Institutional Animal Care and Use Committee (IACUC) for animal research at the University of Minnesota.

3.3.5 MAT Image Reconstruction

For the image reconstruction we use the modified time reversal algorithm presented in the theory section. It is seen through studies of ultrasound image reconstruction theory [173, 174] that there is data redundancy in the measured ultrasound signal from around the object. A half view angle corresponding to 180 degrees of scanning for data collection around the imaging object is sufficient for the tomographic reconstruction. In the present study, we used 180-degree scans to avoid potential signal distortion from the ultrasound pressure waves traversing through the abdominal regions of the mouse reaching the transducer possibly containing gases. Also, the reduced scan angle leads to reducing the scan time. The ultrasound transducers available have a limited bandwidth around the center frequency of about 60%-70% acting as a bandpass filter on the received pressure signal as seen in the theory section. This filter, as seen in the frequency domain, creates a signal windowing function around the center frequency and behaves much like a Gaussian low pass filter combined with the temporal derivatives

needed for ultrasound image reconstruction as seen in Equation 14 [175]. The temporal derivatives of the measured pressure signal used in the image reconstruction could lead to amplification of high frequency noise present. However, as the band pass filtering of the transducer already contains the temporal derivatives, we further modify the image reconstruction in Equation 14 by substituting the pressure signal p, instead of its derivatives p'', for a given transducer location.

In the experiments, the time varying magnetic field leads to electromagnetic interference (EMI) at the ultrasound transducer. This continues for a certain duration due to the turn off transients associated with the stimulator and the impulse response of the transducer. The observed EMI signal in the experimental data has significant, low frequency variations. This noise on time reversal leads to slow varying spatial signals interfering with the reconstruction of the low spatial frequency component of the acoustic source distribution. This leads to errors in IONP distribution imaging, so the received acoustic signal is further bandpass filtered to eliminate most of the low and high frequency noise. A simple filter implemented for this purpose in frequency domain is

$$F(f) = \begin{cases} 1, & 100\ kHz < f < 900 kHz \\ 0, & otherwise \end{cases} \tag{15}$$

I/Q demodulation based envelope detection is performed on the filtered signal, and the ultrasound image reconstruction algorithm as described above is applied to estimate the acoustic source distribution [69].

3.4 Results

3.4.1 Contrast-enhanced MAT with MNPs

We performed magneto acoustic tomography experiments in live nude mice using the proposed system. In the experiment result seen in Fig. 17, we used an agar gel phantom with nanoparticles embedded to test the signal due to the magneto motive force. The phantom as seen in Fig. 17, *A* consists of 1% agar gel with a 1.5 mm circular agar gel inclusion infused with iron oxide nanoparticles. A thin piece of plastic is placed between the inclusion and the background to prevent diffusion of nanoparticles. The concentration of nanoparticles in the inclusion is varied from 8.3, 4, and 1.8 mg Fe/ml to perform three different experiments. The MAT image of the phantom is reconstructed as described in the methods section. The intensity of the signals used in the image reconstruction is normalized to the maximum signal measured in the experiment. The reconstructed image corresponding to the inclusion concentration of 8.3, 4, and 1.8 mg Fe/ml is shown in Fig. 17B-D respectively. It can be seen then that the image intensity varies with the concentration of nanoparticles. Also, the average image intensity and variation in the inclusion region for the three phantoms were plotted with respect to the concentration as seen in Fig. 17E, which shows the linear dependence of the magneto-motive signal on the nanoparticles concentration. In addition, the resolution of the imaging system is ~1.5 mm [159, 176]. The effect of this on the reconstruction leads to distortion in the image of the object with the image intensity varying through the inclusion region as seen in the Fig.17.

Experiments were also performed to image five mouse tumors with the nanoparticles injected as described in the methods section. Fig. 18A is the imaged

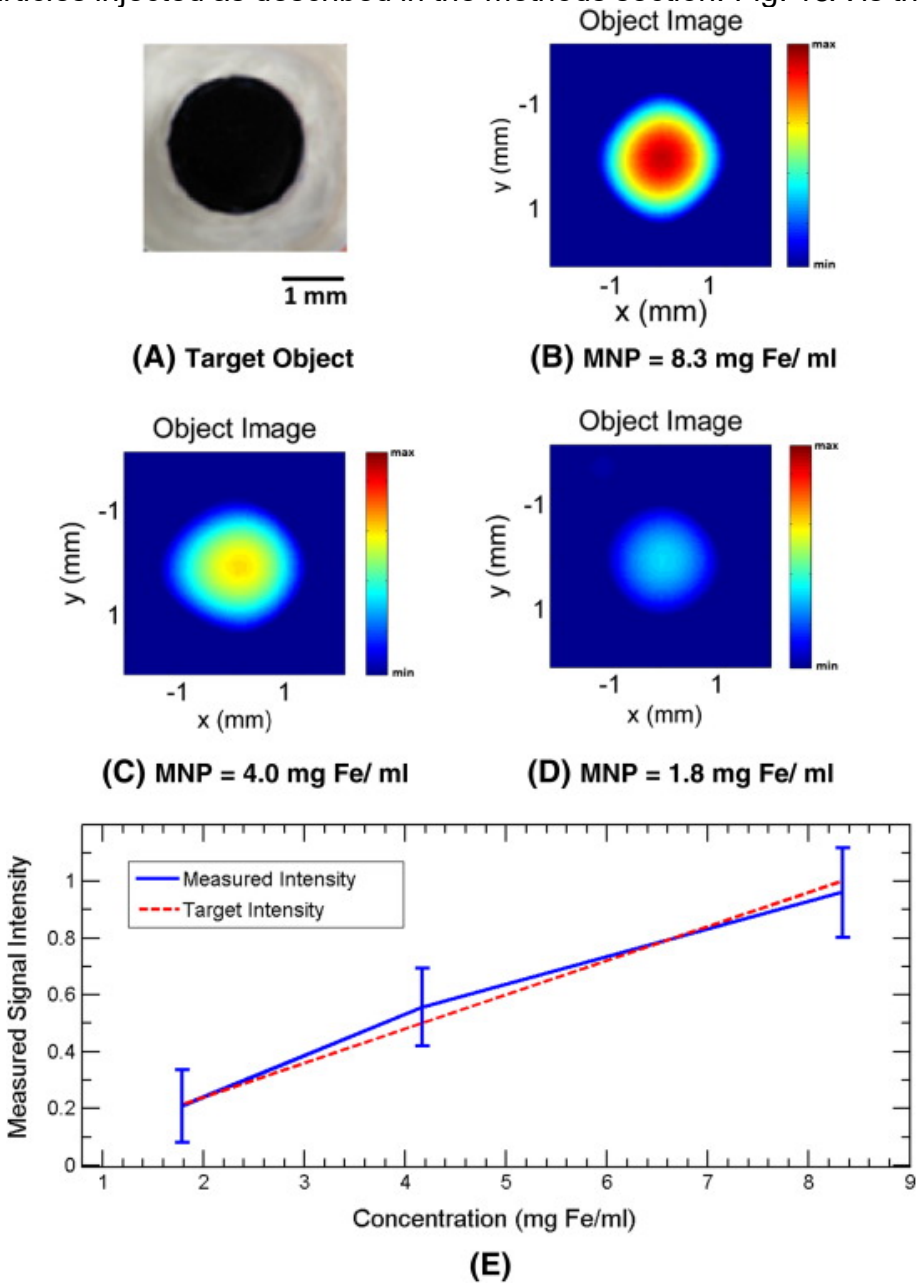

Figure 17. Imaging experiment with a small circular inclusion of IONP at different concentrations in 1 % background agar gel. (A) Top view photo of the imaging object. **(B , C , D)** MAT images of the object with IONP concentration of ~ 8.3, 4.0, 1.8 mg Fe/ml respectively. **(E)** Plot of the measured image intensity with respect to the IONP concentration. (© 2016 Elsevier)

mouse and the tumor region, about 7 mm, in the experiment phantom with the corresponding orientation of the scanning transducer and applied magnetic field. The signal collected from this location is processed as described in the methods section, and this envelope detected signal is shown in Fig. 18A. It can be seen from the figure that strong signals are present around 183–187 μs corresponding with the location of the tumor region; the spread in the signal of around 4 μs corresponds to the distribution of the nanoparticles in the tumor. The background signal strength is approximately 3–4 times lower than the IONP signals. Histological slices of the tumor stained with Prussian blue can be seen in Fig. 18B, confirming the presence of the injected nanoparticles. The measured magneto acoustic signals are used to reconstruct the distribution of the IONP using the back projection algorithm. The image reconstruction result can be seen in Fig. 19. The ultrasound (US) image of the mouse is shown in Fig. 18A showing the imaged cross-section with the tumor present superficially over the right hind limb of the mouse. As the pulsed magnetic field is not applied during the imaging, the signal from the IONPs, due to the magneto motive force, is absent. The intensity of ultrasound speckle distribution is fairly uniform throughout the reconstructed image. The MAT image showing the IONP distribution can be seen in Fig. 18B. The noise baseline of the reconstruction from the imaging system is used as the floor of the reliable signal that can be measured and masked out from the MAT image. Fig.18C shows the overlaying of the MAT image on the ultrasound image of the mouse; the IONP signal is strongly present in the region over the hind limb of the mouse indicating the tumor. Fig. 18D shows the tumor region with the overlaying MAT

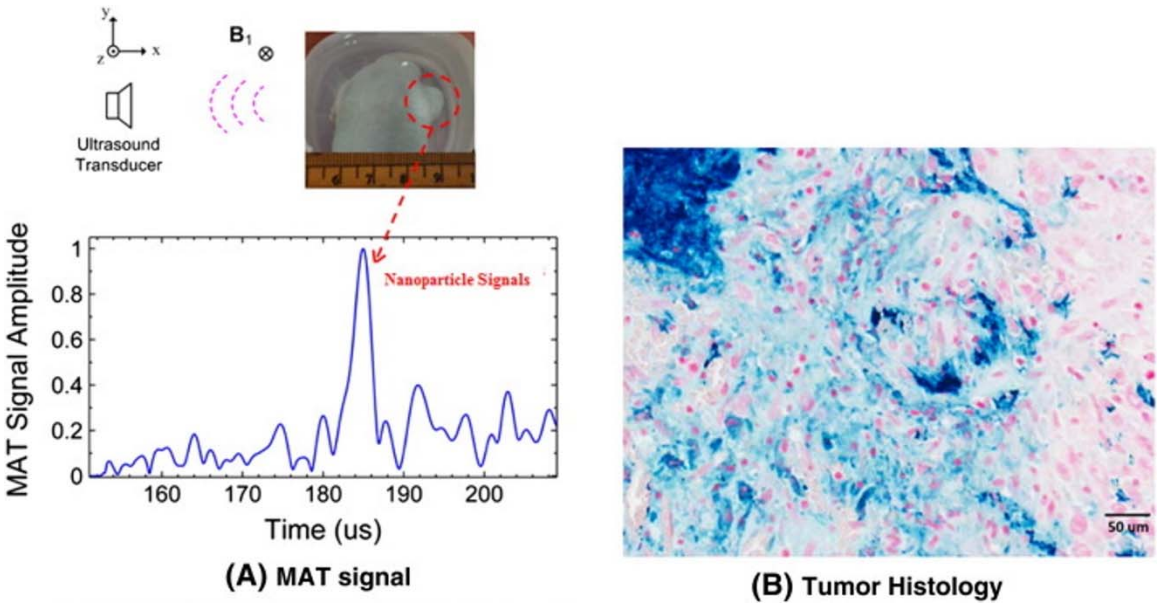

Figure 18. MAT signal and tumor histology. (A) Top view photo of the imaging object showing the tumor region in the mouse and the corresponding MAT signal due to the embedded IONPs. (B) Histological cross section of the tumor injected with IONPs. The section is stained with Prussian blue stain and counter stained with nuclear fast red with the blue areas indicating the IONPs. (© 2016 Elsevier)

image. From the non-uniform intensity of the reconstructed IONP distribution, we can also see the heterogeneous distribution of the nanoparticles due to the IONP injection in the tumor region, seen in the histology from Fig. 17B.

To further validate the MAT method for *in-vivo* IONP imaging, four more tumor images were obtained as shown in Fig. 20. Fig. 20A-D shows the ultrasound image of the tumor regions without the magnetic pulse stimulation. The corresponding images with IONP distribution estimated from MAT images are shown in Fig. 20E-H. The presence of the IONP in the mouse can be clearly seen in the MAT images. However, as the IONP distribution is not uniform from the injection, the intensity distribution of the reconstruction varies throughout; and as

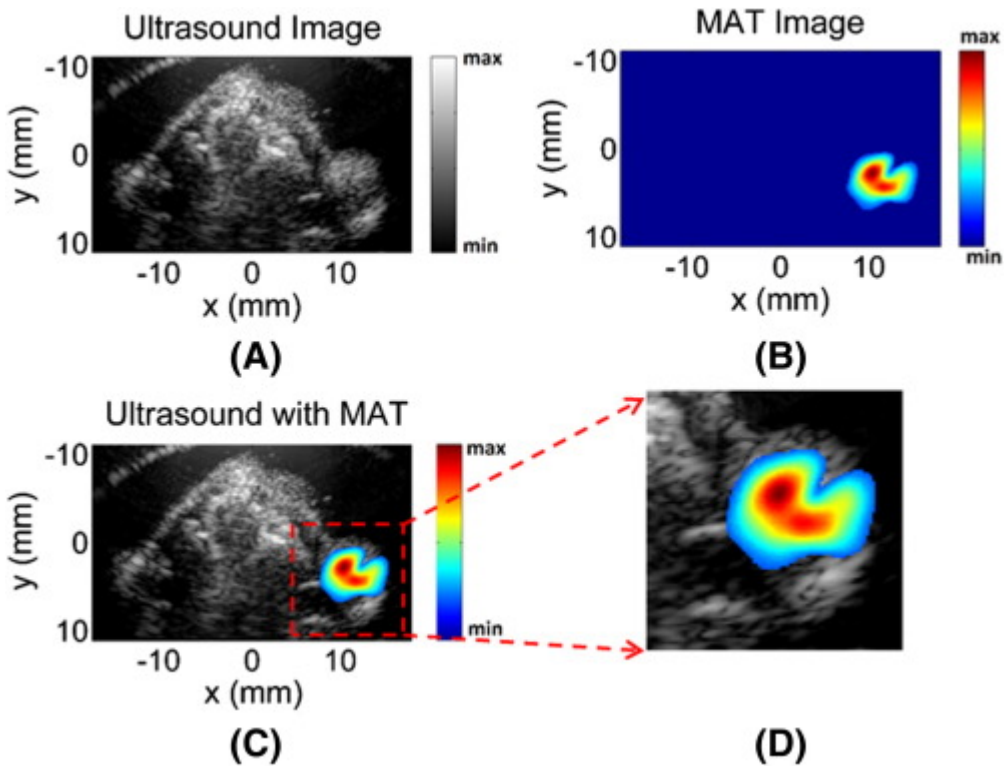

Figure 19. Ultrasound and MAT images. (A) Ultrasound image (US) of the mouse corresponding to the magneto acoustic tomography imaging cross-section showing the tumor on the right hind limb of the mouse. (B) Magneto acoustic tomography image of the magnetic nanoparticles injected in the mouse tumor. (C) Combined MAT and ultrasound image indicating the tumor with the nanoparticles present in the region. (D) Reconstructed image area highlighting the tumor region. (© 2016 Elsevier)

seen in Fig. 20H from the smaller region of IONP in the reconstruction, the dose of the nanoparticles retained in the imaging region could be small.

3.4.2 hfMAT-MI for High Resolution Imaging of MNPs

Furthermore, as presented in Chapter 2, the developed hfMAT-MI system is proved to image samples with MNPs inclusions to obtain better spatial resolutions for imaging the magnetic nanoparticles. In this scheme, from the mathematical expression by Equation 10, both the dynamic and static magnetic

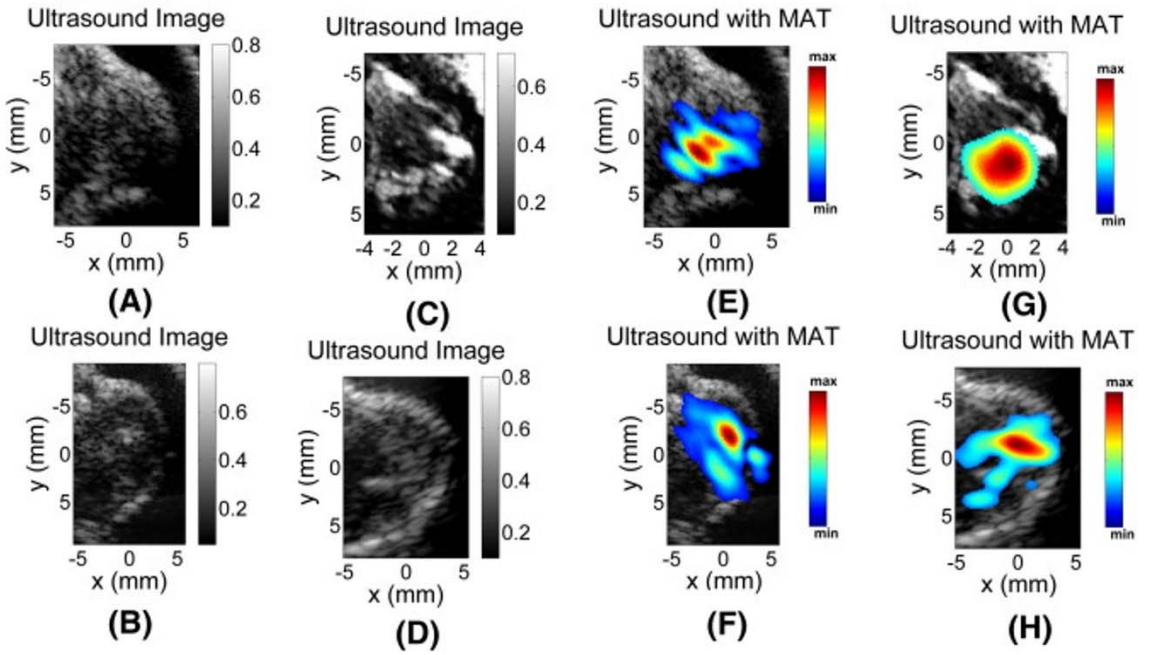

Figure 20. MAT image of four tumors. (A – D) Ultrasound image corresponding to the pulse echo imaging method without the applied magnetic pulse. **(E – H)** MAT images overlying the ultrasound image showing the IONPs present in the tumor region. (© 2016 Elsevier)

fields and their gradients may generate magneto-motive force jointly on MNPs, which is much stronger than the Lorentz force in magnitudes. These two acoustic sources exist in one scanning, and can be recorded simultaneously by ultrasound transducers and further reconstructed with the hfMAT-MI technique. Phantom experiments with MNPs' gel inclusion indicate that the spatial resolution of magnetic nanoparticle imaging with the MAT is enhanced, which is used to better determine the distributions of both MNPs and the electrical impedance in the phantom (Fig. 21A). Moreover, from the study on a phantom with MNPs fluid inclusions, the external static magnetic field may give rise to MNPs aggregation and thus form MNPs clusters (Fig. 21B-D). This geometric change may also lead to an increased magnetic momentum of the nanoparticle clusters, thus a higher

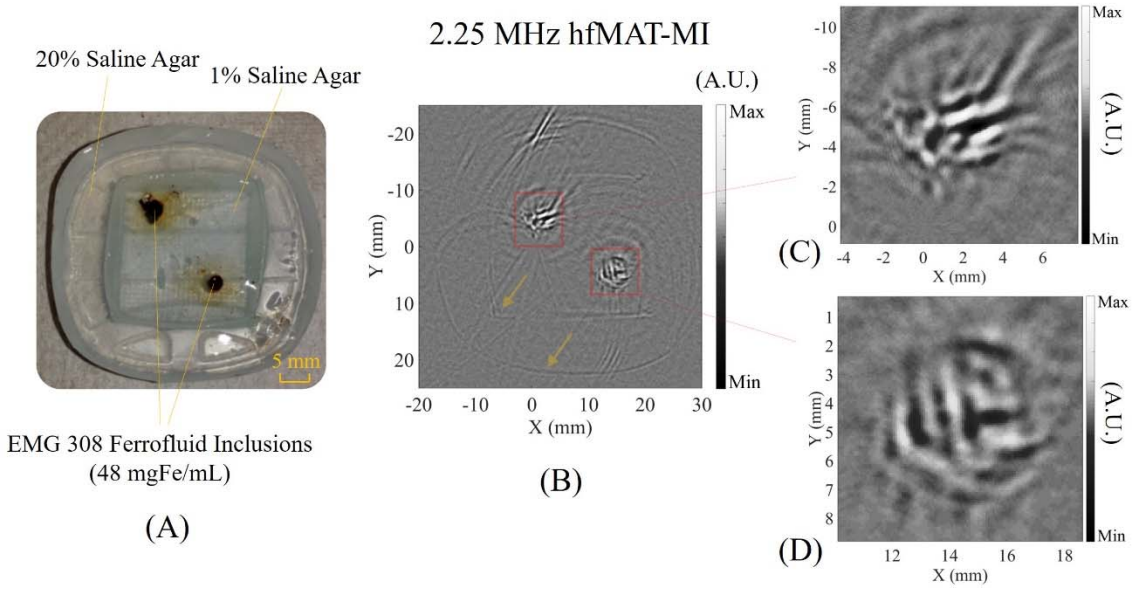

Figure 21. 2.25 MHz hfMAT-MI image of gel phantom with MNP inclusions. (A) Physical phantom consists of agars with two salinity (20% and 1%), and two cylindrical inclusions of EMG 308 MNPs with the ferrum concentration of 48 mg/mL. (B) A magnetoacoustic image reconstructed with 2.25 MHz hfMAT-MI. The sharp boundaries of the agar phantom have been captured as indicated by yellow arrows. (C-D) Images of the MNP inclusions depicting potential aggregation of nanoparticles.

magnetic susceptibility, which further results in an enhanced magneto-motive force. This phenomenon can further contribute to the imaging contrast and improve the signal-to-noise ratio of magnetic nanoparticle imaging with magnetoacoustic methods. Fig. 21B-D demonstrates the very first image that presents the distributions of MNPs using the resolution of 2.25 MHz ultrasound.

In this imaging study, I used a home-made stimulator powered with 440 V, and scanned the phantom at 655 angles with a step size of 0.5 degrees. The ultrasound scanning radius was 206 mm.

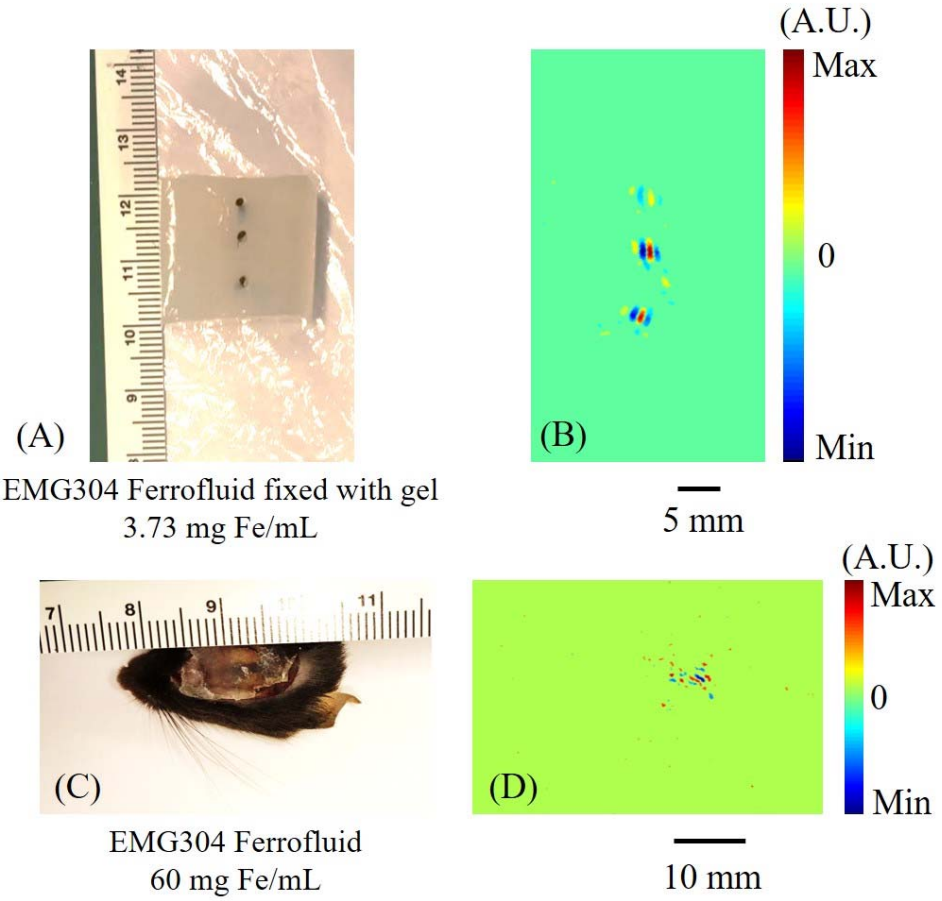

Figure 22. 1.5 MHz hfMAT-MI imaging phantom with MNPs. (A) An agar phantom with three cylindrical MNP inclusions having EMG 304 (ferrum concentration is 3.73 mg/mL). (B) The hfMAT-MI image of the phantom in (A). (C) After euthanizing a mouse subject, 60 mg Fe/mL EMG 304 MNPs were injected into the brain through a 1-mm burr hole. (D) The distribution of MNPs inside the mouse head reconstructed with 1.5 MHz ultrasound.

Furthermore, I applied the developed 1.5 MHz high-power hfMAT-MI to image the MNPs in an agar phantom (Fig. 22A) and, interestingly in a mouse carcass to explore the feasibility of transcranial detection of the magneto-motive force-induced ultrasound signal (Fig. 22C).

Although the 1.5 MHz hfMAT-MI does not provide MNP distributions as detailed as the 2.25 MHz system, the high power (up to 25 kV) capability of this

1.5 MHz system is seen to provide a relative high sensitivity (3.73 mg Fe/mL) and meanwhile shortened scanning duration. Still, it can be observed that Fig. 22B and D depict the nanoparticles with a better spatial resolution than those presented with the regular MAT (Figs. 17, 19, 20). Interestingly, although there would be unsurprisingly significant ultrasound signal attenuation due to the skull, the magneto-force induced ultrasound signal at 1.5 MHz can still be partially detected in order to have a rough estimation of the distribution of MNPs behind the skull; we can thus qualitatively know that the original signal strength would be remarkable.

3.4.3 hfMAT for Epidermal Growth Factor Receptor (EGFR)-targeted MNPs

With the regular MAT as its results being summarized in 3.4.1, the magnetic nanoparticles were local injected to the tumor protrusion for further imaging tests. Our goal for the magnetoacoustic imaging of MNPs is to test out whether or not we can probe the nanoparticles with MAT, in which the nanoparticles *per se* are specifically targeting to the growing tumor and injected without knowing the location of cancerous tissues. Although considered as highly demanded, this has been long believed as a grand challenge majorly because of the feasibility of fabricating such targeted MNPs. Dr. Panyam's group in UMN have successfully synthesized a type of water-dispersible EGFR-targeted superparamagnetic iron oxide (SPIO) MNPs for inhalation to treat non-small cell lung cancer (NSCLC) [177], as the EGFR overexpression is observed to be phenomenal in NSCLC patients [178, 179]. With the help from his group, EGFR-targeted EMG 308 ferrofluid (ferrum concentration: 3.2 mg/mL) has been developed for pursuing this goal. Using the similar animal protocol mentioned in 2.3.3 and 2.3.4, after anesthetizing

the animal, this *in vivo* experiment injected the targeted MNPs to the nude mice subject through tail vein by 200 μL at least 40 minutes prior to the 1.5 hour-long hfMAT scanning. It is worth to note here that the static magnetic field has been removed from the hfMAT-MI setup in order to eliminate confounding signals by Lorentz force, i.e. the signal obtained from hfMAT can be all attributed to the presence of MNPs, given that the flux density magnitude of pulsed magnetic field is about 50 times weaker than that of the static one (Fig. 8c-f). The tiny ultrasound signals generated on the MNPs were harnessed to reconstruct the presence of nanoparticles, as shown in Fig. 23B. The dashed oval circles the suspected signals originating from the unilateral side of tumor protrusion. There might be retention of the targeted MNPs taking place at the cancerous tissue, although the generated signal is so weak to reach the detection sensitivity limit. Despite of the challenges,

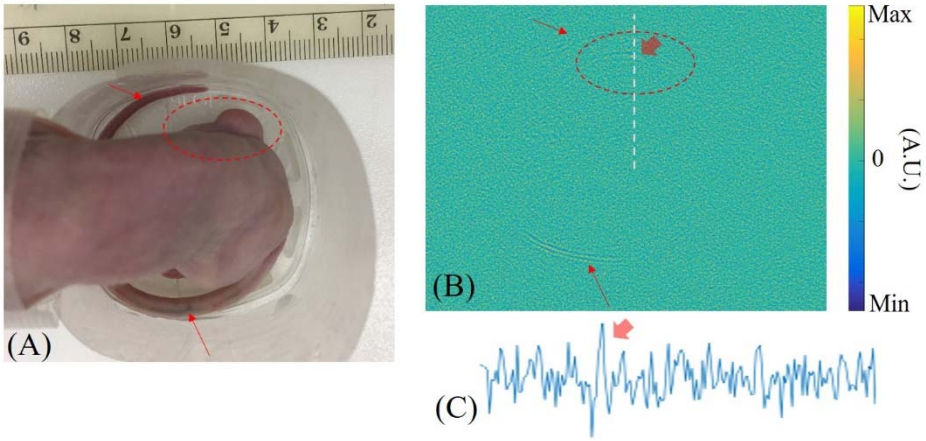

Figure 23. The first trial of magnetoacoustic imaging of EGFR-targeted MNPs. (A) The tumor-bearing nude mice was injected with the EGFR-targeted SPIO nanoparticles through the tail vein. (B) 1.5 MHz hfMAT-MI reconstructed signals show the residual MNPs in the tail and part of the injected nanoparticles appear at the tail tip (indicated by red line arrows). The dashed oval circle and the filled red arrow indicate suspected signals originating from the unilateral side of tumor protrusion. (C) The line profile of the reconstructed signals along the white dashed line in (B).

this is indeed the first trial of using magnetoacoustic imaging to capture the presence of tumor-targeted nanoparticles.

3.5 Discussion

We applied magnetoacoustic tomography (MAT) and high-frequency MAT-MI methods using a short pulsed magnetic field to image magnetic nanoparticles applied to prostate tumors in a mouse model. The preliminary *in-vivo* study shows that the images of the IONP present in the tumor are reconstructable. Further, we tested the strength of the MAT signal which is proportional to the dependence on the concentration of magnetic nanoparticles for a phantom with uniform *z-directional* distribution of nanoparticles. The acoustic source creating the MAT pressure signal is the divergence of the magneto motive force. This is dominant along the *z* direction in the experimental setup over the object region and depends on the *z* distribution of the IONPs in this MAT setup. Therefore, to further obtain a quantitative map of the IONP distribution, this z-dependence of the acoustic source would have to be taken into account. This can be achieved by varying the *z* profile of the magnetic field and performing multiple measurements and combining them as used in multi excitation methods proposed in electrical properties imaging [44, 180]. This could give a quantitative distribution which could be useful in designing therapeutic applications.

The MAT signal from the IONPs is in the same frequency range as the applied RF pulsed field, matched to the ultrasound scanner being used to measure the signal for optimum signal recording. The ultrasound systems have a limited bandwidth around a center frequency governing the resolution of the image

reconstruction. The ultrasound resolution can be obtained, for the tomographic reconstruction method used in the current study, by estimating the point spread function of the imaging system. This is done by using a point source in Equation 13, $\nabla \cdot \boldsymbol{F_m}(r) = \delta(r)$, and substituting the estimated pressure in Equation 14. This gives the reconstruction of a point source with this imaging system, which is an estimate of the imaging point spread function. The current ultrasound imaging system used in MAT imaging has a center frequency of 500 kHz leading to an imaging resolution better than 2 mm shown in previous resolution estimating experiments and simulations of the point spread function of the ultrasound system [159, 176]. The imaging depth of the MAT system is governed by the attenuation of the ultrasound wave travelling through tissue. Unlike ultrasound, the magnetic field in the low MHz range used in MAT method does not get attenuated by the tissue [45, 169]. The strength of the ultrasound wave decays exponentially: $p(x) = p(0)\exp(-\alpha x)$, where x is the depth of the MAT source from the sensor, $p(0)$, $p(x)$ is strength of the signal at the source and sensor, α is the ultrasound attenuation coefficient. The attenuation coefficient α is around 1 dB/cm for most soft tissue at 1 MHz frequency. In the current system the signal from the MNPs embedded in the tumors on the surface of the mouse leads to an imaging contrast of 5–7 times due to the improvement in SNR from the signal averaging from various measurement directions present in the image reconstruction method. [42] This imaging contrast is proportional to the strength of the signal which is obtained at the surface of the body of the mouse. Assuming an imaging contrast of 2 would be the limit of the imaging depth, with the exponential decay of the pressure wave,

this contrast would be obtained for an imaging depth of around 10 cm in soft tissue. The spatial distribution of the magnetic field generated in the MAT method is governed by the geometry of the coils [45, 169]. In the present study we use a 5 cm diameter coil and the imaging region is located 2.5 cm from the coil surface. To obtain a similar strength magnetic field at a larger depth either a larger diameter coil or coil arrays could be used.

In the current imaging setup, a single transducer scanning mechanically around the object is used for the data acquisition. For the data to image a tumor region with the tomographic method used, 50 min of scanning time is required (140° view angle). However, the use of ultrasound imaging arrays to acquire these data in parallel could significantly shorten this time. After this data acquisition, an ultrasound back-projection algorithm with built-in data filtering is used to reconstruct the acoustic source from IONPs. Thus, each of the presented tomographic images of the nanoparticles' spatial distributions can be produced less than 5 s by a computer with an Intel Core i7 processor.

In the MAT method, though, we apply a very large magnetic field of around 120 mT at ultrasound frequencies which can lead to induced electric fields in the sample to be around 550 V/m. This is comparable to the stimulating strength in transcranial magnetic stimulation (TMS). However, the total energy applied to the samples in MAT is much lower than TMS, as the MAT pulse duration is at the microsecond level instead of hundreds of microseconds in TMS. Additionally, the temperature rise due to a microsecond long pulse applied to the IONP at the concentration of EMG 308 is around the mK range [80], and also the pulse is

repeated at a slow repetition frequency under 50 Hz further dissipating the heat deposited leading to unsubstantial temperature rise in the object. Thus, the use of a short duration pulse reduces the amount of energy deposited in the tissue.

The acoustic homogeneity assumption used in the theoretical derivation in this study restricts the proposed imaging method to primarily soft tissue imaging. The acoustic heterogeneity of soft tissue is less than 10%, and its effect can be negligible for those imaging techniques based on the acoustic measurements of induced ultrasound signals [181, 182].

In these MAT-based *in-vivo* imaging studies we performed intratumoral injections to have efficient accumulation of the non-targeted superparamagnetic nanoparticles. These intratumoral injections lead to the uneven distribution of nanoparticles in the tumor. We have initiated the studies using tumor specific antibodies modifying the magnetic nanoparticles that would be applied systemically through blood; and on accumulation in the tumor, it would be imaged as a potential method for early detection of tumors for screening purposes. Also, superparamagnetic iron oxide nanoparticles are seen to have low cytotoxicity concerns [82] enabling them to be more suitable for cellular/molecular biomarkers in biomedical applications which could be a concern with contrast agents required for some imaging methods such as radionuclide imaging.

Chapter 4. Non-Invasive Brain Imaging Perturbed by Low-intensity tFUS

4.1 Introduction

In this chapter, by reversing the MAT-MI model, I will firstly introduce an intermediate study using focused ultrasound to stimulate and generate local electrical potentials in agar phantom and excised fresh brains in the existence of a static magnetic field. Subsequently, I will further summarize my work on using electrophysiological source imaging (ESI) to monitor global brain responses *in vivo* perturbed by low-intensity tFUS.

Imaging brain activity is of utmost importance to understand the brain. Functional imaging modalities have been developed to understand the brain's mechanisms of action, including fMRI, electroencephalography (EEG), magnetoencephalography (MEG), positron emission tomography (PET), *etc*. While these imaging modalities are noninvasive in nature and have been used widely to study human brain functions and dysfunctions, they are limited in either spatial resolution (such as EEG or MEG) or temporal resolution (such as fMRI and PET). EEG/MEG offers high temporal resolutions capturing brain dynamics, yet has limited spatial resolution to image brain activity due to the head volume conduction effect. fMRI is widely utilized for neuroscience research. However, the present resolution of 3 Tesla fMRI typically used for cognitive neuroscience studies and clinical applications is few millimeter (mm) spatially (voxel size) and in the

order of seconds temporally. Such temporal resolution is far below the neural activation in which action potentials are firing, in the order of one millisecond.

Perturbation-based neuroimaging is a novel pathway for neuroimaging by combining neuromodulation with the functional neuroimaging modalities. Current electric and electro-magnetic non-invasive neuromodulation approaches like transcranial magnetic stimulation (TMS) and transcranial direct current stimulation (tDCS) have poor spatial resolution, suffer from a depth-focality tradeoff and experience significant attenuation at depth, thus making them inappropriate to effectively stimulate specific neural circuits. Transcranial focused ultrasound (tFUS) is a new and promising non-surgical, low-energy technique for inducing transient plasticity with high spatial resolution, adjustable focus and low soft-tissue attenuation. Despite the unclear mechanism, there are mounting evidences that ultrasound can interact with neural tissue. Ultrasound has been proved to noninvasively stimulate the animals' hippocampus and motor cortex, and even disrupt seizure activity induced by chemicals in animal models. tFUS has recently shown its capability to be a safe, effective, and highly spatial-selective neuromodulation method in humans. Therefore, an integration of EEG and tFUS would identify a portable, noninvasive perturbation-based neuroimaging modality having high spatiotemporal resolution.

4.2 Characterization of the Lorentz Current Induced by Acoustic Radiation Force (ARF)

4.2.1 Theory

Ultrasound technique has attracted great attention and been used to mediate the stimulation process. Instead of passively detecting ultrasound waves from Lorentz force and/or magneto-motive force, in our proposed non-invasive stimulation scheme, an active focused ultrasound beam is transmitted to vibrate a local volume of a conductive object with the ARF. With the existence of an external magnetic field, a corresponding Lorentz current $\boldsymbol{J_L}(\boldsymbol{r},\ t)$ is thus induced at the focal spot of the ultrasound beam as described as in Equation 16 [23, 183]:

$$\boldsymbol{J_L}(\boldsymbol{r},t) = \sigma(\boldsymbol{r})\ \boldsymbol{B_z} \times \boldsymbol{v}(\boldsymbol{r},t) \tag{16}$$

in which $\sigma(\boldsymbol{r})$ is the tissue electrical conductivity, and the ultrasound-induced vibration has a velocity $\boldsymbol{v}(\boldsymbol{r},t)$ within a constant magnetic field $\boldsymbol{B_z}$. Our hypothesis is that using acoustic radiation pressure (ARP) in a focused way can increase the mechanical motion of the vibrated tissue, thus improving the stimulation efficacy.

4.2.2 Materials and Methods

In this present study, we have tested this ultrasound-induced directional Lorentz-current stimulation in saline gel phantoms with dual mode ultrasound array (DMUA) [184, 185] in a collaboration with Dr. Ebbini's lab at UMN. The dual-mode ultrasound array consists of 2x32 elements operated at a center frequency of 3.2 MHz with a concave spherical radius of 40 mm. The F number is 0.86 given its small focal length relative to the big effective ultrasound aperture. The DMUA is

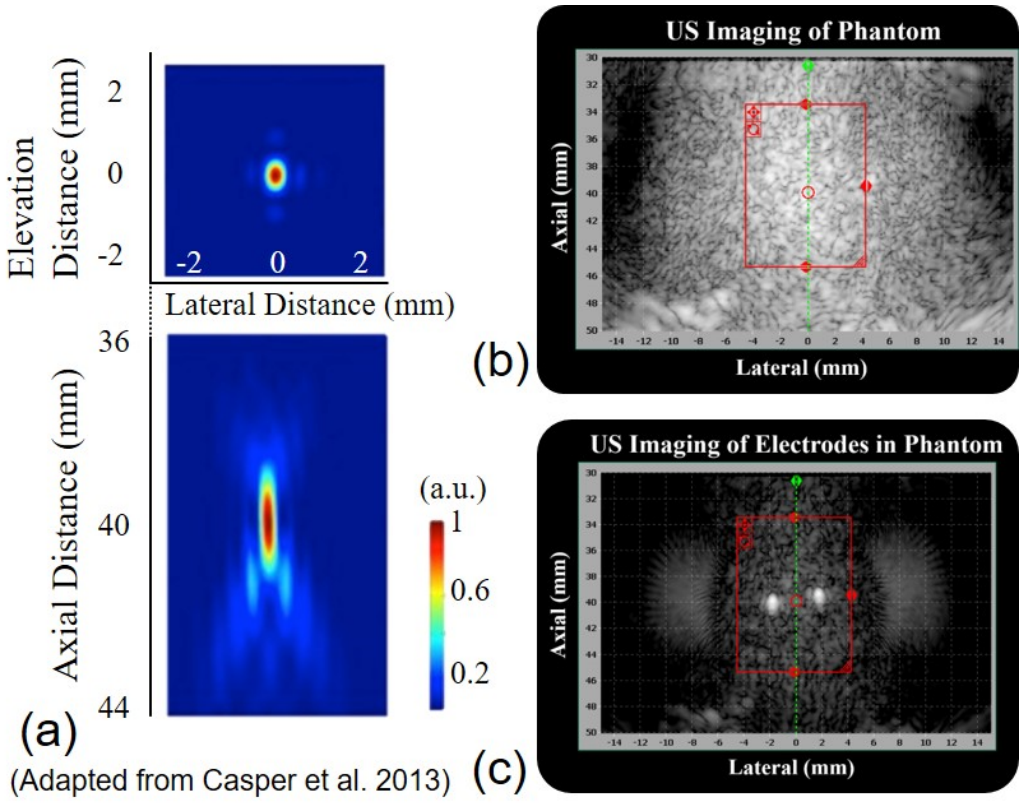

Figure 24. DMUA imaging performances. (a) The spatial resolution characterization (adapted from Casper *et al*. 2013). (b) Ultrasound imaging by the DMUA of a cellulose phantom. (c) An ultrasound image of a phantom inserted with two needle electrodes presented as two white spots.

able to achieve a small focal spot, with a -6 dB contour at 1.6 mm in axial direction, 0.25 mm in lateral direction (Fig. 24a).

To effectively receive the ultrasound radiation pressure, a certain concentration of cellulose is introduced as ultrasound scatterer in the preparation of the phantom, thus the phantom was imaged as Fig. 24b. To determine the induced current, a pair of unipolar needle electrodes and electric potential measurement are used, and the ultrasound image shows the distance between the two electrodes is about 4 mm (Fig. 24c). Fig. 25 shows a conceptual diagram of generating and recording the focal Lorentz-current in phantom tissues. The

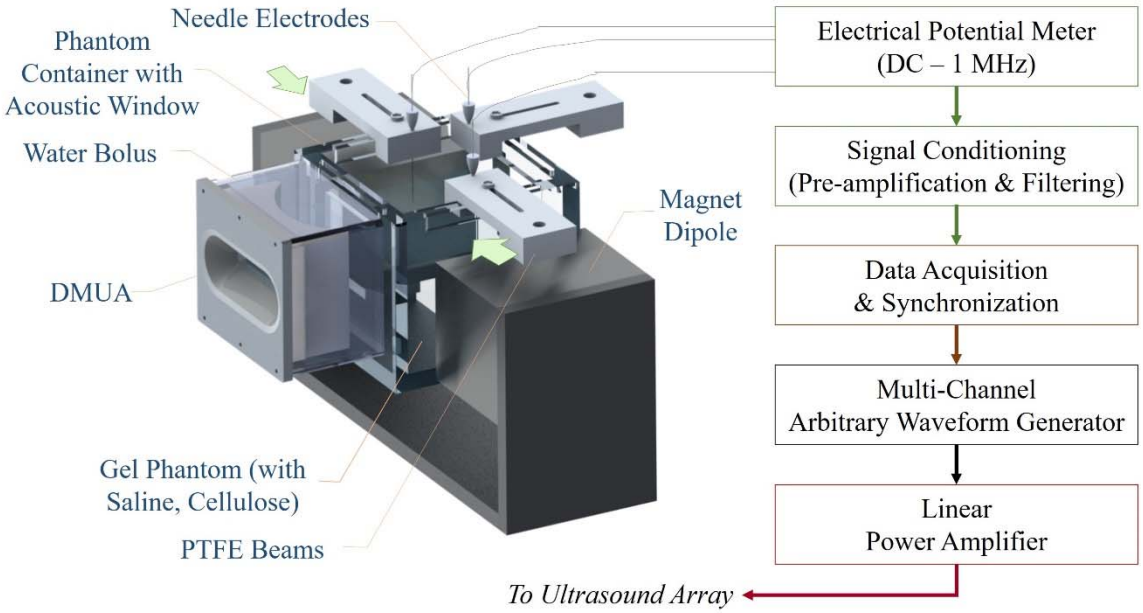

Figure 25. Diagram of Lorentz-current stimulation and recording system.

DMUA is programed to transmit customized ultrasound waveforms, which are amplitude-modulated with low-frequency envelope, e.g. < 100 Hz.

Fig. 26 shows the sonication temporal profiles, ARF-induced electrical potentials and their spectral power density. The estimated Lorentz current density is 4 μA/cm^2 at the ultrasound focal region (comparing with 83 μA/cm^2 used in tACS by [95]). It can be observed that the spectral contents of the induced Lorentz current follow the applied acoustic radiation frequencies, and also include their harmonics.

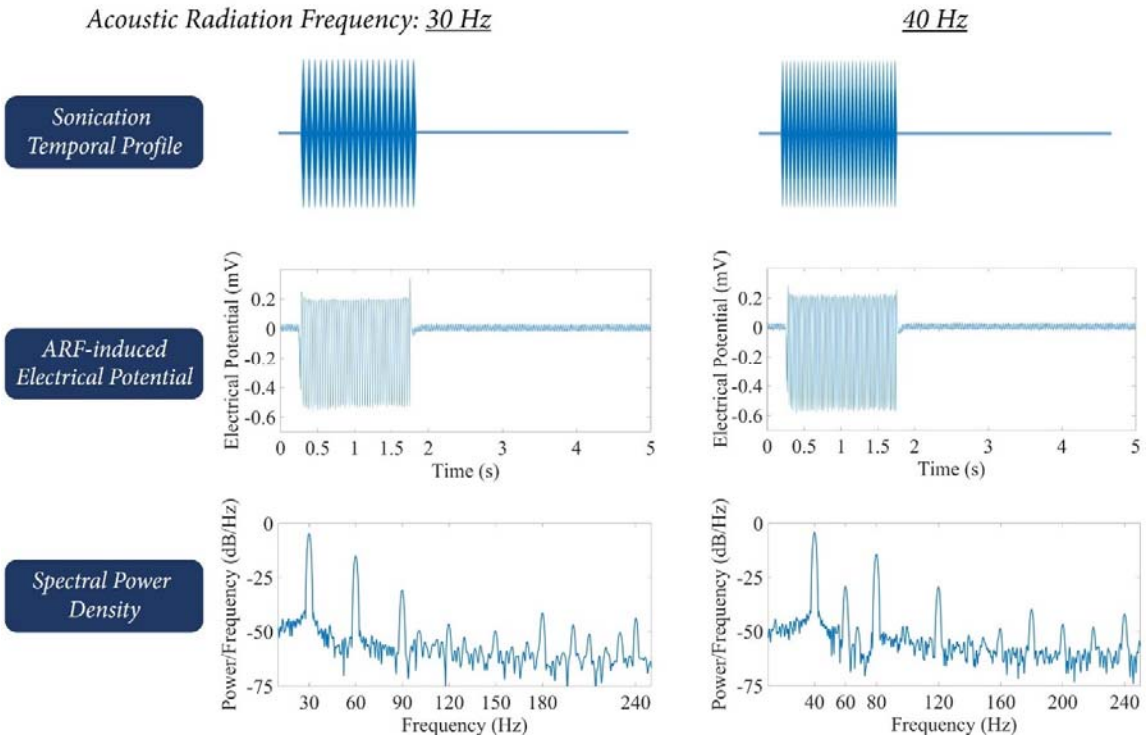

Figure 26. The ultrasound temporal profile and the recorded electrical signals with their spectral component analysis.

Furthermore, I characterized the spatial specificities of the induced Lorentz current in freshly excised rat brains after euthanizing the rat subjects. As shown in Fig. 27a, the electrode's pair is moving axially following the arrow in the phantom (in blue color), and from the spectral power densities, it can be seen that the axial spatial specificity (-3 dB) is about 2.2 mm (Fig. 27b). Next, one of the electrodes is step-wisely moving away from the fixed electrode (Fig. 27c), and it thus can be found that the lateral power density decreasing rate is about 6 dB/Hz per millimeter (Fig. 27d).

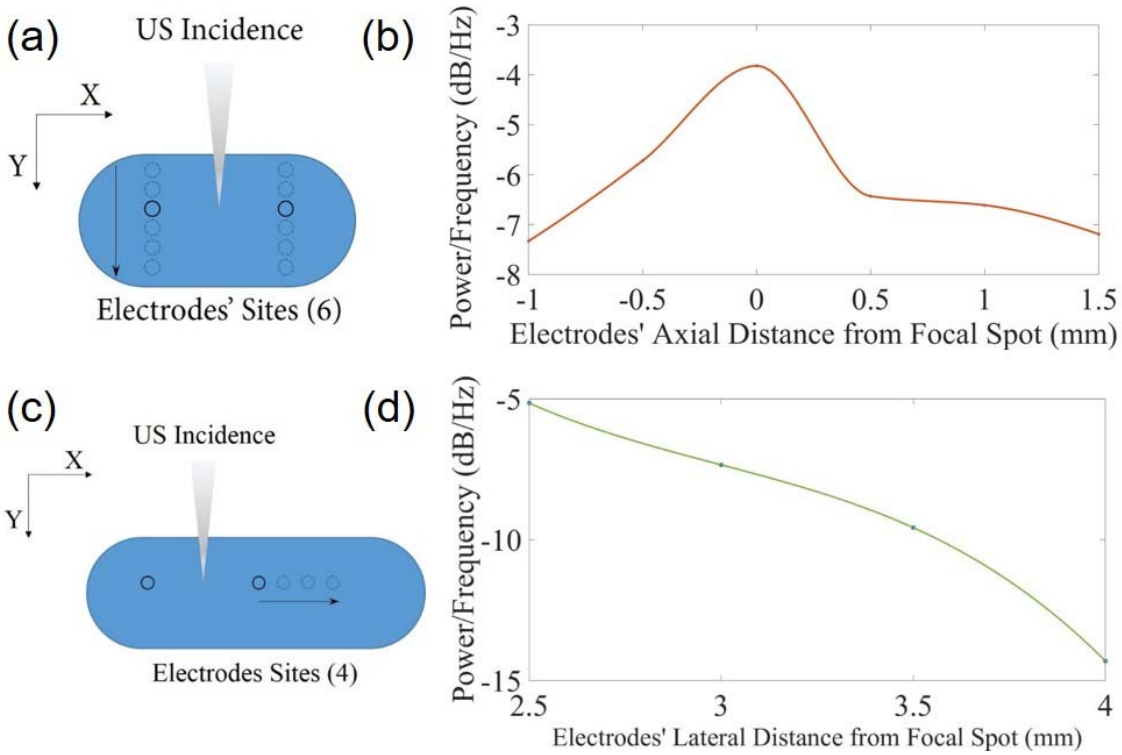

Figure 27. The spatial specificity of the Lorentz current characterized in the axial direction (a-b), and in the lateral direction (c-d).

4.2.3 Preliminary Results

Following the characterization on excised brain samples, I also tested the Lorentz current neuromodulation on *in vivo* rat model with stimulated by a single-element transducer and recorded by concurrent 24-channel scalp EEG recordings (Fig. 28a). The protocols on sonication setup, *in vivo* rat model preparation, and electrophysiological signal detection and preprocessing will be further described in section 4.3. The 50 ms sonication (Fig. 28b) consists of repetitions of the single pulses with each lasting about 70 μs (Fig. 28c), and the peak-to-peak ultrasound pressure measured by a needle hydrophone is about 80 kPa. The butterfly plots

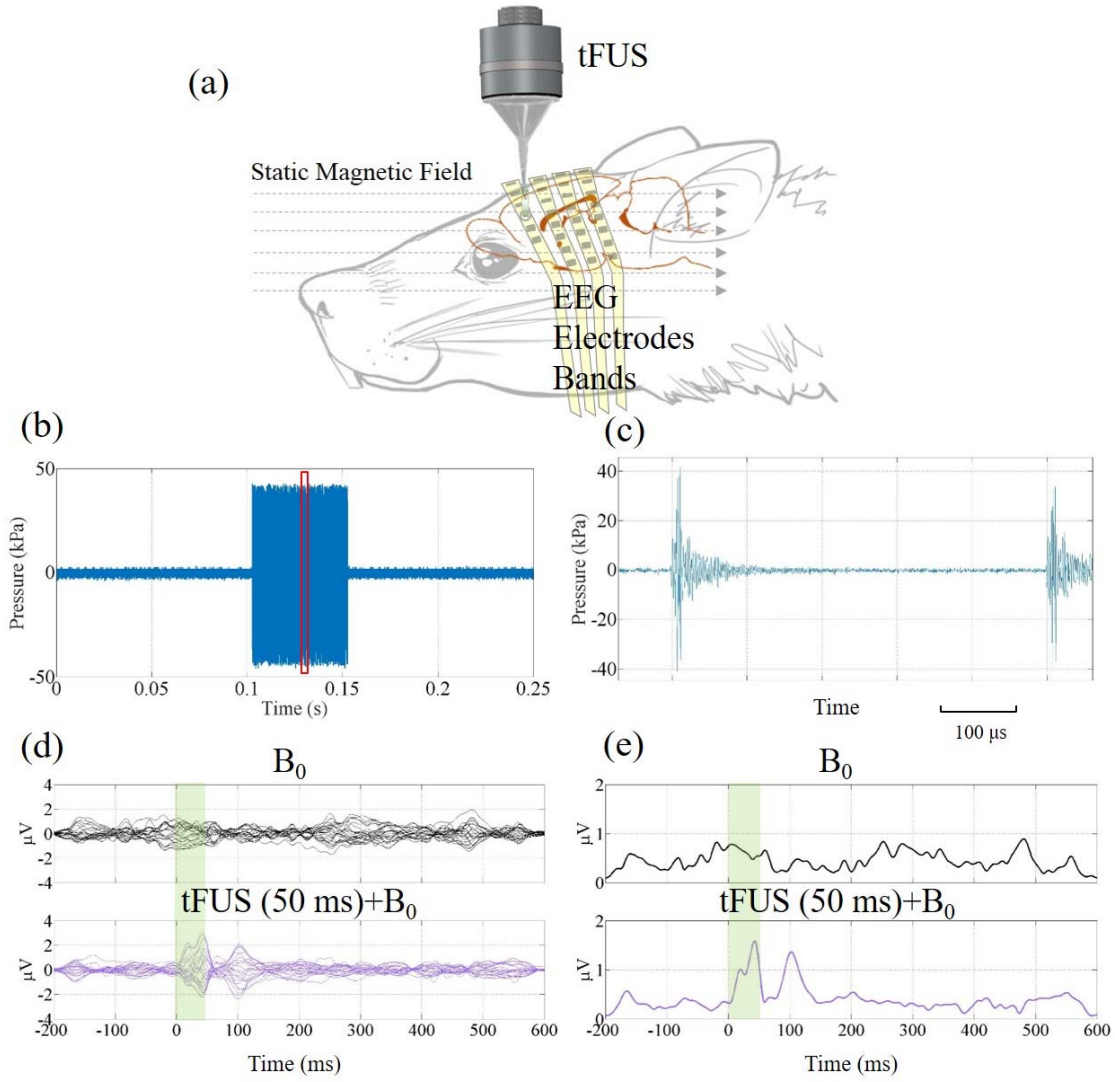

Figure 28. *In vivo* test of Lorentz-current brain stimulation. (a) *In vivo* anesthetized rat experiment setup. (b-c) The temporal profiles of transmitted ultrasound by a single-element transducer. (c) is a zoom-in profile of the red-boxed region in (b) showing the single ultrasound pulses. (d) 24-channel EEG butterfly plots for the baseline and tFUS. (e) Mean global field power of EEG for the baseline and tFUS. The green bars in (d) and (e) indicate the sonication period.

stack those original EEG signals together while the mean global field power (MGFP) demonstrate the distinct features of electrophysiological signals comparing the baseline condition (only with static magnetic field) to the tFUS

condition (combining the ultrasound with the magnetic field) (Fig. 28d-e). Notably, the time-locked brain responses in both plots may indicate the neural neuromodulatory effects potentially induced by the Lorentz current.

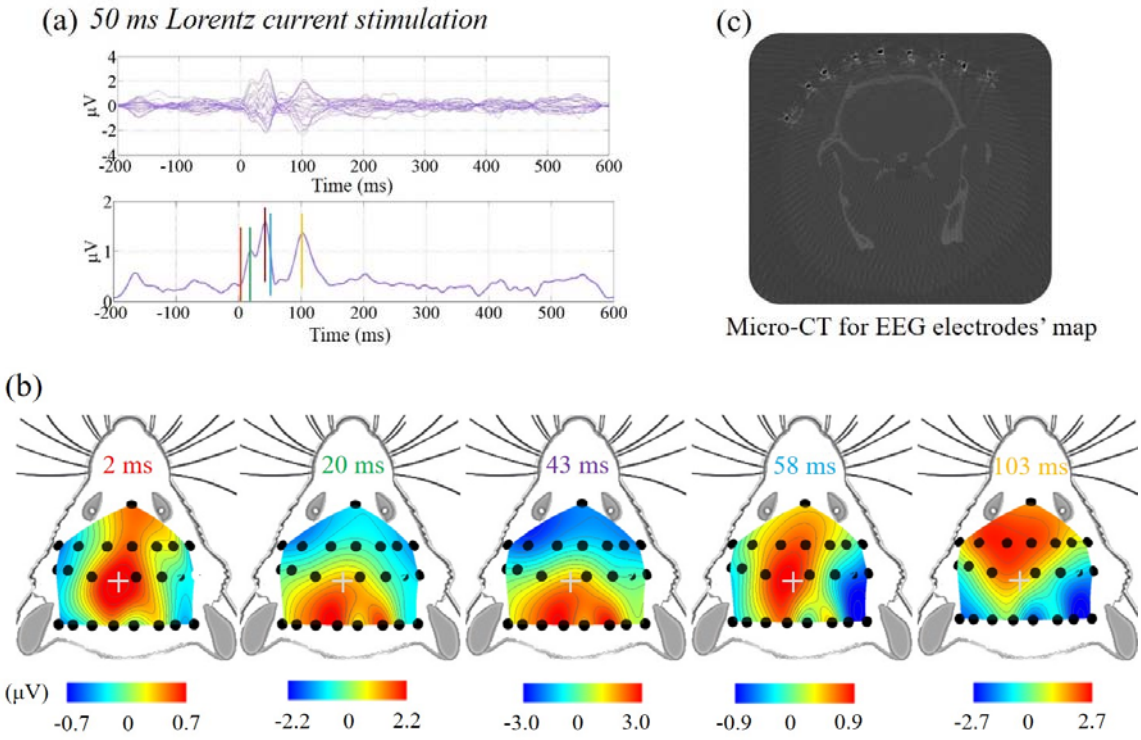

Figure 29. The tFUS perturbation-based brain mapping. (a) The butterfly and MGFP plots capture a global response to the 50 ms Lorentz current stimulation. (b) Time frames of topographic voltage map spanning from at an initial time (2 ms) to a post-stimulus time (103) ms. Each map is corresponding to the time line indicated with same color. The grey crosses in these maps indicate the sonication site. (c) The EEG electrodes' locations are mapped with micro-CT images.

Moreover, Fig. 29b depicts a series of topographic voltage maps at 2, 20, 43, 58, and 103 ms relative to time of the sonication onset (0 ms). It can be observed that the initial focal activation aligns the sonication site; however, such an activation has its dynamics of rapidly propagating to other brain areas. Using the scalp electrophysiological recordings empower a high temporal resolution to potentially identify the tFUS-evoked brain dynamics. To obtain precise topo maps, the locations of EEG electrodes are estimated with micro-CT images acquired by a Siemens Inveon preclinical microPET/CT (University Imaging Center, UMN).

Still, there are two major issues of this “Lorentz current stimulation” study. One issue is that the topography is not able to present high spatial resolution; and the other one is that the tFUS *per se* may also lead to brain activation, which means that the observed brain activations (Fig. 29a) may be attributed to the mechanical effects conferred by the tFUS. For these reasons, by collaborating with my lab colleague, Abbas Sohrabpour for further investigations.

4.3 Non-invasive EEG Source Imaging of Brain Activations by Low-intensity tFUS

There is an unanswered question whether low-intensity tFUS (much lower than FDA’s regulations) can induce EEG responses over the scalp or not. We report our experimental study to noninvasively detect and localize brain activity from scalp EEG following low-intensity tFUS in an *in vivo* rat model. In this section, I will review my collaborative work on using EEG-based source imaging to globally

map the tFUS-induced brain responses with high temporal resolution and improved spatial definition.

4.3.1 Sonication Setup

tFUS pulses were produced in a burst mode by a single-element focused ultrasound transducer (V389, Olympus, USA) and were employed to perturb the intact rat brain in anesthesia, as shown in Fig. 30. This ultrasound transducer has a diameter of 38.1 mm, a center frequency of 500 kHz, a -6 dB bandwidth of 300-690 kHz and a nominal focal distance of 55 mm. The transducer is controlled by two function generators (33220A, Keysight Technologies, USA) that manage the time sequence of ultrasonic output, so as to produce a specified time burst of pulses with 2 kHz pulse repetition frequency (PRF) in 3 s inter-sonication intervals. Such ultrasound temporal protocol was developed following Tufail *et al*. [186, 187] and Yoo *et al*. [99, 102]. Instead of tone burst mode (i.e. tens of cycles in each pulse duration) used in their experiments, in this present study we used the single-pulse burst mode as shown in Fig.30 to significantly reduce the I_{spta} and I_{sppa}. These pulses triggered an ultrasonic pulser unit (5077PR, Olympus NDT, USA), which controlled the voltage amplitudes fed into the transducer. To guide the ultrasound energy onto a certain brain location, a customized conical ultrasound collimator was fabricated using a polypropylene funnel and a polytetrafluoroethylene cylindrical tube, and was then filled with ultrasound coupling gel (Aquasonic 100 Ultrasound Transmission Gel, Parker Laboratories, USA). This collimator had an inner diameter of 1.7 mm at its tip, and its total length equaled the focal distance of the transducer. The directed acoustic intensities (I_{spta}: 0.1-0.6 mW/cm^2, I_{sppa}:

0.74-4.6 mW/cm^2, spatial-peak temporal-peak intensity I_{sptp}: 38-252 mW/cm^2, corresponding to spatial peak rarefactional pressure P_r amplitude of 18.3-45.9 kPa) transported through the collimator were then measured using a calibrated hydrophone (HNR500, Onda, USA) placed behind a piece of freshly excised Wistar rat skull. To measure such ultra-low intensity, a calibrated, broadband hydrophone preamplifier (AH-2010-025, Onda, USA) was also employed. Notably, the administered ultrasound intensities were far less than the safety limit, i.e. I_{spta} of 720 mW/cm^2 and I_{sppa} of 190 W/cm^2, used in ultrasound diagnostic imaging systems, set forth by the U.S. Food and Drug Administration (FDA) [188, 189]. By further measuring the acoustic pressure directly at the tip of the collimator, the ultrasound insertion loss as calculated for the pressure, was approximately -14 dB across the sites on the skull where the transducer would be placed in our

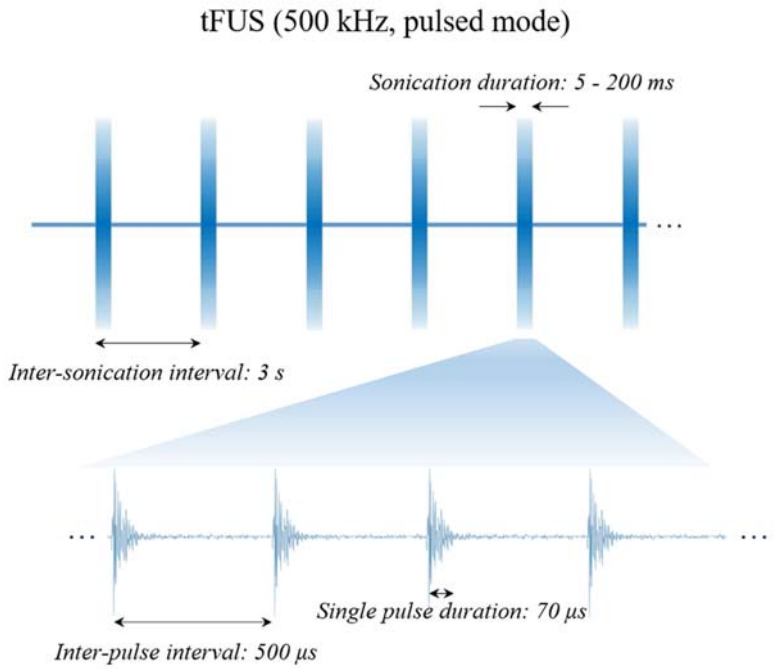

Figure 30. The sonication waveforms used in the *in vivo* experiment. (© 2016 IEEE)

experiment. The collimator, the skull sample and the needle hydrophone were aligned using a 3-axis positioning stage. This positioning stage was controlled by a stepper motor system, and was also used to aim the ultrasound transducer and collimator to a specific scalp region during the *in vivo* experiments.

4.3.2 *In vivo* Rat Model

The Wistar rat was chosen for the *in vivo* study mainly due to its relatively big cranial size and thinner skull among the rat species. Three one-year-old rat subjects were used, and each was anesthetized using katamine/xylazine mixture (75 mg/kg and 10 mg/kg respectively) with certain dosage determined by both the rat's weight and the anesthetic duration (2-3 hours). The hair over the rat's scalp, the nape, hind limbs and caudal regions were carefully removed using an electric hair trimmer and a hair remover cream lotion, to expose the skin. After the exposed skin was further degreased using alcoholic pads, and the impedance was lowered using skin prep gel, EEG and ECG electrodes were then attached to the treated skin regions, accordingly. During the experiment, a rectal thermometer and a

Table 1. Ultrasound Parameters for Three Sonication Intensities (SI) (© 2016 IEEE)

Parameters	SI 1	SI 2	SI 3
I_{spta} (mW/cm^2)	0.1	0.2	0.6
I_{sppa} (mW/cm^2)	0.7	1.4	4.6
I_{sptp} (mW/cm^2)	38	83	252
P_r (kPa)	18.3	27.9	45.9
P_p (kPa) [a]	16.1	22.8	42.8

[a] P_p: spatial-peak positive pressure amplitude.

heating lamp were used to monitor and maintain the rat body temperature. This experiment protocol was approved by the University of Minnesota Institutional Animal Care and Use Committee.

4.3.3 Electrophysiological Signal Detection and Preprocessing

All the electrophysiological signals were acquired, amplified, filtered and digitized using a multi-channel NeuroScan system (Synamps 2, Compumedics, USA) with a sampling rate of 1 kHz. The EEG was simultaneously recorded and synchronized with the ultrasound system so as to know exactly when the sonication pulses were administered. During the data acquisition, the bandpass filters with respective cutoff frequencies were applied to EEG, and ECG channels. 8-channel EEG recordings were used to assess the effect of sonication intensity on brain activation, and 16-channel EEG recordings were used to measure the spatiotemporal distribution of the brain electrical activity as induced by tFUS. EEG data were further bandpass filtered and preprocessed for source imaging analysis. The epochs of ultrasonic stimulations were aligned by using the event markers transmitted by the function generator in the sonication setup. Additionally, the short-time Fourier transform (STFT) of the mean global field power (MGFP) of the averaged ERP was also plotted using a Hamming window of length 32 ms and overlap of 4 ms.

A sham condition was designed by removing the ultrasound collimator and turning the transducer away from the rat scalp while transmitting ultrasound pulses. In order to only image the brain activity due to sonication and to reduce the effect of common activity perceived in the sham condition, the common components of

activity observed in the sham condition were removed from the ERP signals prior to source imaging. Auditory pathways may be activated during the ultrasound pulse generation, as animals like rat are capable of hearing frequency ranges much higher than human beings [190]. This was achieved by performing the principal component analysis (PCA) and identifying components demonstrating a high correlation with the sham components. Independent component analysis (ICA) [191] can be used to perform this analysis, as well. ICA is a promising method when dealing with artefacts, since such interferences are independent of the brain activity and ICA is efficient in detecting and removing those signals. Mainly the interferences can be roughly categorized as physiological artefacts such as eye movement, muscle contraction, and electromagnetic interferences from stimulation or 60 Hz power-line noise. In our experiment the animals were anesthetized, the aforementioned physiological artefacts were minimal and absent after averaging. Since ultrasound stimulation was administered, no electromagnetic interference was introduced by stimulation and power-line noise was removed with a 60-Hz notch filter. The PCA [192], however, determines main components in the data based on their strength (signal energy which is related to signal's second norm). Thus, we could compare strong components present in the two conditions, i.e. sham vs. stimulation, to reject common components which are related to background brain processes (not artefacts). For example, auditory pathways may be activated during the ultrasound pulse generation, as animals like rats are capable of hearing frequency ranges much higher than human beings. In this sense, ICA might not add an extra value for component analysis, thus PCA

and ICA could be used interchangeably and both analyses actually show many similar components.

4.3.4 EEG Source Imaging

We used a publicly available Wistar rat MRI atlas (http://www.idac.tohoku.ac.jp/bir/en/db/rb/101028.html) to build a generic boundary element method (BEM) model of the rat head, as individual head MRI was not available at the time [193]. The BEM head model consisted of three layers of tissue, namely, the skin, the skull and the brain with conductivities of 0.33 S/m, 0.0165 S/m and 0.33 S/m, respectively [194-196]. The minimum norm (MN) algorithm [197] was used to solve the inverse problem. As mentioned previously using PCA, the components of the EEG signal that were highly correlated with the EEG recorded during the sham condition were removed from the EEG prior to source analysis. The source imaging was performed for the duration of the sonication and after cessation of stimulation, for about several hundreds of milliseconds.

4.3.5 Statistical Testing

In order to test the significance of the results when comparing ERP signals to the sham condition, we performed statistical testing to determine time intervals at which the ERP signals and the sham condition were significantly different ($p<0.025$). We performed a paired t-test to this end. The data recorded at different channels of the EEG were treated as samples drawn from the two conditions (sham vs. ERP induced by sonication). The amplitudes of the signal in the two

conditions were compared over time to find time intervals at which a significance of ($p<0.025$) was achieved [97, 106, 198].

4.3.6 Results

Fig. 31 shows the 8-channel scalp EEG recordings of the tFUS-evoked brain activities in a rat from three ultrasound intensities (as listed in Table I) used

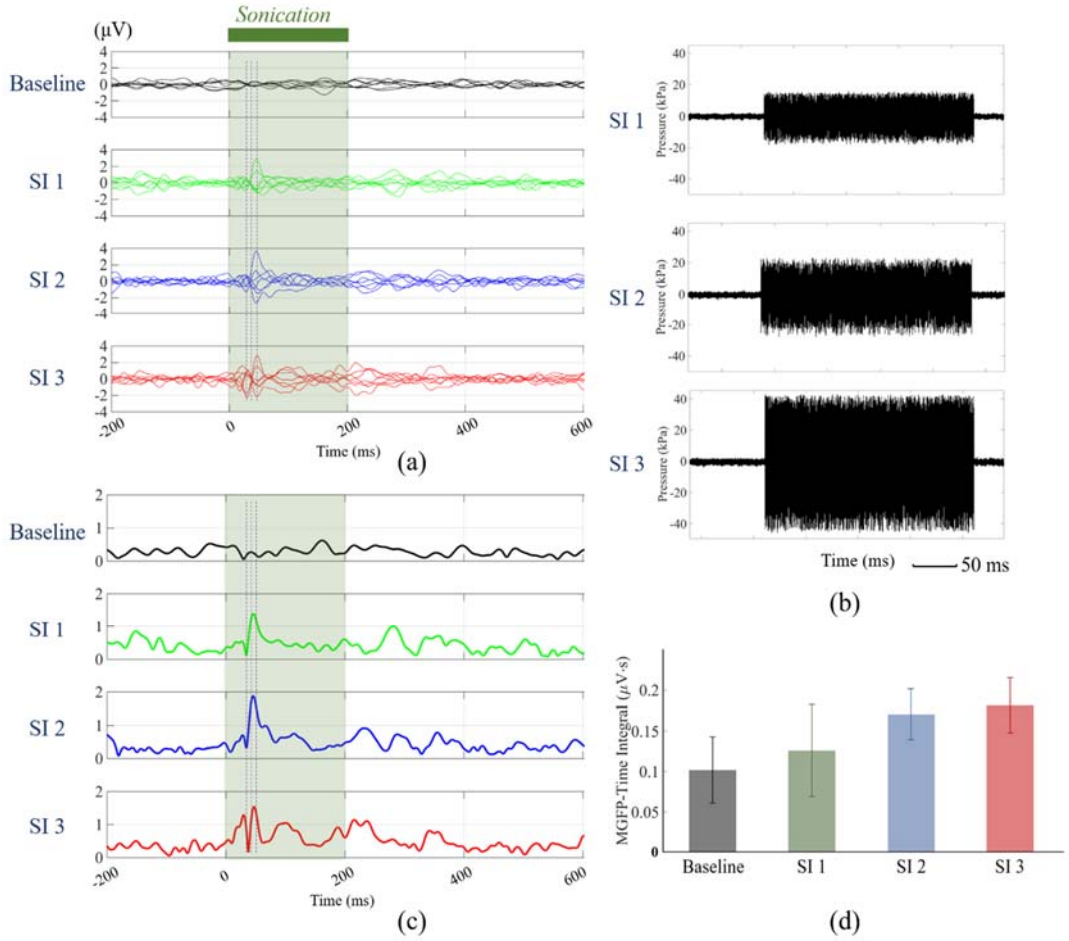

Figure 31. tFUS-evoked brain activities induced by three sonication intensities (as shown in Table I) recorded by 8-channel scalp EEG. (a) Butterfly plots of EEG waveforms, (b) ultrasound pressure-time plots for each sonication intensity, (c) EEG MGFP plots, and (d) a bar plot of averages of MGFP-time integral values with standard deviations among trials. (© 2016 IEEE)

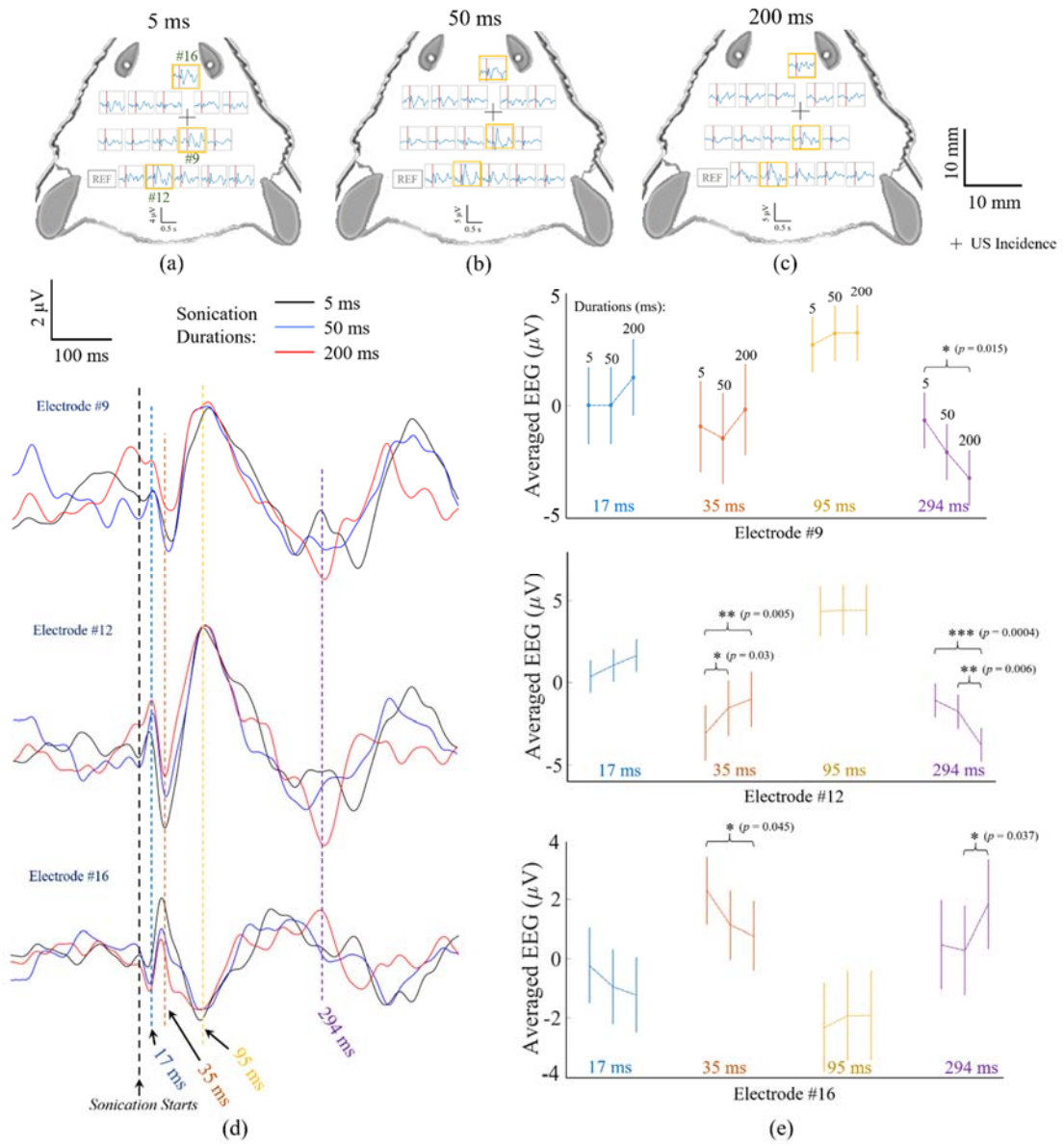

Figure 32. Averages of ultrasound-induced electrical potentials recorded with a 16-channel EEG. These potentials are in response to (a) 5 ms, (b) 50 ms, and (c) 200 ms sonication conditions in a top-view of the rat head. The channels indicated by the orange squares, i.e. electrode #9, #12, and #16 are shown at a higher gain in (d), in which the EEG recordings with three sonication durations are plotted for each electrode. The vertical dotted lines demonstrate the time points (17, 35, 95 and 294 ms) of interests at which the peaks of neural activity locate, and those average values and standard deviations are depicted in (e). The t-tests with p values indicate significant effects of sonication durations in each electrode as presented in (e). (© 2016 IEEE)

to sonicate the targeted right anterior cortex. These intensities are due to three different excitation voltages that drive the transducer. After averaging across 300 trials, the results are illustrated in the time course (from -200 to 600 ms, 0 ms indicates the onset of the 200-ms sonication) both with butterfly plots and MGFP plots. Fig. 31 indicates that even when a low-intensity sonication (I_{spta}: 0.1 mW/cm^2, I_{sppa}: 0.7 mW/cm^2) is administered with the applied ultrasound pressure recorded in Fig. 2(b), the rat brain shows an observable time-locked activation as perceivable in the EEG. When increasing the input ultrasound intensities, the recorded EEG shows increasing response amplitudes and extended activations as depicted in Figs. 31(a) and (c). If one takes the time integral of the MGFP within the sonication duration of 200 ms, the results demonstrate an increasing trend shown in Fig. 31(d). These integral values are calculated using trapezoidal integration method with an integration step of 1 ms.

Fig. 32 shows 16-channel scalp ERPs averaged from 600 trials of another rat subject. The channels indicated by the orange squares, i.e. electrode #9, #12, and #16 are further magnified in Fig. 32(d), in which the neural recording under three sonication durations are plotted for each electrode. Within sonication period, all those three conditions use acoustic intensity I_{spta} of 0.6 mW/cm^2 (I_{sppa}: 4.6 mW/cm^2, I_{sptp}: 252 mW/cm^2) when the tFUS wave reaches the skull covering the targeted cortical region. The vertical dotted lines in Fig. 32(d) show the time points of interest at the extrema of neural activity time course. Fig. 32(e) depicts the averaged signal values and standard deviations at the four time points (i.e. 17, 35, 95 and 294 ms) read from the three individual EEG electrodes (indicated by orange

squares in Fig. 32(a)(b)(c)). Significant differences exist at 294 ms among three sonication durations from recorded signals by three electrodes. Electrodes #12 and #16 also present significant differences at 35 ms in the signal profiles by the 5-ms and 200-ms sonication durations.

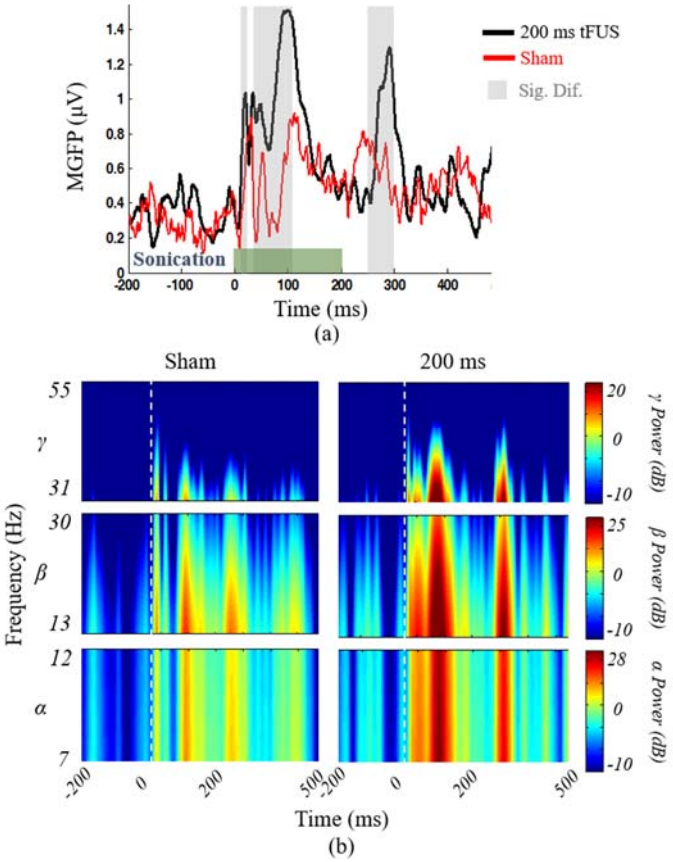

Figure 33. Comparing the brain activity during sonication with the sham condition. (a) The MGFP is depicted for the two conditions, namely the 200 ms sonication (Ispta: 0.6 mW/cm^2, Isppa: 4.6 mW/cm^2, Isptp: 252 mW/cm^2) and sham. The green bar indicates the duration for which the tFUS was administered (200 ms) and the gray bars indicate the time intervals during which the amplitude of the EEG signal was statistically different for the two conditions ($p<0.025$). (b) The short-time Fourier transform of the MGFP of the two conditions is calculated and compared against each other. (© 2016 IEEE)

Inevitably, the audible sound from tFUS may also result in auditory evoked potentials. In the *in vivo* experiment, during the sham condition, the transducer keeps transmitting ultrasound as in the stimulation session, using 200 ms sonication, while the transducer is flipped to point away from the animal. Fig. 33(a) depicts the MGFP values of the 16-channel EEG recordings of the sham ultrasound condition (red), and its comparison to the 200 ms tFUS condition (black). The gray vertical bars at 8-19 ms, 33-109 ms, and 267-311 ms indicate significant differences (paired t-test, $p<0.025$) in the amplitude of evoked neural signals between the sham and the transcranial sonication conditions. Fig. 33(b) shows the time-frequency plots depicting the spectral contents in α (7-12 Hz), β (13-30 Hz), and lower γ (31-55 Hz) frequency bands of the elicited brain activity after the onset (dashed vertical lines) of the sonication. Compared to the sham condition, we also found significant differences existing within each frequency band during 0-100 ms and 200-250 ms produced by the 200 ms tFUS. Hence, based on the analyses of global field power and spectral power, the tFUS-evoked brain activities can be distinguished from the sham condition.

Signals from the sham condition have been subtracted from the recordings with the tFUS condition. Solving the inverse problem using the MN method, the EEG source images were obtained to estimate the spatial location of the

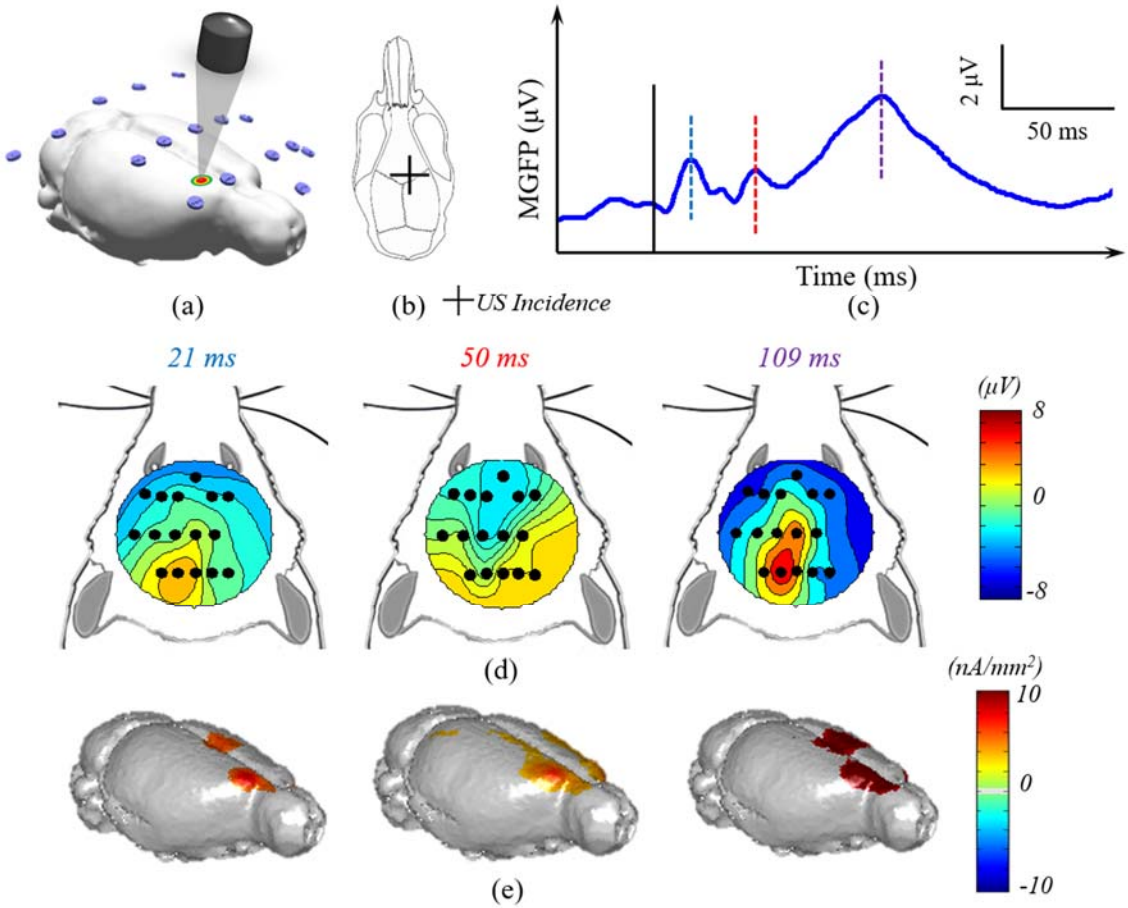

Figure 34. ESI neuroimaging of brain activity induced by the 200 ms low-intensity tFUS stimulation at the right anterior cortex in a rat. In this experiment, the tFUS transducer was placed over the right hemisphere as indicated in the 3D model (a), and the schematic diagram (b), where the cross depicts the placement of ultrasound transducer. The MGFP of the recorded EEG signal (c), in which the black solid line indicates the onset of sonication, and the blue, red and purple dashed lines represent the temporal instances of relative peaks in the MGFP (21 ms, 50 ms, and 109 ms). The topographical voltage maps (d) and source images (e) of these instances are depicted correspondingly. (© 2016 IEEE)

ultrasound perturbation and its induced brain activation. In the presented ESI results, we found that the estimated source covered cortical regions including the targeted region of the ultrasound beam. Further, a series of EEG topographic voltage maps and source images at several time points of relative signal peaks (21, 50, 109 ms) in the MGFP plot are depicted in Fig. 34(c), (d) and (e), while the relative locations of the rat brain, the cranial bone, the ultrasound incidence, and the EEG electrodes are shown in Fig. 34(a) and (b), respectively. From the presented source images (Fig. 34(e)), the location of the initial activation (21 ms) aligns with the ultrasound targeting region, and this activation soon propagates to the surrounding cortical regions (50 ms). Because the tFUS keeps depositing mechanical energy during the sonication period, the brain activation source stays at the right anterior cortical region (50 and 109 ms), and meanwhile several other cortical areas become active successively.

When the same ultrasound beam is directed at another anterior cortical region which is more lateral, the ultrasound intensity reaching the brain tissue would be even less due to an increasing skull thickness of the rat cranium. Therefore, the amplitudes decrease as observed in the topographic voltage maps and the EEG source imaging results (Fig. 35(d) and (e)). From these results, it is shown once more that the initiation region of cortical activation (17 ms) follows the ultrasound incidence site, and later at 68 ms, this source activation propagates to other brain regions while the initiation region remains being activated by the ongoing ultrasound stimulation.

A third rat was also studied using the same sonication condition as harnessed in Figs. 34-35, whereas ultrasound incidence site was changed to the

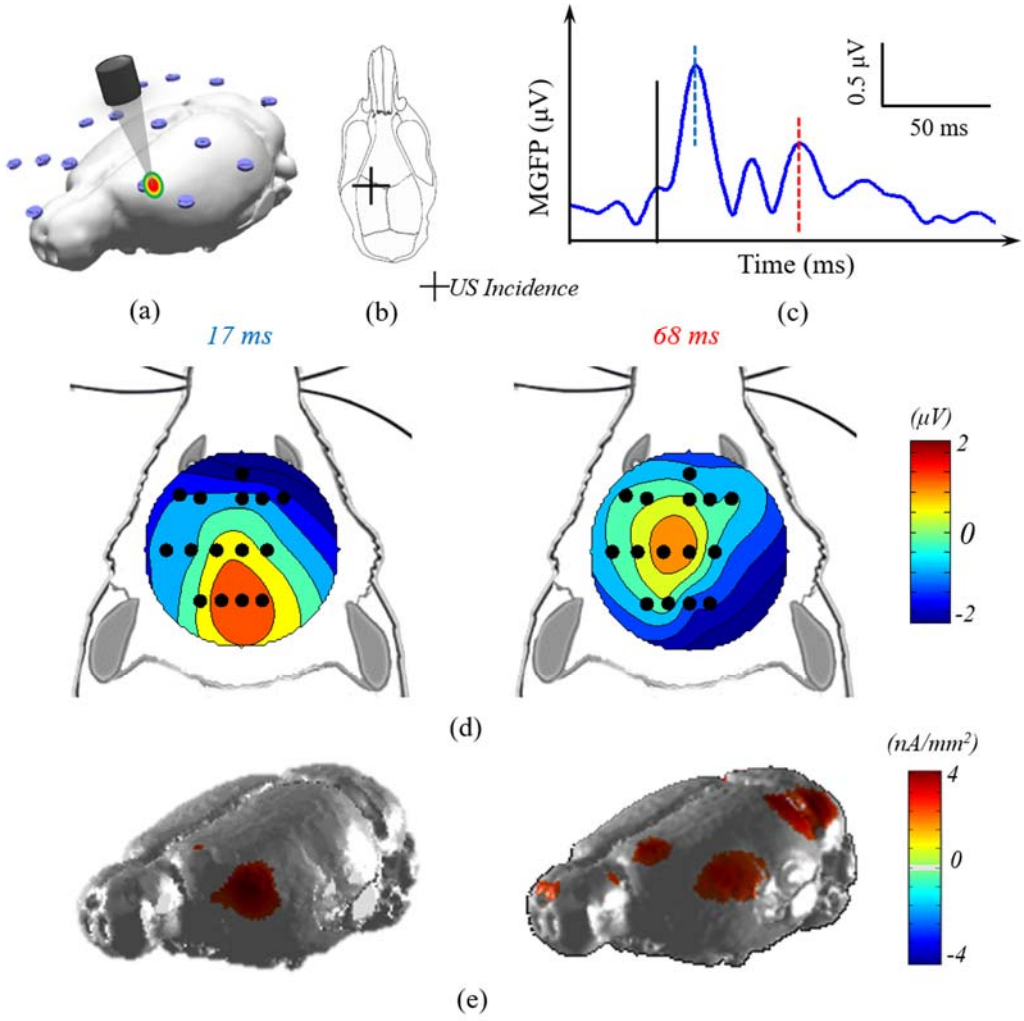

Figure 35. ESI neuroimaging of brain activity induced by the 200 ms low-intensity tFUS stimulation at the left anterior cortex of a rat. In this experiment, the tFUS transducer was placed over the left hemisphere as indicated in the 3D model (a) and the schematic diagram (b), where the cross depicts the placement of ultrasound transducer. The MGFP of the recorded EEG signal (c), in which the black solid line indicated the onset of sonication, and the blue and red dashed lines points to the temporal instances of the relative peaks in the MGFP (17 ms, and 68 ms). The topographical voltage maps (d) and source images (e) of these instances are depicted correspondingly. (© 2016 IEEE)

location of electrode #9 as mapped in Fig. 32(a). Similar ESI results were observed in this case comparable to other two animals (data not shown).

4.4 Discussion

We have conducted an experimental investigation to demonstrate the feasibility of noninvasively recording brain electrical activity as induced by low-intensity tFUS in an *in vivo* animal model. We have also demonstrated, for the first time, that it is possible to image brain electrical activity from noninvasive scalp EEG recordings following tFUS perturbation. Our results suggest that ESI may become a useful tool to derive biomarkers to quantify tFUS effects and guide its use for neuromodulation. Such noninvasive biomarker, while obtained in real time, may offer important insights to optimize tFUS stimulation parameters and make tFUS a closed-loop neuromodulation modality.

Our work also suggests using tFUS as an important guide for perturbation based neuroimaging. In perturbation based neuroimaging [85], external energy is applied to alter the neural information processing; the spatio-temporal activation patterns as altered due to such perturbations, can then be used to identify and delineate the mechanisms of neural activation and pathology. For this purpose, it is important to use low intensity neuromodulation so the injected energy will only present perturbations to avoid global and wide-spread effects.

In our work, using a single-element focused ultrasound transducer with a collimator, we introduced the low-intensity tFUS (I_{spta} as low as 0.1 mW/cm^2, and I_{sppa} as low as 0.7 mW/cm^2) as a brain perturbation tool and demonstrated the

capability of noninvasively recording electrophysiological responses of the brain following such low-intensity tFUS perturbation. By stimulating multiple sites and localizing the initiation site of the induced activity, our results confirmed such local activation can be noninvasively recorded and localized to the target site (corresponding to tFUS beam) by means of ESI.

Considering the different skull thicknesses in various *in vivo* animal models or human subjects, one may need to compare the ultrasound intensities at the brain tissue (as opposed to ultrasound pressure at the scalp). In our *in vivo* rat experiment for tFUS-ESI, the applied I_{spta} (0.1-0.6 mW/cm^2) is much lower than the lowest ultrasound spatial-peak temporal-average intensity (13.5±3.8 mW/cm^2) ever reported in the past *in vivo* studies [101], to the best of our knowledge. For the neuroimaging purpose, such ultra-low intensity tFUS shall not damage the brain, but is still able to perturb the brain network. The present experiment has identified a low but effective tFUS intensity for EEG source imaging. Additionally, the ultrasound spatial-peak temporal-average intensity of less than 1 mW/cm^2 (at the tip of collimator) ensures the non-invasive merit of tFUS (such level of stimulation did not induce other physiological activities such as leg movement, as the EMG did not show any detectable signal at both hind limbs). However, these parameters (at the tip of collimator and at the cortex) would need to be modified and scaled up, if to be used for human experiments.

In our experiment, the fundamental ultrasound frequency used was 500 kHz, which may not be an optimal choice in terms of eliciting behavioral changes and neuromodulation. Some previous studies aiming to study effective ultrasound

parameters, to maximize sensorimotor responses in rats, reported that frequencies lower than 500 kHz were more effective in eliciting stronger EMG responses [129]. However, as lower frequencies lead to poorer ultrasound spatial specificity, a trade-off between the stimulating efficiency and spatial focality exists. Further investigation on effective frequencies needs to be done on an application-specific manner, as effective frequencies that elicit maximal behavioral responses, might be different for different networks in the brain.

Our results, in general, support the hypothesis that tFUS-induced brain activity is generated from the point of cortex targeted by the ultrasound beam and propagates to surrounding tissue. Since the ultrasound transducer was not targeted at a specific location of cortex, and low intensity ultrasound (I_{spta}<1 mW/cm^2) was used in the *in vivo* rat experiment, no behavioral change was observed. Our results indicate a focus of activity forming under the ultrasound collimator on the cortex and its later propagation to nearby tissue. This is the first evidence of ultrasound-induced electrical activity captured non-invasively by dynamic EEG source imaging in a living system, to the best of our knowledge.

While tFUS has been used in recent years to modulate and study the brain [97, 103, 106, 187] the neural effect induced by tFUS remains unclear [199, 200]. Use of ESI represents an opportunity to delineate the mechanism of tFUS by noninvasively mapping the spatio-temporal patterns of brain activation induced by tFUS. The specificity of tFUS and its ability to form concentrated foci, makes the combination of tFUS and ESI an ideal tool for noninvasively studying the brain. Using ESI to monitor the effects of tFUS stimulation can help not only in

determining the nature of neuromodulation therapies performed by ultrasound, but also to be used to study normal brain networks by exciting or inhibiting different brain locations [99], i.e. network nodes. Another impact of using ESI technique in ultrasound neuromodulation is that ESI is able to non-invasively document the targeted brain region by the transducer, which is considered as one of the challenges for ultrasound neuromodulation research.

Ultrasound has also been used to treat pathological brain conditions. An early study by Manlapaz *et al*. [201] on a feline model provided experimental evidence as to the efficacy of ultrasound-induced attenuation of seizure activity and consequently decreased morbidity. A relatively high acoustic intensity of 840 W/cm^2 with a fundamental acoustic frequency of 2.7 MHz was used in the aforementioned study. More recently Min *et al*. [202] reported on a rat model having pentylenetetrazol-induced epileptic activity; the sonication (I_{spta}: 130 mW/cm^2) was shown to be successful in suppressing the occurrence of epileptic EEG bursts as observed in subdermal two-channel EEG recordings. These *in vivo* studies show the value of tFUS as a neuromodulation tool. Combined with ESI, the target to be stimulated by tFUS can be determined from electrophysiological recordings, thus allowing precision neuromodulation by assessing the tFUS effects. After tFUS is administered, the pathological activity, e.g. seizure, can be monitored by ESI to study the prognosis of stimulation and treatment efficacy.

While the EEG was used to record and image brain activity as induced by tFUS in the present study, it is anticipated that one can use magnetoencephalography (MEG) [30] to record and image brain activity induced

by tFUS. Such demonstration shall be interesting for further investigation, and the present results indicate such possibility [1].

4.5 tFUS-ESI on Human Subject: A Pilot Study

One of the most attractive advantages of tFUS is the non-invasiveness. Thus, to fully harness such merit for human applications, the non-invasive brain mapping approach, ESI is the one that has great promise working seamlessly with tFUS. The outstanding compatibility in a natural setting will facilitate the tFUS-ESI to become an effective combination for a translational use on humans. In a collaborative research experiment at Dr. Wynn Legon's lab, we tested the tFUS-ESI framework on a human subject. Following the similar protocol of experiment setup as reported in [97] without median nerve stimulation. As demonstrated in Fig. 36, a single-element US transducer was placed over the motor cortex and 500

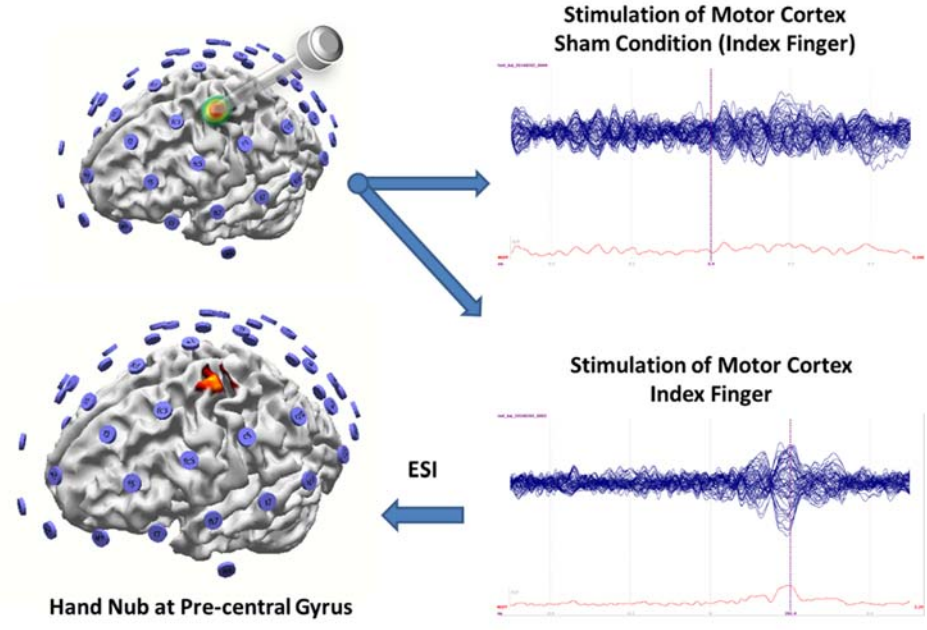

Figure 36. tFUS stimulation in human (left upper) and ESI mapping of tFUS induced brain activity (left bottom). The brain model is reconstructed from 3 Tesla MR images of the subject.

pulses (pulse duration: 360 μs, PRF: 1 kHz) are transmitted at I_{sppa} of 15.04 W/cm^2 with 500 kHz central frequency (upper left) while the multi-channel EEG is being recorded simultaneously. The sonication interval is generated randomly between 6-10 s. The hand nub of the motor cortex is located using TMS stimulations and EMG monitoring, to detect index finger movement. Once the EEG is epoched and averaged around the tFUS stimulation instances, evoked potentials can be detected (lower right). The transducer was turned 180 degrees facing away from the scalp, and the stimulations were applied for the sham condition. No evoked potentials are observed (upper right). ESI imaging was performed, and the activated cortical area is localized to the hand nub of the pre-central gyrus (lower left). This promising preliminary human result demonstrates the merits and feasibility of the proposed ESI-tFUS as applied to human neuroscience. And in the meanwhile, real-time ESI may become an effective tool to non-invasively monitor the brain responses to the deposited ultrasound energy, which is deemed to lead a revolution for a high-spatiotemporal resolution brain mapping technique.

Chapter 5. Towards the Mechanism of Ultrasound Neuromodulation

5.1 Introduction

In concert with efforts pursuing agent-dependent enhancement of ultrasound modulation specificity, exploring ultrasound's intrinsic cell-type selectivity may pave the way for the translation of tFUS as an effective non-invasive modulation tool for brain stimulation and elucidating neural mechanisms. A unifying theoretical framework was formulated in order to map the acoustic parameters that lead to neuronal activation/suppression effects through cortical stimulation results based on their neuronal intramembrane cavitation excitation (NICE) model [203, 204]. While further validations are necessary, certain cell-type-selective effects are predicted by this model when T-type calcium channels, existing in both cardiac and central nervous systems, are added in the neuronal modeling [203]. Inspired by this work and the increasing number of studies demonstrating ion channel dynamics as the mechanism of tFUS stimulation [199, 205, 206], we investigate the cell-type dependent effects of tFUS stimulation through extracellular recordings in *in vivo* rodent brains. We hypothesize that, if the type and relative distribution of ion channels play a major role in tFUS mechanism of activating neurons, different neuronal types will have a distinct response profile to tFUS.

As a common research method, intracranial electrophysiological recordings have been used to reveal the vivid neural activities [207]. To test our hypotheses,

we explored the effects of tFUS on single neuron spiking activity through multi-channel electrical recordings, such as local field potentials (LFPs) and multiunit activities (MUAs), with high spatio-temporal resolution and measurement fidelity in *in vivo* anesthetized rodent models.

5.2 Materials and Methods

5.2.1 Experimental Model and Subject Details

Rat Subjects: Wistar outbred male rats (Hsd:WI, Envigo, USA) were used as subjects, and all rat studies were approved by the Institutional Animal Care and Use Committee at University of Minnesota in accordance with US National Institutes of Health guidelines.

Transgenic Mouse Subjects: Transgenic mice models are purchased from The Jackson Laboratory and bred to achieve the desired strains. CaMKIIa-ChR2 mice are crossed between a T29-1 parent expressing calcium/calmodulin-dependent protein kinase II alpha (CaMKIIa) promoter driving Cre recombinase expression, and an Ai32 parent, expressing channelrhodopsin-2/EYFP fusion protein following exposure to Cre recombinase. A genetically positive offspring co-expressing ChR2 in CaMKIIa neurons are identified via tail snip DNA testing using YFP as a probe. PV-ChR2 mice are crossed between a PV-Cre parent expressing Cre recombinase in parvalbumin-expressing neurons and an Ai32 parent. A genetically positive offspring co-expressing ChR2 in PV neurons are identified via fluorescent protein visualization goggles (BLS, Budapest, Hungary). The procedures are reviewed and approved by the Institutional Animal Care and Use

Committee at the University of Minnesota in accordance with US National Institutes of Health guidelines.

5.2.2 tFUS Setup and Parameter Selection

Single element focused transducers were used for tFUS stimulation. Transducer diameter 28.5 mm, ultrasound fundamental frequency (UFF) 0.5 MHz, -6 dB bandwidth 300-690 kHz, a nominal focal distance of 38 mm. (V391-SU-F1.5IN-PTF, Olympus Scientific Solutions Americas, Inc., USA). Collimators were 3D printed with VeroClear material to match the focal length of the transducer and the animal model, the outlet of the angled collimator for the rat model has an elliptical area of 25.6 mm^2, the one for the ultrasound normal incidence has a circular area of 19.64 mm^2, while the one for the mouse model has the smallest elliptical area of 5.39 mm^2. The size of collimators' outlet was set to be no less than or at least commensurate with one ultrasound wavelength (i.e. 3 mm in soft tissue). One single-channel waveform generator (33220A, Keysight Technologies, Inc., USA) was working with another double-channel generator (33612A, Keysight Technologies, Inc., USA) to control the timing of each sonication, synchronize the ultrasound transmission with neural recording, and form the initial ultrasound waveform to be amplified, thus driving the transducer. A 50-watt wide-band radio-frequency (RF) power amplifier (BBS0D3FHM, Empower RF Systems, Inc., USA) was employed to amplify the low-voltage ultrasound waveform signal. The employed ultrasound intensity levels and duty cycles are described in Table. 1. As noted in the table, all ultrasound conditions used the same UFF of 0.5 MHz,

ultrasound duration (UD, also known as sonication duration) of 67 ms, inter-sonication interval (ISoI) of 2.5 s, tone-burst duration (TBD) of 200 μs.

Table 2. Administered tFUS Conditions with Featured Parameters

tFUS Conditions*	UPRF (Hz)	UDC (%)
UPIx1	30	0.6
UPIx10	300	6
UPIx50	1,500	30
UPIx100	3,000	60
UPIx150	4,500	90

* Except for the ultrasound pulse repetition frequency (UPRF) and ultrasound duty cycle (UDC), all the listed tFUS conditions use the same UFF, UD, ISoI, TBD, I_{sptp} within each animal model. UPI stands for ultrasound pulsed intensity.

5.2.3 Extracellular Recordings

Extracellular recordings were made using 32-channel 10mm single shank electrodes, where electrode sites are arranged in 3 columns, spaced 50 microns apart from each other (A1x32-Poly3-10mm-50-177, NeuroNexus, Ann Arbor, MI, USA). Electrodes were inserted into the rodent skull using a small animal stereotaxic frame with 10-micron precision manipulators (Model 963, David Kopf Instruments, Tujunga, CA, USA). Electrodes were inserted at a 40-degree angle in the sagittal plane, in order to directly record from brain areas under peak ultrasound stimulation.

Rodents were sedated under either ketamine and xylazine cocktail or isoflurane. All animals were skin prepared with hair shaving and hair removal gel. Rodent heart rate, respiration rates and inter-rectal temperatures were monitored throughout recording. Cranial windows, 1-2 mm in diameter, are opened in the skull using a high-speed micro drill (Model 1474, David Kopf Instruments, Tujunga, CA, USA) under stereotaxic surgery assisted with microscope system (V-series otology microscope, JEDMED, St. Louis, MO, USA). Brain suture lines were used to identify brain structure locations. Recordings were obtained using the NeuroNexus Smartbox recording system (20 kHz sample frequency, 16-bit ADC, NeuroNexus, Ann Arbor, MI, USA). All mentioned procedures on rodent models have been reviewed and approved by the Institutional Animal Care and Use Committee at University of Minnesota.

5.2.4 Stimulation at Primary Somatosensory Cortex in Rats

Rat subjects were adults in the weight range of 400 g to 600 g, sedated initially under ketamine and xylazine cocktail (75 mg/kg, 10 mg/kg) and extended with ketamine injections (75 mg/kg). This sedative approach allows us to achieve stable anesthesia with minimum body movement, e.g. breathing, heat beating, *etc*. tFUS collimator is coupled with the rat skull using ultrasound gel. Ultrasound collimators are transmitted through intact skull, directed at 40 degrees angle towards the left S1 region on the rat head.

5.2.5 Stimulation at Primary Somatosensory Cortex in Transgenic Mice

Mice expressing ChR2(H134R) in select neuronal populations were achieved by crossing mice expressing ChR2 in a cre-dependent manner

(B6;129S-Gt(ROSA)26Sortm32.1(CAG-COP4*H134R/EYFP)Hze/J; Jackson labs stock number: 012569; also referred to as Ai32; donated to Jackson labs by Hongkui Zeng) with mice expressing Cre recombinase in either parvalbumin-expressing cells, including fast-spiking inhibitory interneurons (B6;129P2-Pvalbtm1(cre)Arbr/J; Jackson labs stock number: 008069 [208]; donated to Jackson labs by Silvia Arber; resulting cross referred to as PV-ChR2 in this manuscript) or in neurons expressing CaMKIIα, including RS excitatory cortical neurons (B6.Cg-Tg(Camk2a-cre)T29-1Stl/J; Jackson labs stock number: 005359[209]; donated to Jackson labs by Susumu Tonegawa; resulting cross referred to as CamKII-ChR2 in this manuscript). Opsin-expressing offspring were identified by genotyping (for CamKII-ChR2 mice; Transnetyx) or via fluorescent protein visualization goggles (BLS, Budapest, Hungary) (for PV-ChR2 animals), as done previously [210].

Recordings were performed in adult mice, males and females, older than 8 weeks old. Mice were sedated under isoflurane (4% during surgery, 2% during recording); Optoelectrodes (NeuroNexus, Ann Arbor, MI, USA) were inserted in the S1 (ML -1.5 mm, AP -1 mm, Depth 0.7 mm) at a 40-degree angle from the posterior, while tFUS was delivered at 30 degree incidence angle from the anterior in the same sagittal plane. After all tFUS recordings were performed, to avoid confounds of light delivery potentially altering neuronal firing properties, brief pulses of light (wavelength 465 nm, ≤ 10ms in duration, duration of light adjusted to avoid bursts of activity; PlexBright LED Module, Plexon, Dallas, TX, USA) were used to ‘optotag’ recorded neurons. Units which displayed an increase in firing rate

(defined as an increase above 99% confidence interval of spontaneous firing) within 10 ms of the light pulse were classified as excitatory neurons (in CamKII-ChR2 mice) or parvalbumin-expressing inhibitory neurons (in PV-ChR2 mice).

5.2.6 MUA Data Processing

For spike analysis, neural traces were band-passed between 244 Hz and 6 kHz, followed by Symlet wavelet denoising using Wavelet toolbox in MATLAB v9.0.0 (The MathWorks, Inc., Natick, MA, USA) to remove potential artifacts. All MUA spike sorting and single-unit preselection are performed using PCA based spike classification software Offline Sorter (Plexon, Dallas, TX, USA). Local field potentials (LFP) were band-passed from 1 Hz to 244 Hz, and denoised using Wiener filter and independent component analysis to generate Figure S3f. Further analyses, including the ISpI computation, PSTH, raster and return plots (also known as Poincaré plot, a second-order analysis method for nonlinear features in time series), feature extraction for the initial phase (IP) and afterhyperpolarization (AHP), descriptive statistics for spike waveform and spiking rates, LFP temporal and spectral analyses were performed using FieldTrip toolbox [211] in the MATLAB. After obtaining phase durations of IP and AHP, K-means clustering function in the MATLAB was employed to conduct the cluster analysis of neuron types.

5.2.7 Ultrasound Pressure/Intensity Mapping

In order to characterize tFUS stimulation's temporal and spatial dynamics near our targets, we developed a three-dimensional *ex-vivo* pressure mapping system that uses a water submerged needle hydrophone (HNR500, Onda

Corporation, Sunnyvale, CA USA) driven by a 3-axial positioning stage (XSlide, Velmex, Inc., Bloomfield, NY, USA) to map out the spatial-temporal pressure profiles of ultrasound transmitted through an *ex-vivo* skull. The needle hydrophone was placed beneath an *ex-vivo* skull and recorded ultrasound pressure values at discrete locations (scanning resolution: 0.25 mm laterally, 0.5 mm axially) behind the skull. Skulls were freshly dissected from euthanized animals. This setup allows us to quantify the amount of energy delivered to the brain, which varies substantially due to the inhomogeneity and aperture of the skull. The system can be set up to mimic the exact conditions of the ultrasound set up with matched collimator locations and angles.

Based on the measured 3-D ultrasonic pressure map, the spatial-peak temporal-peak intensity (I_{sptp}) is calculated using Equation 17

$$I_{sptp} = \frac{{P_0}^2}{Z_0} \tag{17}$$

where P_0 is the maximal instantaneous pressure amplitude in both spatial and temporal domains, and Z_0 is the characteristic acoustic impedance. This impedance can be computed using Equation 18

$$Z_0 = \rho \cdot c, \tag{18}$$

where ρ is the medium density (1,028 kg/m^3 for brain tissue, 1,975 kg/m^3 for cortical bone[212]), and c is the speed of sound in the medium (1,515 m/s for brain tissue, 3476 m/s for cortical bone[212]).

We can also obtain the spatial-peak temporal-average intensity (I_{spta}) from temporal profile of ultrasound pressure at its spatial maximum, which is denoted as $P(t)$. Equation 19 is used to calculate the I_{spta}.

$$I_{spta} = \int \frac{P(t)^2}{Z_0} dt \cdot UPRF \tag{19}$$

5.2.8 Ultrasound Induced Temperature Rise

As a safety concern, once obtaining the ultrasound pressure map, we did a numerical estimation of maximum temperature rise using the following calculation methods [213]. Firstly, we can obtain the I_{spta} from Equation 19, and then the rate of heat generation per volume is calculated using Equation 20.

$$\dot{\mathrm{Q}} = 2\alpha \cdot I_{spta} \tag{20}$$

Where α is the ultrasound amplitude absorption coefficient in brain tissue (0.03 Np/cm at 0.5 MHz [214]) or in cortical bone (3.45 dB/cm at 0.5 MHz [212]). Since we introduced the spatial-peak temporal-average intensity, the estimation of the Q value was maximized for the targeted site. Next, we borrowed the Equation 21 from [215] to obtain the maximum temperature increase if we assume no heat removal process took place in the ultrasound energy deposition:

$$\Delta \mathrm{T}_{max} = \frac{\dot{\mathrm{Q}} \cdot \Delta t}{C_v} \tag{21}$$

where $\Delta \mathrm{t}$ is the tissue exposure time under tFUS, and C_v is the heat capacity per unit volume (3.6 J/g/℃ for the brain tissue, 1.606 J/g/℃ for the skull [216]). We estimated the temperature rise at a disk-shape focal area with a radius of one ultrasound wavelength (i.e. 3 mm). With these, the estimation would produce an upper limit for the temperature change.

5.2.9 Statistical Methods

The animal or neuron numbers reflect our past experiences in developing neurotechnologies. Non-parametric statistical tests were conducted in R v3.2.1. The neuronal spiking data normality and variance homogeneity were initially inspected with Shapiro-Wilk test and Fligner-Killeen test, respectively. All related statistical methods have been described within the results.

5.3 Results

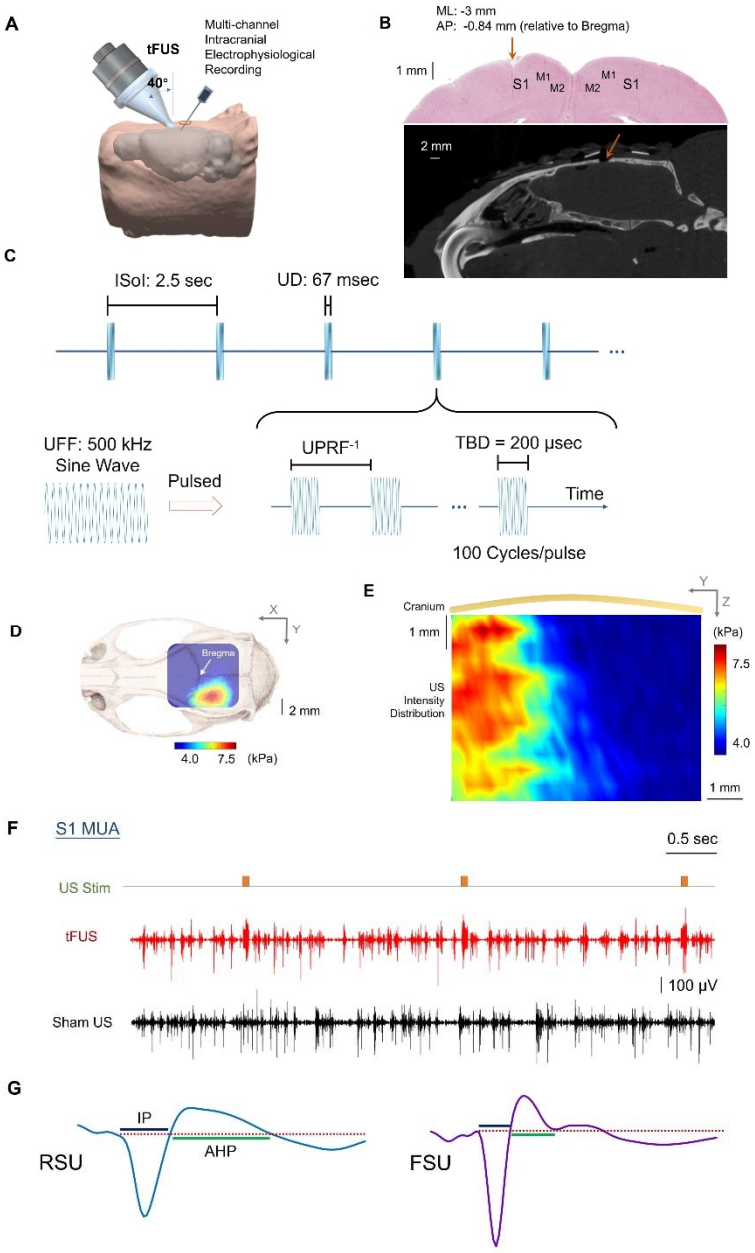

Figure 37. *In vivo* experimental setup and recordings. (**A**) Collimator guiding focused ultrasound (US) to hair-removed scalp of an anesthetized rat model with an incidence angle of 40°, and a 32-channel electrode array inserted at an incidence angle of 40° into the left primary somatosensory cortex (S1) prepared through a craniotomy. The rat head and brain model were 3D reconstructed from T_2-weighted (T2W) MRI images [193]. (**B**) The spatial coordinates of electrophysiological

recordings. The coronal brain slice shows the location of electrode insertion as a physical breakage with the insertion depth of 1 mm at the left S1. A sagittal view of the Micro-CT image captured the surgical burr hole (approximate diameter: 2 mm) on the top of cranium. ML denotes the medial lateral distance from midline; AP denotes the anterior posterior distance from Bregma. (**C**) The temporal profile of tFUS. 100 cycles of sinusoidal wave formed a single ultrasound pulse, which generated a tone-burst at an ultrasound fundamental frequency (UFF) of 500 kHz for a tone burst duration (TBD) of 200 μs. Such ultrasound pulses were repeated at certain ultrasound pulse repetition frequency (UPRF) for a corresponding number within the ultrasound duration (UD) of 67 ms. The inter-sonication interval (ISoI) was 2.5 seconds. (**D** to **E**) One transverse (X-Y plane) and one coronal (Y-Z plane) scans of ultrasound spatial-peak temporal-average intensity (I_{spta}) distribution under the cranium using a hydrophone-based US field mapping system. After transmission through an *ex-vivo* skull, spatial-peak ultrasound pressure is measured at 7.9 kPa, I_{spta} is 15.2 mW/cm^2 at a UPRF of 1,500 Hz, and spatial-peak temporal-peak intensity (I_{sptp}) is 405 mW/cm^2. (**F**) An example of acquired multi-unit activity (MUA) from the S1 using tFUS with UPRF=1500 Hz. The timing between the acoustic-induced action potentials and the administered stimulations are exemplified by 4 trials. The sham condition showed a silence of such MUA. (**G**) Typical examples of regular spiking unit (RSU) and fast spiking unit (FSU) separated from the recorded MUA. The waveform features, i.e. time durations of initial phase (IP) and afterhyperpolarization (AHP) were employed to conduct the units' separation.

5.3.1 tFUS Stimulation and Setup

The *in vivo* experimental setup and the recorded neuronal action potentials are illustrated in Fig. 37. As presented (Fig. 37A), pulsed tFUS is first generated by a single-element transducer, guided to a scalp location over the left somatosensory cortex through a mounted 3-D printed collimator with an incidence angle of 40° [187]. Meanwhile a 32-channel electrode array is inserted using a stereotaxic arm into the targeted brain area (i.e. primary somatosensory cortex S1,

ML: -3 mm, AP: -0.84 mm, depth: 1 mm, Fig. 37b upper panel) prepared through craniotomy, and histologically confirmed through a coronal brain slice. The burr hole through the skull with an approximate diameter of 2 mm is shown in a sagittal CT image (Fig. 37B bottom panel). The stimulation dynamics of the tFUS waveforms consist of tone-burst sinusoidal waves with constant UFF (500 kHz), and TBD (200 μs), and varied UPRF, spanning five levels between 30 – 4,500 Hz (Fig. 37C, Table 2). The duration of inter-sonication interval (ISoI) is 2.5 seconds per trial. The spatial profile of the ultrasound in the x-y plane is superimposed on a rat cranium (Fig. 37D). A hydrophone-based 3-D scanning system was used to obtain measurements of the tFUS spatial temporal profile. The ultrasound spatial map from the coronal view (y-z plane) is reconstructed, in which mechanical energy distributed along a beam up to a depth of 4 mm, but spatial peak energy is located within a depth of 1 mm (Fig. 37E), i.e. the angled incidence[187] leads to a shallowed targeting at cortices. This ultrasound field pattern is resultant from a 40-degree angled incidence, dissipating the majority of ultrasound energy through the skull. Angled tFUS stimulation is the preferred method for studying the cortex, as its activation pattern is shallower than orthogonal tFUS. As a result of the delivery of pulsed low-intensity ultrasound energy, increased firing rate is observed in recorded multi-unit activity (MUA, Fig. 37F). A sham US condition where the ultrasound transducer transmits ultrasound waves in air, directed 180 degrees away from the skull (Fig. 37D), is recorded to control for possible confounds due to acoustic and electromagnetic noise in the experimental setup. Stimulation performed at a secondary control site, during primary site intracranial recordings,

further demonstrated the spatial specificity of the ultrasound-induced brain activities (Figure 38).

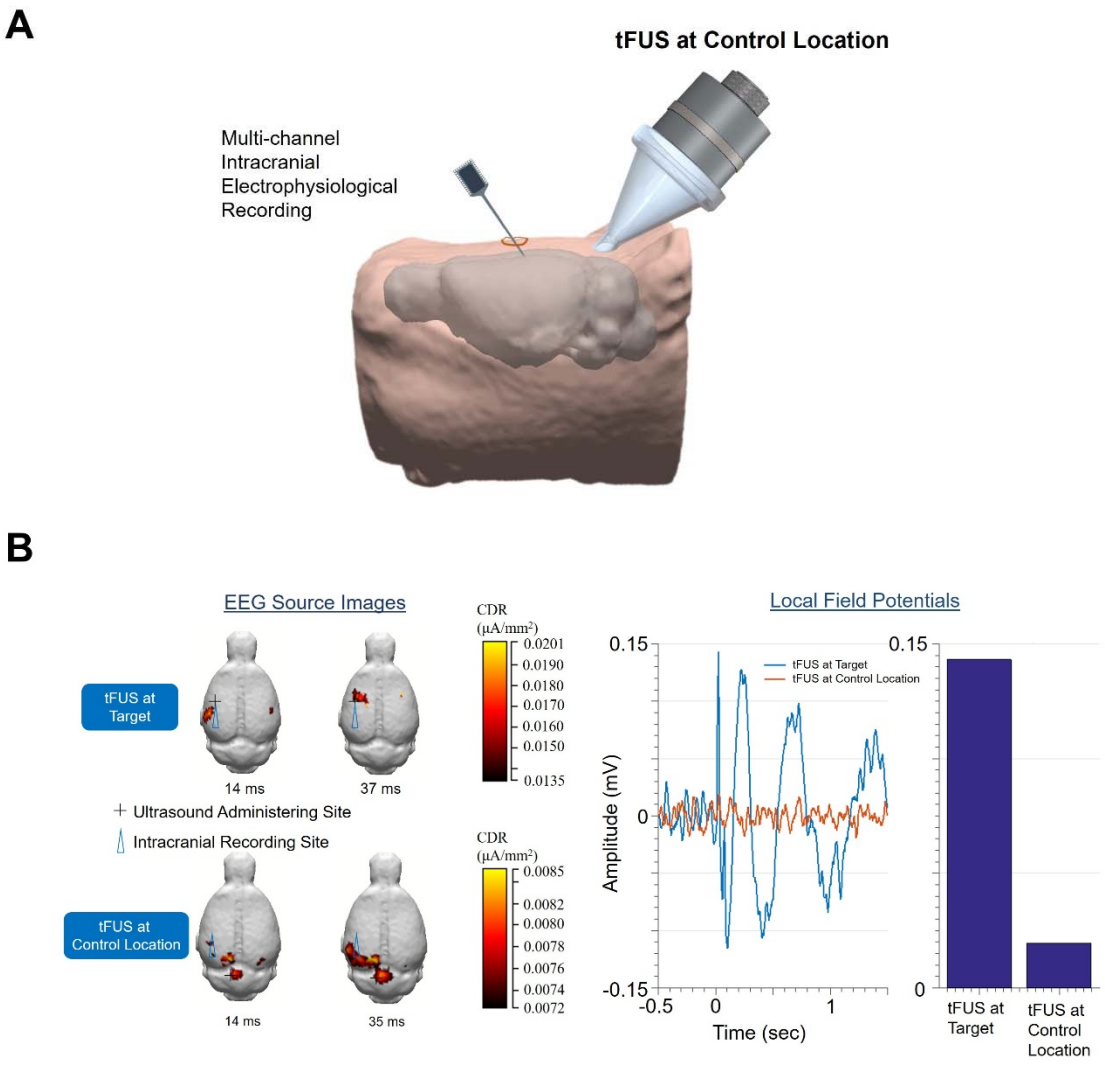

Figure 38. Spatial specificity of tFUS induced brain activations. (A) Another sham ultrasound condition by relocating the incidence of tFUS at a posterior part of brain with ultrasound parameters as UPIx50. (B) Two EEG source imaging frames for tFUS (Figure 37A) and the sham US conditions in (A) obtained from simultaneous 26-channel EEG recording. Local field potentials (LFP) were compared.

5.3.2 Cell-type Specific Response to tFUS in Rats

All recorded action potentials from our 32-channel electrode array were sorted based on the spike waveforms and inter-spike intervals (ISpI). Regular-spiking (presumably excitatory) (RSU) and fast-spiking (presumably inhibitory) units (FSU) are thus identified based on the temporal dynamics of the action potential waveform [217-219]. The features extracted are the durations of initial phase (IP) of the action potential, i.e. from onset to the re-crossing of baseline, and afterhyperpolarization period (AHP), i.e. from the end of the IP to its re-crossing of baseline, demonstrated in Fig. 37G. These features have been associated with differences of ion channel distributions in the neuronal cell membrane. We thus hypothesize that the RSU and FSU will have distinct responses to various tFUS stimulation sequences, which is to be statistically tested given one of the putative mechanisms is that the mechano-sensitive ion channels mediate the acoustic induced neural effects [199].

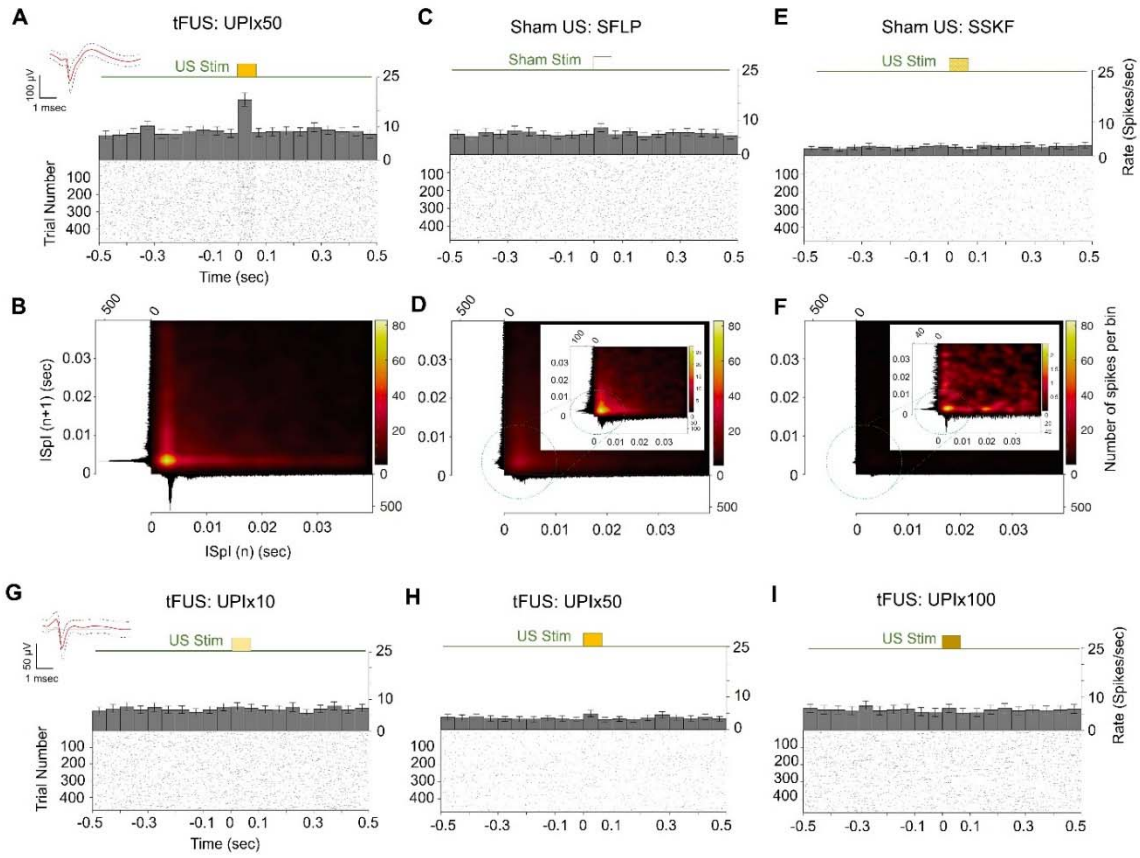

Figure 39. Temporal dynamics of neuronal action potentials responding to administered ultrasound conditions. (**A** to **F**) The peri-stimulus time histograms (PSTH, bin size: 50 ms) and raster plots of the spiking unit (IP duration mean: 850 µs; AHP duration mean: 1850 µs, waveform depicted as an inset in (**A**)) responding to a tFUS condition (illustrated Fig. 1**A**) with UPRF of 1500 Hz (**A**), and sham conditions used as a negative control (**C**) in which the ultrasound aperture was active but flipped away from the animal subject (SFLP, illustrated as Fig. 3**D**) and a positive control (**E**) in which the ultrasound was directed to an anterior part of the skull (SSKF, illustrated as Fig. 3**G**). The histograms and return plots in (**B** to **F**) compared the differences of the first and second-order statistics of inter-spike waiting time using a bin size of 0.1 ms. The color represents the number of spikes within the bin of certain inter-spike intervals. The insets within (**D**) and (**F**) show the return plots in their respective original scales. (**G** to **I**) The PSTHs of another spiking unit (IP duration mean: 700 µs; AHP duration mean: 600 µs, waveform depicted as an inset in (**G**)) recorded

from another rat in response to three tFUS conditions with UPRF of 300 Hz (**G**), 1500 Hz (**H**) and 3000 Hz (**I**). All of the temporal dynamics are computed across 478 trials, with each trial lasting 2.5 s. The applied ultrasound pulsed intensity (UPI) conditions are described in Table 1 (see Methods). Data are shown as the mean±95% confidence interval in the PSTHs.

After recording the MUAs from the first group of wide-type male Wistar rats (N = 6), we studied the neural effects of the administered pulsed tFUS through intracranial recordings. Using the peri-stimulus time histogram (PSTH), we found a significant increase of spiking rate (18.24±2.03 spikes/sec, Fig. 39A) from one of the identified somatosensory cortical neurons (the inset of Fig. 39A, mean spike waveform IP: 0.85 ms, AHP: 1.8 ms) when stimulated with a tFUS condition (1500 Hz UPRF, I_{spta}=15.2 mW/cm^2). More intuitively, an increase of spiking as a function of time along 478 consecutive trials is demonstrated with the raster plot (Fig. 39B), in which the density of spiking events increases during the ultrasound stimulation. A significant bursting peak, a type of non-Poissonian, tFUS-mediated behavior showing in the return plot of ISpI (Fig. 39B). In the sham US conditions, no distinct spiking increase can be found in either the PSTHs, raster and return plots (Fig. 39, C to F). The pattern captured in the return plot of ISpI in the sham condition of SFLP demonstrates a type of exponential distribution of time between subsequent spikes, thus a Poisson distribution of the spike counts, which may indicate a well isolated, long refractory neuron (inset of Fig. 39D). When being further treated with the other sham condition of SSKF to potentially introduce another control for skull-conduction, it can be seen from the PSTH (Fig. 39E) that the overall spiking rate of such identified single unit (inset of Fig. 39A) decreases comparing to Fig. 39A,

and the more dispersive pattern presented in the return plot at its original scale (inset of Fig. 39F) implies a more sporadic firing by this neuronal unit.

In contrast, another identified cortical neuron (inset of Fig. 39G) with shorter durations of IP (mean: 0.7 ms) and AHP (mean: 0.65 ms) shows a more homogeneous PSTH distributions in response to three levels of tFUS treatments (Fig. 39, G to I) using the ultrasound setup shown in Fig. 37A. However, the firing rate (7.6±1.2 spikes/sec) is not altered significantly by the US stimulation (300 Hz UPRF, I_{spta}=3.0 mW/cm^2) comparing to pre-stimulus rates (e.g. 7.5±1.2 spikes/sec at the bin of [-0.05, 0] s). Interestingly, for this neuron, we still found no significant changes in spiking rates (6.5±1.3 spikes/sec) even when ultrasound was administered at a UPRF 10 times higher (3000 Hz UPRF, I_{spta} = 30.4 mW/cm^2, Fig. 39I). From Fig. 39H, we can further observe that this fast-spiking unit (5.0±1.0 spikes/sec) does not prefer the 1500 Hz UPRF (I_{spta} = 15.2 mW/cm^2, Fig. 39H) when comparing to the unit in Fig. 39A. Overall, the baseline spiking rate variability of this fast-spiking unit may not be negligible across the three tFUS conditions, which might be due to the applying order of tFUS conditions, as in this case, the UPIx10 was applied prior to UPIx100 that was followed by the UPIx50. The time-accumulating effect of tFUS might be playing a role herein.

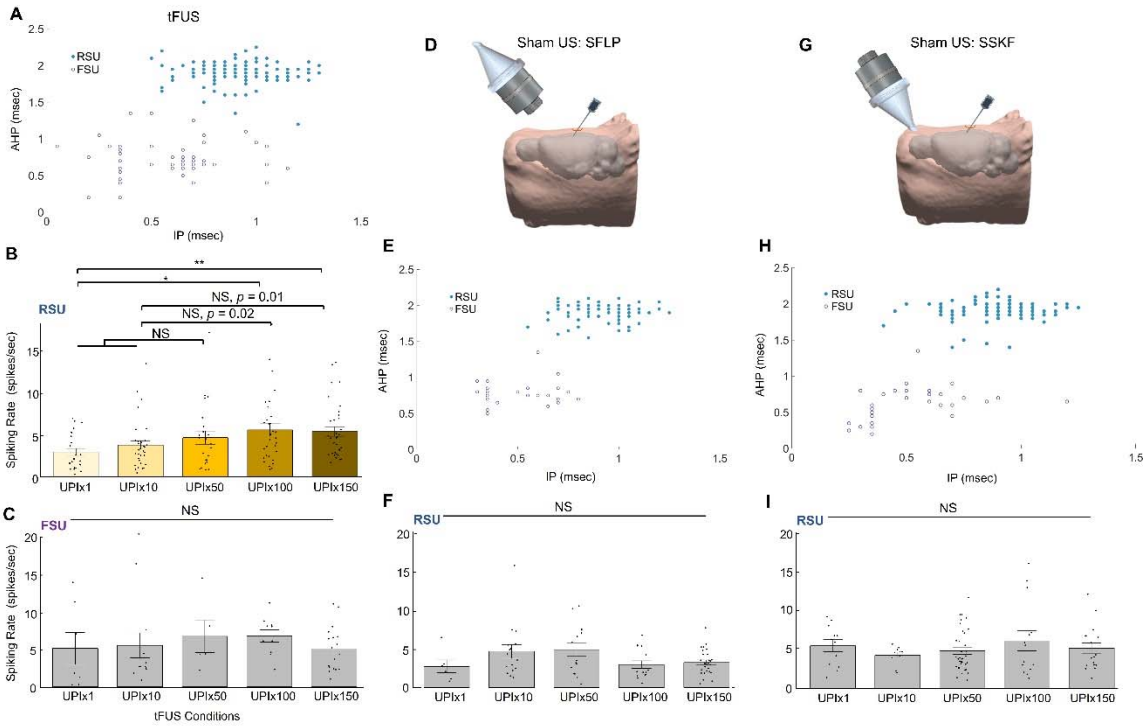

Figure 40. Cell-type selective responses to tFUS and sham US conditions. (**A**) k-means cluster analysis of 199 single units identified from 6 rats with blue solid circles depicting the RSUs while purple circles representing the FSUs. The majority is classified as the RSU with longer IP and/or AHP durations than the FSU. These spiking units are recorded and identified under the influence of the administered anesthesia (xylazine) and analgesic drugs (ketamine), in which the durations of both IP and AHP are observed to be longer than the results reported in literature [217, 220] for different sedative approaches. (**B**) The 146 RSUs significantly differ their responses to different tFUS conditions. Data are shown as the mean±s.e.m., with statistical comparisons made through Kruskal-Wallis one-way ANOVA and one-tail two-sample Wilcoxon tests with Bonferroni correction for multiple comparisons. (**C**) The FSU group, which consisted of fewer neurons (N = 53, marked as purple hollow circles), was observed to have a higher mean spiking rate than RSUs, whereas this FSU group showed no significant effect by different UPRF levels. Data are shown as the mean±s.e.m., statistics by Kruskal-Wallis one-way ANOVA. (**D**) The experimental setup of the sham US condition as a negative control (SFLP). The ultrasound transducer was flipped its aperture by 180°, although the pulsed ultrasound and the intracranial recordings were maintained. (**E**) The

cluster analysis for another 108 single units identified from the sham US condition. 80 RSUs and 28 FSUs were separated. (**F**) RSUs showed a homogeneous lack of response to sham ultrasound conditions. No significant effect by the ultrasound conditions was observed through statistics by Kruskal-Wallis one-way ANOVA. Data are shown as the mean±s.e.m. (**G**) The experimental setup of the sham US condition as a control for bone-conduction (SSKF). The ultrasound incidence took place at an anterior location of the skull, and the aperture was kept transmitting ultrasound. (H) The third cluster analysis for another 127 single units identified from the sham condition of SSKF. 89 RSUs and 38 FSUs were separated. (I) RSUs also showed a homogeneous lack of response to the SSKF sham ultrasound conditions. No significant effect by the ultrasound conditions was observed through statistics by Kruskal-Wallis one-way ANOVA. *$p < 0.005$, **$p < 0.001$. NS, not significant. s.e.m., standard error of mean.

Given these case studies, we pursued a statistical investigation of the behavior of different neuron types in response to tFUS and sham conditions, across multiple levels of UPRFs. In the tFUS group, we compiled all single unit activities during the UD of 67 ms recorded from the rats, and separated them into RSUs and FSUs using k-means cluster analysis (Fig. 40A). 199 identified single units were separated into the two groups, with the RSU group containing 146 units. The sample sizes are unbalanced due to the prevalence of each cell types in the cortex. In the RSU group, we found a statistically significant effect by the UPRF levels (Kruskal-Wallis chi-squared =14.45, p = 0.006), which indicated that the RSUs change their spiking rates accordingly in response to the tFUS conditions (Fig. 40B). More specifically, the spiking rates have shown an increasing trend along with the elevating UPRFs.

Furthermore, we found 2 significantly different pairs among 10 two-sample post-hoc tests (Fig. 40B, thresholding at $p < 0.005$ Bonferroni corrected for multiple

comparisons), in which our null hypothesis was that the RSUs' spiking rate in the low UPRF ultrasound condition would be no less than the one in the high UPRF. As a result, the spiking rates in UPIx50 was not significantly higher than those in the other two low UPRF conditions ($p > 0.1$). In the FSU group (Fig. 40C), no significant difference between tFUS conditions could be found (Kruskal-Wallis chi-squared = 4.34, $p > 0.3$). This implies that the spiking rates of the FSUs were not significantly altered by the levels of UPRF, consistent with our case study (Fig. 39, G to I). The contrast between the responses observed in these two different neuron types suggested a cell-type selective mechanism by tFUS. Unsurprisingly, the RSU group did not show significant differences among the five levels of sham US conditions, including the SFLP sham (Kruskal-Wallis chi-squared = 5.94, $p > 0.2$, Fig. 40F) and the SSKF sham (Kruskal-Wallis chi-squared = 0.96, $p > 0.9$, Fig. 40I). Through these results, we demonstrate that in an anesthetized rat model, the RSUs significantly increase their firing rate in response to UPRF as high as 4500 Hz, although the median value of the rate at 1500 Hz and 3000 Hz UPRFs became higher than the value in its corresponding sham condition (UPIx1500 tFUS vs. SFLP sham: 4.11±0.77 vs. 3.62±0.84; UPIx3000 tFUS vs. SFLP sham: 4.53±0.72 vs. 2.09±0.50). In spite of the none dependency on the UPRFs, we notice that the UPIx1 SSKF sham, however, demonstrates a high spiking rate (UPIx1 tFUS vs. SSKF sham: 2.06±0.41 vs. 6.21±0.78), this is possibly due to the more effective sensory input induced by the low UPRF (30 Hz) ultrasound targeting at the anterior scalp close to the sensory hairs.

The distinct difference in responses of RSUs and FSUs to the change of ultrasound UPRF has not been reported in literature. Although it is not surprising to see that the FSU spikes faster than the RSU does, since the length of the refractory period determines the minimum time between neuronal firings. The spiking rate contrast between these two groups can be observed in Fig. 40, B and C. When administered with a low UPRF (such as 30 and 300 Hz), the RSUs do not respond to tFUS stimulation, while FSUs maintain a stable spiking state during the sonication. The observed responses suggest cortical neurons with different action potential shapes, hence different distribution of ion channels in terms of ion channel types or relative quantity, have a distinct response patterns to tFUS UPRF. While FSUs are excited across all UPRF frequencies, RSUs only exhibit increased firing rate during high UPRFs. This could explain why when stimulating at low UPRFs, some previously reported studies have observed tFUS suppression effects [97, 138]. The observed effects may not simply be due to the lack of facilitation in the neural circuit, but inhibition in the network could play a significant role.

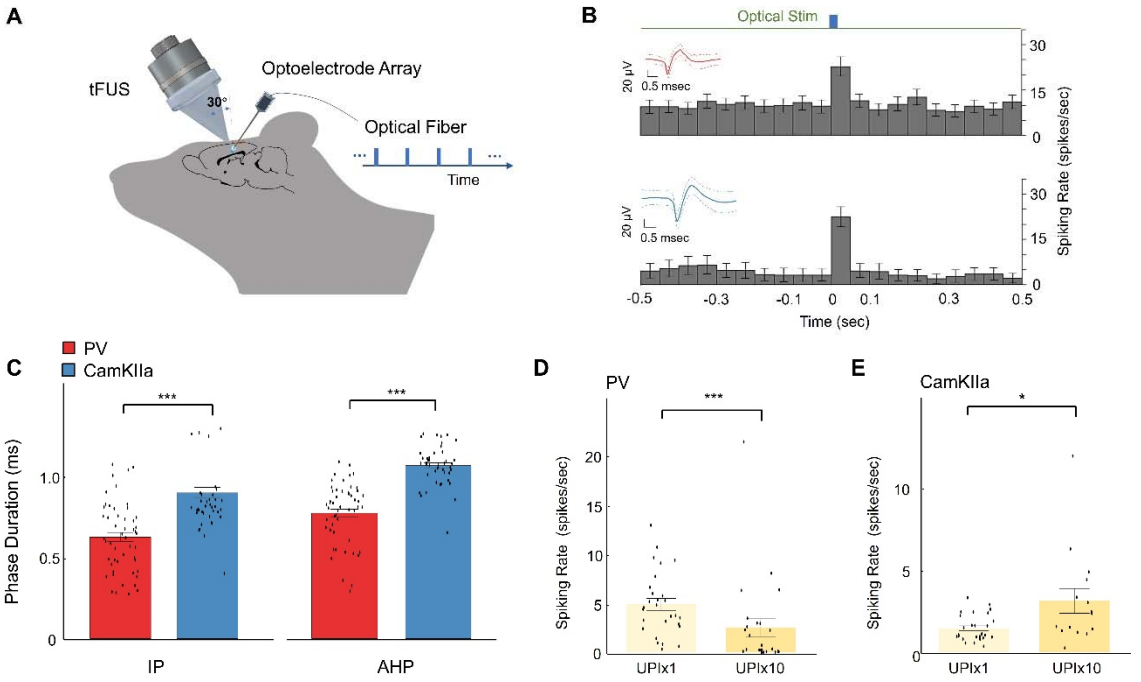

Figure 41. Validation of UPRF preferences by inhibitory and excitatory neurons. (**A**) A mouse-specific 3D printed collimator guiding tFUS to hair-removed scalp of an anesthetized (2% isoflurane, 2 mg/kg bupivacaine subcutaneously) transgenic mouse model with an incidence angle of 30°, and a 32-channel optoelectrode array inserted at another incidence angle of 40° into the left S1 prepared through a craniotomy. The blue light stimuli were pulsed using a PlexBright LD-1 Single Channel LED driver at 30 mA, and were then delivered via optical fiber (105 μm diameter) to the recoding side of the shank. (**B**) The PSTHs (bin size: 50 ms) of the PV spiking unit (IP duration mean: 550 μs; AHP duration mean: 850 μs) and the CAMKIIa spiking unit (IP duration mean: 600 μs; AHP duration mean: 1100 μs) responding to the optical stimuli. Spike waveforms depicted as insets in (b), solid red line as the mean waveform, dashed lines as the waveform standard deviation. Data are shown in the PSTHs as the mean ± 95% confidence interval. (**C**) Comparing PV and CamKIIa neurons regarding the IP and AHP phase durations. Data are shown as the mean±s.e.m., statistics by two-tail Wilcoxon test. (**D** to **E**) The spiking rates comparison between treatment conditions of UPIx1 and UPIx10 within PV and CAM neurons respectively. Data

are shown as the mean±s.e.m., statistics by two-tail Wilcoxon test. *$p < 0.05$, **$p < 0.01$, ***$p < 0.001$.

5.3.3 Optogenetics Confirms Cell Type Specific Response in Mice

To access our cell-type specificity hypothesis, we tested our results in transgenic mouse model with PV (N = 52, from 3 mice) and CamKIIa (N = 42, from 2 mice) cortical neurons confirmed by responding to optical stimulations. Fig. 41A illustrates the *in vivo* experimental setup combining the optical stimulation, tFUS and multi-channel intracranial electrophysiological recordings. The optogenetic stimulation (wavelength = 465 nm) locally activates a subpopulation of channelrhodpsin expressing neurons, based on the MUA recording from our optoelectrode we can thus identify the cell type of our recording neurons (Fig. 41B). The waveforms of action potentials of each neuron are illustrated together with the spiking rates when receiving the optical stimuli (Fig. 41B). Since the activation of channelrhodopsin has been linked to changes in neuronal baseline spiking dynamics, all optogenetic stimulations are administrated after completing all tFUS recording sessions.

In changing animal models from rats to mice, we changed the outlet size of our collimator for the small mouse brain (see Methods for a different outlet size) but we maintained the same tFUS transmission parameters. We were not able to replicate the higher tFUS UPRFs at the same intensities since the mouse skull provides much lower attenuation than the rat skull whereas our stimulation parameters are designed for stimulations on rats. At high UPRFs we observed significant noise in our recordings. Between PV and CamKIIa neurons, we

observed significant differences in the action potential waveforms regarding the IP and AHP phase durations, validating our method for separating neuron population in rats (Fig. 41C, $p < 0.001$). In PV neurons, spike rates are higher under tFUS stimulation at UPRF of 30 Hz (Fig. 41D, $p < 0.001$), while in CamkIIa neurons, significantly higher spike rates are observed during tFUS stimulation at UPRF of 300 Hz (Fig. 41E, $p < 0.05$). The difference in response to tFUS UPRFs across these two neuron types shows further evidence of cell-type specific effects of tFUS.

Caution should be taken when directly comparing the mice and rats subject groups due to the difference in animal models and anesthesia methods. These results indicate that different animal models may have significantly different responses to ultrasound UPRFs. For example, the differences of both excitatory (CamKIIa) and inhibitory (PV) neurons in response to the 30 and 300 Hz UPRFs are significantly contrasted (Fig. 41, D and E) comparing to the observations from non-transgenic rats (Fig. 31, B and C). However, the cell-type specific response profile to different ultrasound UPRFs are conserved across the two animal models studied.

5.4 Discussion

In the present study, we set out to use multichannel intracranial recordings to test our hypotheses of tFUS's ability to induce cell-type specific stimulation. Based on the results reported above, we have gained more understanding of the tFUS parameter space, and can furthermore infer on the mechanism of action of tFUS stimulation. Besides macroscopic perspectives reported in literature, uncovering the underlying mechanism requires a detailed inspection of how

neurons respond to a vast set of acoustic parameters. Recordings using multi-channel intracranial electrophysiology allows us to examine the neuron cellular dynamics with high spatial and temporal specificity.

5.4.1 An Intrinsic Selectivity between Excitatory or Inhibitory Neurons by tFUS UPRF

The results reported above are *in vivo* evidences that subsets of neurons, grouped by their action potential waveforms, respond differently to tFUS stimulation UPRFs. This provides insight into results previously reported by other groups studying tFUS [97, 113, 129, 187]. Our results suggest that tFUS interacts with neurons based on ion channel dynamics. Hence, the intrinsic differences in ion channel dynamics between different neuron types contribute to differences in the neuron's response to tFUS.

The ultimate goal of studying the mechanisms of tFUS is to translate the technology to clinical utility. Previous studies have shown that inhibitory effect of tFUS was found at the primary somatosensory cortex [97] and thalamus [138] in humans, in which the same ultrasound parameters were employed (single-element transducer with UFF = 500 kHz, UPRF= 1 kHz, UD = 500 ms, UDC = 36%). In contrast, other studies on humans have shown excitatory effects that the primary visual cortex was directly excited with a specific ultrasound administration (UFF = 270 kHz, UPRF = 0.5 kHz, UD = 300 ms, UDC = 50%) [113], and simultaneous stimulating capability of tFUS were also shown at primary and secondary somatosensory cortices (UFF = 210 kHz, UD = 500 ms) [142].

Given these parameter-dependent studies, the effects of tFUS achieved by these two groups are sometimes observed to be inconsistent or even contradictory on healthy, awake subjects. We cannot conclude from these studies whether the observed behavior was due to overall activation or suppression of neural activity due to changes in tFUS parameters, or if the ultimate behavior was due to selective modulation of the neural network. The modified NICE model was proposed to unify the ultrasound parametric space and predict either excitatory or inhibitory effects at a neuronal level [203]. As we set out to explore the tFUS parameter space in the *in vivo* brains, we set our administered duty cycle of tFUS to the five levels (see Table 2) while maintaining the I_{sptp} as a constant. When tuning tFUS parameters, we discovered that neuronal units grouped based on spike shape characteristics display different spike rate during the same tFUS stimulation. The excitatory neurons (RSUs) exhibit higher spiking rates when stimulated with high UPRF, thus high duty cycle, whereas the inhibitory neurons (FSUs) exhibit high spiking rate during stimulation at all UPRFs studied. The inhibitory phenomena found by Legon *et al*. [97, 138] resulted from a UDC located in a transition zone between tFUS induction of inhibitory and excitatory effects [203], whereas the brain activation reported by Lee *et al*. [113, 142] is probably due to the applied higher UDC. In other words, the UDC of 50% has already significantly increased the activity of excitatory neurons, and since the spiking activity of the inhibitory neurons does not increase proportionally, resulting in facilitation of behavioral outcomes.

5.4.2 UPRF: Possible Mechanism of Cell-type Specific Effects

In a recent study, acoustic radiation force (ARF) has been inferred as the most probable energy form that induces UPRF-dependent behavioral responses [133]. In the present study, when different UPRFs are used to stimulate cortical neurons, we observed a significant difference in response between two neuron subpopulations. We also believe that the difference in response between different neuron types is observed due to the interactions between transcranial ARF and ion channels in the neuron membrane. Neurons exhibit different action potential waveforms due to the difference in distribution of membrane proteins both in channel types and relative quantity of each type of ion channel. These distinct types of membrane proteins may have different response dynamics to acoustic radiation force [199, 221]. The basis of our hypothesis was demonstrated between the FSUs and RSUs in rat S1 cortex.

We further tested this hypothesis in the S1 cortex of transgenic mice. Optogenetics is used to identify excitatory neuron and inhibitory neuron populations, by coexpressing channelrhodopsin only in CamKIIa and PV expressing neurons. Although we cannot verify whether FSUs and RSUs correspond directly to PV neurons and CamKIIa neurons in this study, this model allows us to study specific protein expression to neuronal responses to tFUS stimulation.

In this model, we also observed a distinct spiking response to tFUS stimulation UPRFs. Thus, in two different *in vivo* models, and two different methods to identify cell types, we have observed distinct responses to tFUS stimulation

UPRFs. Based on our findings, future investigations can use genetic approaches to attribute the observed cell-type specific response to differences in protein expressions in different neuronal types.

5.4.3 Ultrasound Safety

All ultrasound parameters employed for targeting at the cortical region used on the S1 cortex of rats are maintained with I_{spta} below 50 mW/cm^2, which lead to negligible temperature rises (< 0.001 ℃) at the targeted brain area. In addition, the mechanical index (MI) used in these experiments is less than 0.1, given the low peak negative pressure (i.e. < 100 kPa). Such low MI makes cavitation in brain tissue unlikely. These levels are well within the levels advised by the Food and Drug Administration (FDA) standard for ultrasound diagnostic imaging safety [189, 222]. Hematoxylin and eosin stains gathered immediately after stimulation in both S1 and the hippocampus show no evidence of neuronal damage, local hemorrhage or inflammatory response at the stimulation site.

5.4.4 Controls for Confounding Effects

Based on a simultaneous EEG source imaging technique applied on rats reported previously [83], observations of the auditory cortex can be induced as a secondary activation when tFUS is not directed at the auditory cortex (see Figure S3a). Therefore, in order to examine the auditory side effects of our tFUS setup, presumably due to tFUS induced mechanical vibrations transmitted through the skull, we conducted tFUS stimulation in rats after chemical deafening (Fig. 42). Our observations of a local rise in local field potential (LFP) at the S1 cortical region in both control subjects and subjects with significant reduction in hearing (see Fig.

42d-e), suggest that side-effect activations in the auditory cortex from tFUS induced hearing percepts do not dictate activation of S1 cortex. Surprising, in this deafened model, the tFUS-induced LFP resembles the reported LFP waveform by Tufail, *et al*. [112]. Similar ultrasound parameters (e.g. UFF and UPRF) were employed in both studies. Although the chemicals used in this group of experiments have been shown to damage auditory pathways, we do not have confirmation of whether these drugs present toxicity to other parts of the neural network. Therefore, one should be cautious in critically evaluating recordings gathered from these deafened rats.

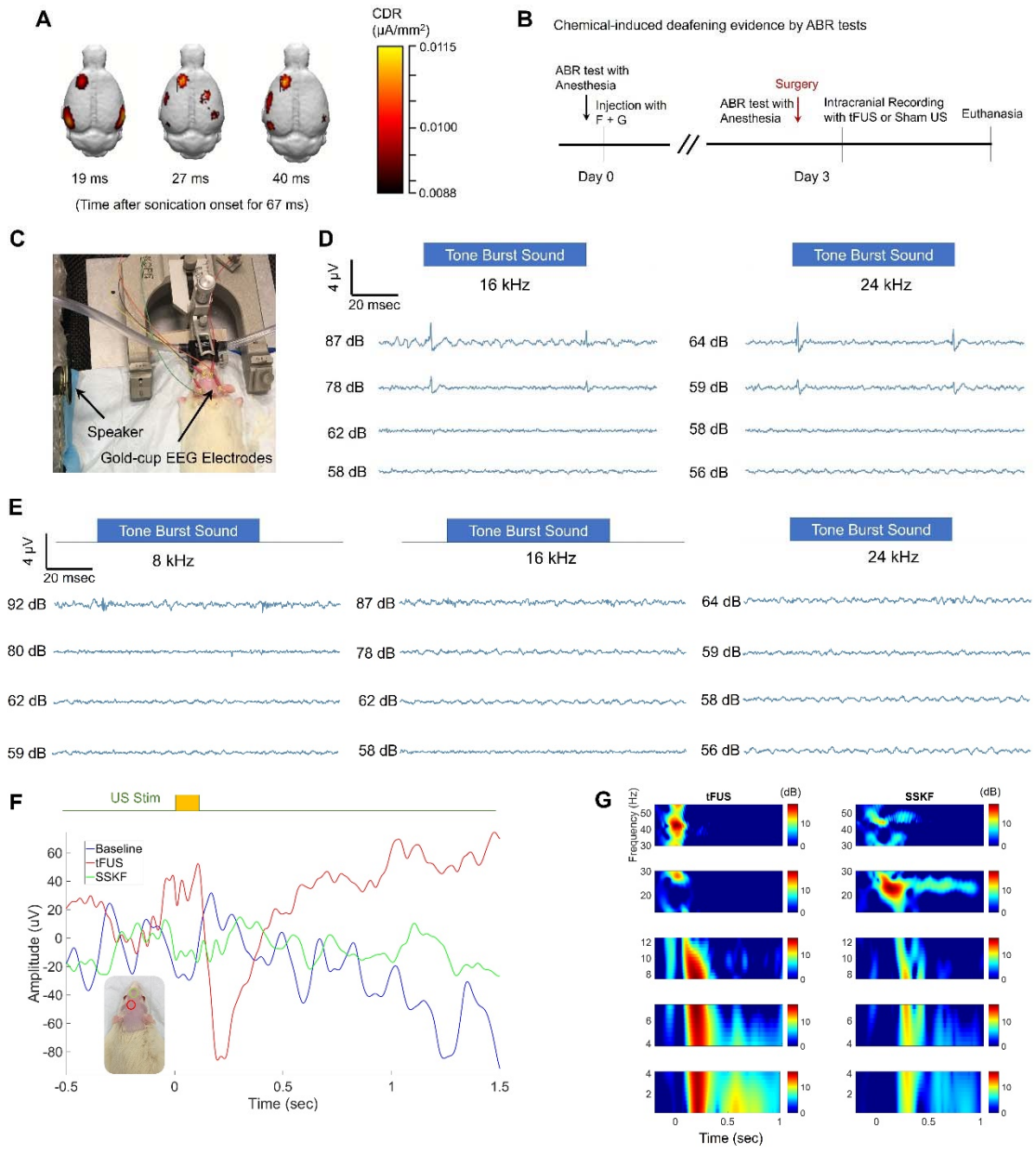

Figure 42. tFUS induced local brain activity on a chemical-induced deafened rat. (A) On a healthy wild-type rat, using EEG-based source imaging technique for tFUS, the administered ultrasound (UPIx50) activated a targeted brain area with a 40-degree ultrasound incidence angle. Besides, we can also notice the bilateral activation at auditory cortical regions. We initially reported this finding at the 3rd Annual BRAIN Initiative® Investigators Meeting. (B) The experimental protocol for creating chemical-induced deafening model. The deafening will be tested by pre- and post-

chemical injection ABR tests on Day 0 and Day 3, respectively. A combination of injected chemicals includes furosemide and gentamicin. (C) The ABR test using speaker as sound stimulation source. Gold-cup electrodes are used to measure the brainstem response induced by the tone-burst sound. The rat subject is anesthetized using 2% isoflurane through inhalation. (D) ABR test results before chemical injection. Four levels of sound intensity with 16 and 24 kHz center frequencies were used. (E) On Day 3, post-injection ABR test results show significantly reduced auditory brainstem responses at three center frequencies (8, 16, 24 kHz) with each applying four levels of sound intensities. (F) LFP recorded at the S1 area and averaged across 478 trials. The employed ultrasound condition is UPIx50. Comparing with a sham condition (SSKF: relocate ultrasound incidence to a site anterior to the S1 as shown in the inset). The green circle in the inset shows the sham ultrasound incidence location, while the red circle indicates the location targeted in the tFUS condition. In this deafened rat model, the tFUS-induced LFP still resembles the reported waveform by Tufail, *et al*. [112]. Similar ultrasound parameters (e.g. UFF and UPRF) were employed in their work. (G) The time-frequency representations at multiple frequency bands illustrate the differences between tFUS and SSKF conditions.

Since our stimulation location is at the primary somatosensory cortex, control studies were conducted to examine whether activations recorded in the S1 could be due to somatosensation rather than direct activation of neurons in the S1. In a study examining the effect of tFUS on anesthesia recovery time, naïve male rats around 12 weeks (body weight: median 386 g, range 370 – 400 g) were injected only with an initial dose of ketamine and xylazine cocktail (75, 10 mg/kg respectively) adjusted according to the animal weight. After sedation, rats are skin prepared and kept on heat pads to allow for recovery from anesthesia. Temperature, heart rate and video recording of movements are monitored. Recovery time is defined based on injection time and time of first perceived

movement. Rats are divided in 3 subgroups. Group 1 (N = 6, Fig. 43A) received tFUS stimulation (UPIx50) at S1HL, peripheral stimulation electrodes are set at the contralateral hindlimb with no current injection. Group 2 (N = 3, Fig. 43C) received sham ultrasound directed 180 degrees away from the skull (Fig. 40D), only a collimator filled with ultrasound gel above S1HL, and peripheral stimulation electrodes are set at the contralateral hindlimb and monopolar pulse of peripheral stimulation at the contralateral hindlimb, current thresholds set at minimum current (1-3 mA dependent on subject, 0.08 – 0.1 ms set by PowerLab 26T) to induce a visible muscle contraction. Group 3 (N = 3, Fig. 43B) received tFUS directed at the anterior part of the skull away from cortical regions of the brain (shown as the inset of Fig. 42F), and peripheral stimulation electrodes were set at the contralateral hindlimb with no current injection. We combined the Groups 2 and 3 as a Sham US group, and compared this new group to the Group 1. As a result, rats with tFUS stimulation directly at S1 (UPRF = 1500 Hz) recovered from anesthesia significantly faster than rats during Sham US. Controls were tested for rats for auditory percepts coupled and not coupled to the skull, and rats with peripheral stimulation at the contralateral hind limb to control for somatosensation. Control rats with auditory percepts coupled to the skull has tFUS focused on the skull, far away from S1, control rats with auditory percepts not coupled to the skull have ultrasound directed 180 degrees away from S1. This study suggests that our tFUS experimental setup can elicit direct stimulation of the rat brain without confounding effects of auditory percepts and somatosensation.

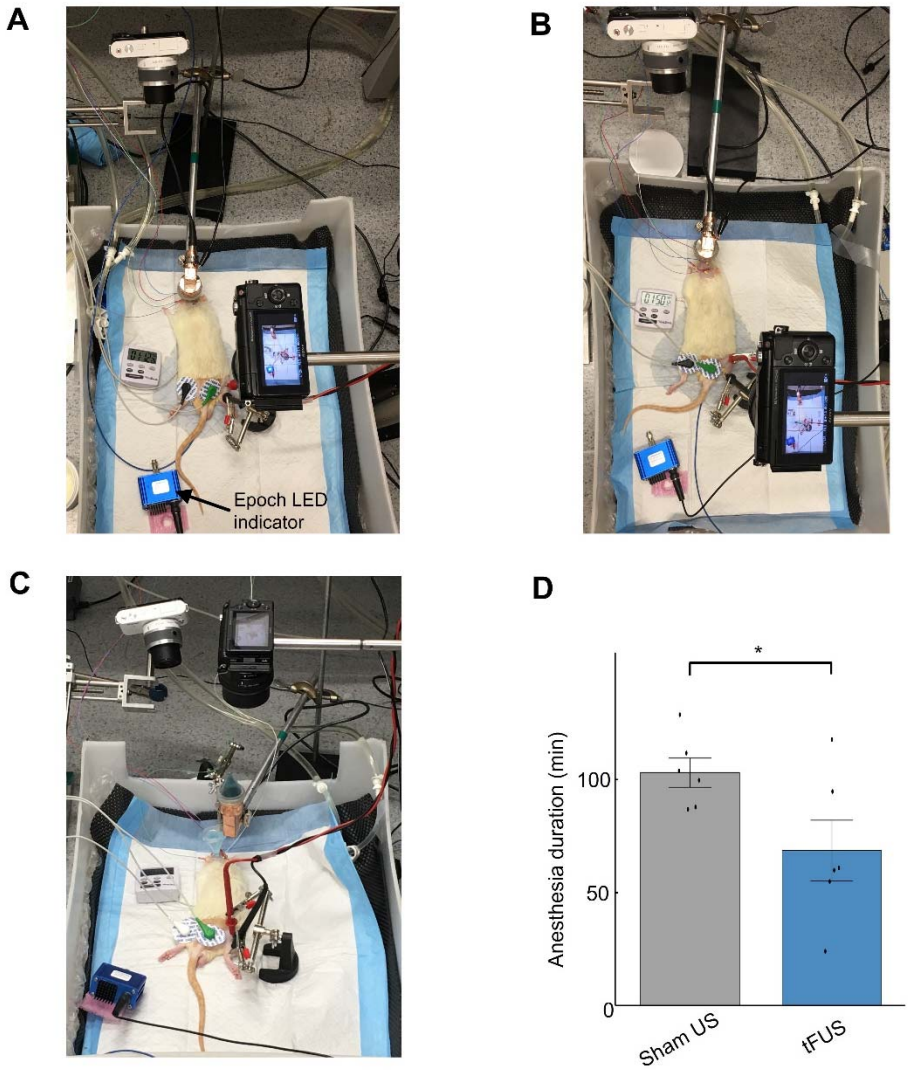

Figure 43. tFUS treatment leads to reduced anesthesia duration. (A to C) Experimental setups for administering tFUS (A), SSKF (B), and peripheral electrical stimulation (C). Two cameras do the videotaping after the anesthesia injection until an animal subject restores its moving capability. (D) One-tail Wilcoxon test for a comparison between Sham US (i.e. SSKF and electrical stimulation at contralateral hindlimb only) and tFUS. Data are shown as mean ± s.e.m. *$p < 0.05$.

5.4.5 Study Limitation

In this work, the rodent models were sedated by anesthetic agents, which may introduce an inevitable confounding factor of changing the neuronal spiking activities. In particular, the injection of ketamine/xylazine does not provide a constant anesthesia level. However, we have tried to randomize the order of applied tFUS and Sham US conditions, which helps reduce the influence of anesthetic level to the statistical analyses. Based on literature reported first-order drug elimination kinetics, we established a numerical model to estimate the ketamine/xylazine blood concentration. When the anesthetic agents and ultrasound conditions were considered as factors, and the spiking rates during the sonication were considered as responses, a simple ANOVA test indicates no significant effect in comparisons among ultrasound conditions by using the anesthetic agents (data not shown).

Caution should be taken when comparing between mice and rat models under tFUS stimulation. Our major constraint was due to the lack of widely available, well studied transgenic rat models for optogenetic stimulation. The thickness of the mice skull over the S1 cortex is 5 to 10 times thinner than that of rats. This leads to different distortions in tFUS field which may result in differences during stimulation. For mice subjects, a different collimator with a smaller tip size was used (see 5.2.2) to account for a smaller S1 region in order to avoid stimulating a widespread area in the mouse cortex. Discrepancies in activation area may also contribute to confounding results. Furthermore, rats were anesthetized with

ketamine and xylazine cocktails while mice were anesthetized with isoflurane due to differences in experimental setup. Such a difference in anesthesia methods could also contribute to differences in results.

Regarding the effective harnessing of ultrasound energy, besides restricting the size of collimator outlet to be commensurate with the ultrasound wavelength, we are also cautious about the potential effect of using the 2-mm burr hole (Fig. 37B) via which the electrode array is able to reach the neurons. For this reason, we have introduced the 3D ultrasound field mappings (Fig. 37, D and E) to explore potential alterations because of the low-acoustic-impedance conduit. And due to the requirement of 3D scanning of ultrasound field, we were only able to place the needle hydrophone (50 mm length) behind a freshly excised skull top piece in water, rather than inside a hollow rodent skull and conducted the ultrasound pressure mapping. However, the latter one is believed to be more demanded so as to obtain additional knowledge of how significant of standing waves would be inside the rodent skull cavity by using the 500 kHz UFF, given that considerable interference patterns due to standing waves has been reported by administering 320 kHz tFUS to rats [223].

Furthermore, the angles of the ultrasound incidence are designed to physically accommodate the ultrasound apparatus and the recording probe, in which we tried to preserve the ultrasound wave in the longitudinal mode versus the shear mode. Although it is unavoidable in the practice, the angled tFUS may introduce nontrivial shear wave propagating along the skull, and thus lead to increased skull conduction. Nevertheless, the difference in the ultrasound wave

mode might result in differed neuronal responses, which also requires further investigations.

Chapter 6. Summary and Outlooks

6.1 Summary

6.1.1 High-frequency Magnetoacoustic Tomography with Magnetic Induction (hfMAT-MI) [146]

We have developed a hfMAT-MI imaging system which provides electrical-conductivity imaging with a 1-mm spatial resolution, a significant improvement over conventional MAT-MI methods. We have also conducted pilot studies on *in vivo* tumor-bearing mouse models. Our results demonstrate the capability of hfMAT-MI for better discriminating transplanted human cancer tissue from normal surrounding tissues with internal details. To the best of our knowledge, this is the first *in-vivo* study using hfMAT-MI to track the tumor growth and establishes the feasibility of applying this magneto-acoustic imaging for early breast cancer detection.

6.1.2 Contrast-enhanced Magnetoacoustic Imaging with Magnetic Nanoparticles [47]

We demonstrated the capability of the MAT method to detect and reconstruct the distribution of superparamagnetic iron oxide nanoparticles embedded *in-vivo* within live, nude mice containing induced LNCap prostate tumors. As this is an ultrasound based imaging method using a short pulsed magnetic field, the present method has good resolution and imaging depth for potential applications in imaging tumors within soft tissue.

6.1.3 Non-Invasive Brain Imaging Perturbed by Low-intensity tFUS [83]

In this study, we have demonstrated, in an *in vivo* experiment in three rat subjects, that low-intensity tFUS (e.g., $I_{spta} < 1$ mW/cm^2) can induce brain electrical activity in the target region of tFUS. We have noninvasively recorded multichannel scalp EEG following low-intensity tFUS and have localized and imaged tFUS-induced brain activation from scalp recorded EEG distributions. Our promising results demonstrate the feasibility of noninvasive sensing low-intensity tFUS-induced brain activation and localization and imaging of brain activity from noninvasive scalp EEG signals. This study suggests that the proposed perturbation-based neuroimaging using tFUS-ESI merits further investigation and may become a useful tool for delineating normal and pathological brain networks and circuitry in a well-controlled and noninvasive manner. The ESI-guided tFUS may also have important applications to the treatment and management of various brain disorders.

6.1.4 Towards the Mechanism of Ultrasound Neuromodulation with Intracranial Electrophysiological Recordings

Transcranial focused ultrasound (tFUS) is a promising neuromodulation technique, but its mechanisms remain unclear. We investigate the effect of tFUS stimulation on different cell types and synaptic connectivity in *in vivo* anesthetized rodent brains. Single units were separated into regular-spiking and fast-spiking units based on their extracellular spike shapes, further validated in transgenic optogenetic mice models of light-excitable excitatory and inhibitory neurons. We

show that excitatory neurons are significantly less responsive to low ultrasound pulse repetition frequencies (UPRFs), whereas the spiking rates of inhibitory neurons do not change significantly across all UPRF levels. Our results suggest we can preferentially target specific neuron types noninvasively by altering the tFUS UPRF.

6.2 Outlooks

6.2.1 Combining the Diagnostics and Therapy Using the Nanoparticle-mediated Magnetoacoustics.

Mapping the biological tissues' electrical conductivity, the (hf)MAT-MI has been developed to pursue a potential clinical use in cancer diagnosis with an ultrasound spatial resolution. The contrast-enhanced MAT using MNPs further shows the capabilities of non-invasively estimating the bio-distribution of MNPs, especially the tumor-targeting nanoparticles. Along with the rapid developing bio-material science, we can anticipate more effective tumor-targeting MNPs with improve retention rates. Thanks to the wide MNP imaging dynamic range of the MAT, a theranostic use by combing the targeted therapy with diagnosis may further lead more beneficial applications. Fig. 44 summarizes imaging modalities and applications for MNPs.

Magnetic resonance imaging was firstly used to image magnetic nanoparticle-labeled molecular targets, as it is able to provide an enhanced image contrast because of its nature that can significantly shorten relaxation time [224]. Research is ongoing to reliably detect such signal changes at concentration levels

in the 1- 10 mg Fe/mL range. With the sweep imaging with Fourier transformation (SWIFT) MRI technique, quantitative imaging of up to 3 mg Fe/mL concentration of MNPs is possible.

X-ray CT scanning has also been explored as another approach for estimating the distribution of magnetic nanoparticles [225]. It is seen that the MNP distribution above 10 mg Fe/mL is well recognized in the CT images with the sensitivity being limited below this concentration. Unfortunately, the cost of MRI or CT imaging systems may prove prohibitive towards large scale screening for early cancer detection applications. Ultrasound based system, like pulsed magneto-motive ultrasound (pMMUS) imaging [226] and MAT [47] may provide cost-effective imaging alternatives.

Magnetic Particle Imaging (MPI) is a tomographic imaging method taking advantage of using the nonlinear response of magnetic nanoparticles to an external magnetic field [227]. Magnetorelaxometry is based on the magnetisation of MNP in a magnetic field and the detection of their relaxing magnetisation following the switch-off the magnetic field [228]. Both approaches have high sensitivity, thus a much low detection limit. However, to further incorporate more biomedical applications in which relative high MNP concentrations are required, the MAT is potentially to cover more applications including cancer therapies, e.g. hyperthermia therapy, drug delivery and further release.

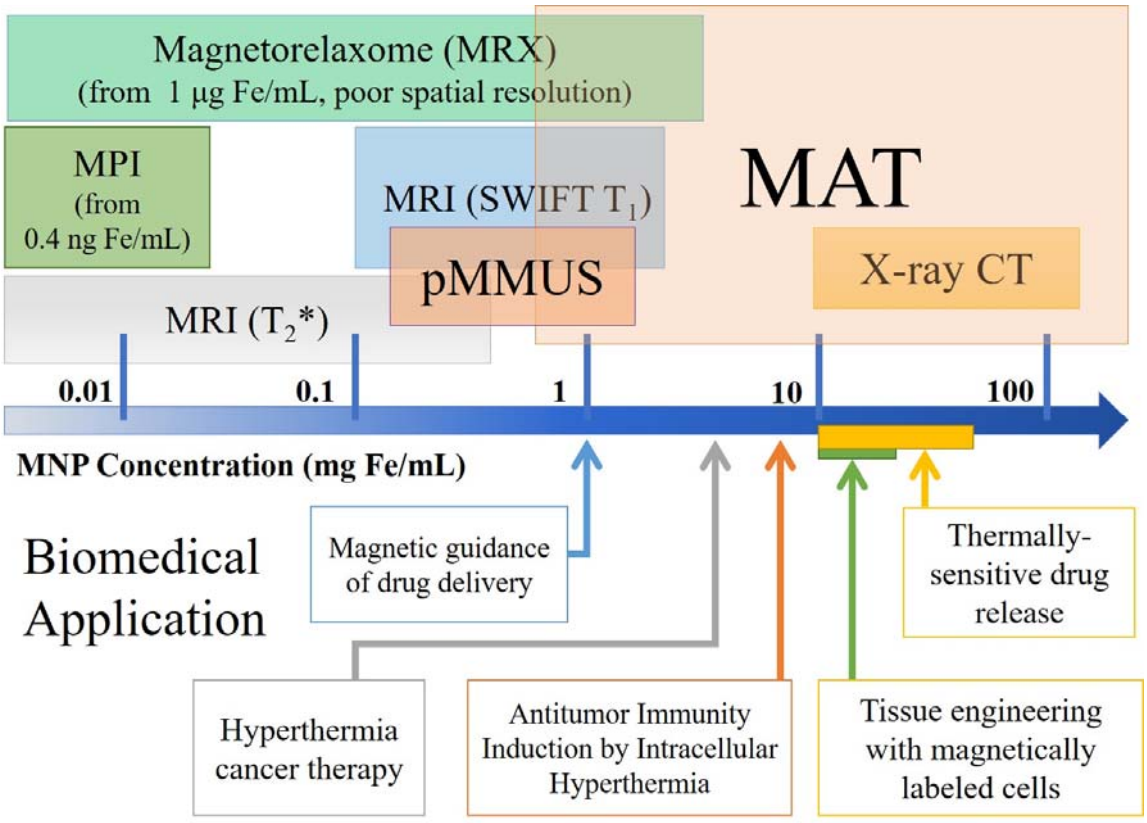

Figure 44. Application vs. imaging modalities for MNPs. MPI: magnetic particle imaging. MRI: magnetic resonance imaging. MAT: magnetoacoustic imaging. (Presented in 4th Global Conference on NanoEngineering for Medicine & Biology, Minneapolis, USA, 2015) (Courtesy of Dr. Qi Shao)

6.2.2 Simultaneous Scalp EEG and Intracranial Recordings for A Multi-scale Perspective of Ultrasound Neuromodulation.

A natural setting is more preferred than e.g. the fMRI for better understanding the ultrasound-brain interaction, and promoting to uncover the mechanism of ultrasound neuromodulation. Although the fMRI is featured with high spatial resolution, the required strong static magnetic field *per se* may alter the excitability of neural circuits [114], and the pulsed magnetic imaging sequence may also lead to inevitable auditory responses. With a much better temporal resolution, I have been devoted to use the electrophysiological recordings, e.g. scalp EEG

and intracranial electrode array to investigate the ultrasound-mediated brain activities. Combining global and local pictures of the brain responses are of high importance; therefore, a simultaneous multi-scale electrophysiological recording and interpretation framework, e.g. correlation of EEG and LFP waves and their coherence in varies bands, hold a great promise in the neuroscientific research of tFUS. With further efforts on closed-loop control of ultrasound parameters based on the real-time monitoring of brain responses, effective paradigms are hoped to be identified (Fig. 45). Overall, by successfully developing this simultaneous multi-scale technique along with the advancement of ultrasound technologies, tFUS is believed to become an effective, and widely-used brain stimulation approach.

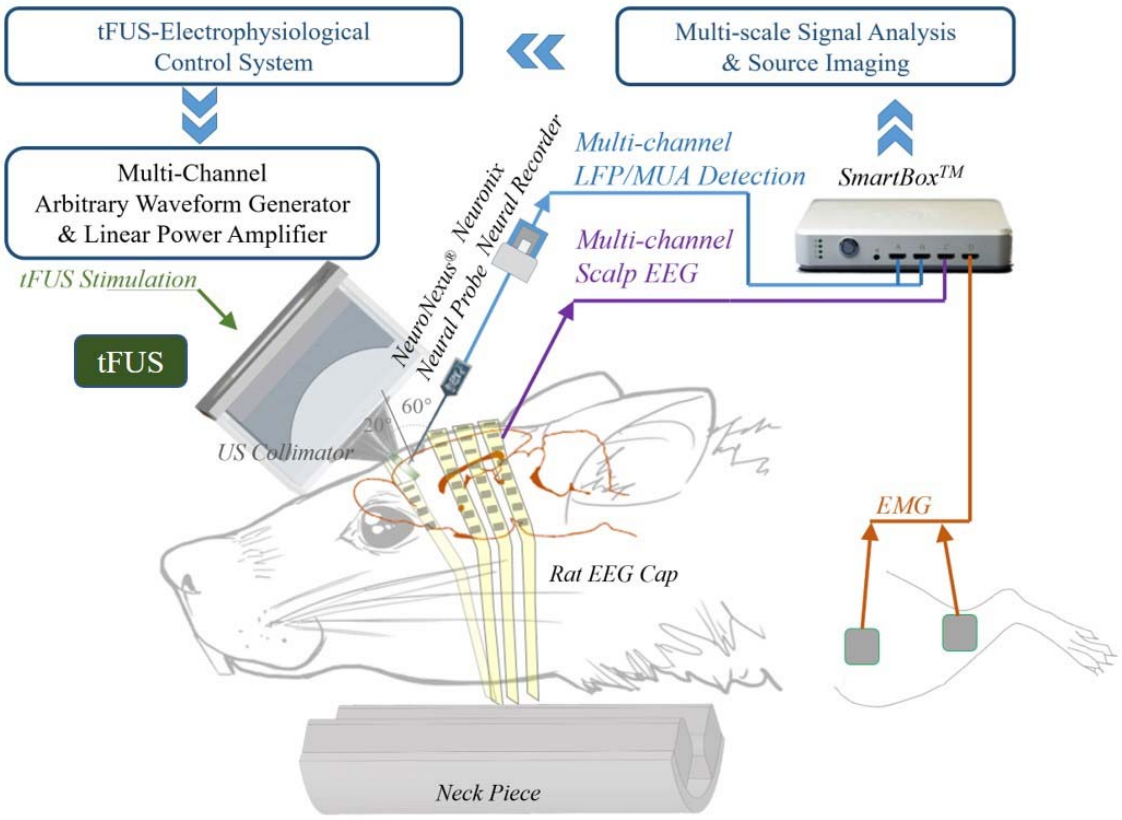

Figure 45. Simultaneous multi-scale electrophysiological recordings with closed-loop control of tFUS administration.

References

[1] X. Li, K. Yu, and B. He, “Magnetoacoustic tomography with magnetic induction (MAT-MI) for imaging electrical conductivity of biological tissue: a tutorial review,” *Phys Med Biol,* vol. 61, no. 18, pp. R249-R270, Aug 19, 2016.

[2] R. J. Sadleir, T. D. Vannorsdall, D. J. Schretlen, and B. Gordon, “Transcranial direct current stimulation (tDCS) in a realistic head model,” *Neuroimage,* vol. 51, no. 4, pp. 1310-8, Jul 15, 2010.

[3] L. A. Geddes, and L. E. Baker, “The specific resistance of biological material--a compendium of data for the biomedical engineer and physiologist,” *Med Biol Eng,* vol. 5, no. 3, pp. 271-93, May, 1967.

[4] A. J. Surowiec, S. S. Stuchly, J. B. Barr, and A. Swarup, “Dielectric properties of breast carcinoma and the surrounding tissues,” *IEEE Trans Biomed Eng,* vol. 35, no. 4, pp. 257-63, Apr, 1988.

[5] J. Jossinet, “The impedivity of freshly excised human breast tissue,” *Physiol Meas,* vol. 19, no. 1, pp. 61-75, Feb, 1998.

[6] J. Jossinet, “Variability of impedivity in normal and pathological breast tissue,” *Med Biol Eng Comput,* vol. 34, no. 5, pp. 346-50, Sep, 1996.

[7] D. Haemmerich, S. T. Staelin, J. Z. Tsai, S. Tungjitkusolmun, D. M. Mahvi, and J. G. Webster, “In vivo electrical conductivity of hepatic tumours,” *Physiol Meas,* vol. 24, no. 2, pp. 251-60, May, 2003.

[8] Y. Zou, and Z. Guo, “A review of electrical impedance techniques for breast cancer detection,” *Med Eng Phys,* vol. 25, no. 2, pp. 79-90, Mar, 2003.

[9] M. A. Fallert, M. S. Mirotznik, S. W. Downing, E. B. Savage, K. R. Foster, M. E. Josephson, and D. K. Bogen, “Myocardial electrical impedance mapping of ischemic sheep hearts and healing aneurysms,” *Circulation,* vol. 87, no. 1, pp. 199-207, Jan, 1993.

[10] J. Cinca, M. Warren, A. Carreno, M. Tresanchez, L. Armadans, P. Gomez, and J. SolerSoler, “Changes in myocardial electrical impedance induced by coronary artery occlusion in pigs with and without preconditioning - Correlation with local ST-segment potential and ventricular arrhythmias,” *Circulation,* vol. 96, no. 9, pp. 3079-3086, Nov 4, 1997.

[11] D. C. Barber, and B. H. Brown, “Applied Potential Tomography,” *Journal of Physics E-Scientific Instruments,* vol. 17, no. 9, pp. 723-733, 1984.

[12] M. Cheney, D. Isaacson, and J. C. Newell, “Electrical impedance tomography,” *Siam Review,* vol. 41, no. 1, pp. 85-101, Mar, 1999.

[13] H. Griffiths, W. R. Stewart, and W. Gough, “Magnetic induction tomography. A measuring system for biological tissues,” *Ann N Y Acad Sci,* vol. 873, pp. 335-45, Apr 20, 1999.

[14] H. S. Khang, B. I. Lee, S. H. Oh, E. J. Woo, S. Y. Lee, M. H. Cho, O. Kwon, J. R. Yoon, and J. K. Seo, “J-substitution algorithm in magnetic resonance electrical impedance tomography (MREIT): phantom experiments for static

resistivity images," *IEEE Trans Med Imaging,* vol. 21, no. 6, pp. 695-702, Jun, 2002.
[15] E. J. Woo, and J. K. Seo, "Magnetic resonance electrical impedance tomography (MREIT) for high-resolution conductivity imaging," *Physiological Measurement,* vol. 29, no. 10, pp. R1-R26, Oct, 2008.
[16] H. Wen, "Feasibility of biomedical applications of Hall effect imaging," *Ultrason Imaging,* vol. 22, no. 2, pp. 123-36, Apr, 2000.
[17] M. Joy, G. Scott, and M. Henkelman, "In vivo detection of applied electric currents by magnetic resonance imaging," *Magn Reson Imaging,* vol. 7, no. 1, pp. 89-94, Jan-Feb, 1989.
[18] E. J. Woo, H. J. Kim, A. S. Minhas, Y. T. Kim, W. C. Jeong, and O. Kwon, "Electrical conductivity imaging of lower extremities using MREIT: postmortem swine and in vivo human experiments," *Conf Proc IEEE Eng Med Biol Soc,* vol. 2008, pp. 5830-3, 2008.
[19] J. K. Seo, and E. J. Woo, "Electrical Tissue Property Imaging at Low Frequency Using MREIT," *Ieee Transactions on Biomedical Engineering,* vol. 61, no. 5, pp. 1390-1399, May, 2014.
[20] B. J. Roth, "The role of magnetic forces in biology and medicine," *Exp Biol Med (Maywood),* vol. 236, no. 2, pp. 132-7, Feb, 2011.
[21] B. C. Towe, and M. R. Islam, "A magneto-acoustic method for the noninvasive measurement of bioelectric currents," *IEEE Trans Biomed Eng,* vol. 35, no. 10, pp. 892-4, Oct, 1988.
[22] B. J. Roth, P. J. Basser, and J. P. Wikswo, Jr., "A theoretical model for magneto-acoustic imaging of bioelectric currents," *IEEE Trans Biomed Eng,* vol. 41, no. 8, pp. 723-8, Aug, 1994.
[23] H. Wen, J. Shah, and R. S. Balaban, "Hall effect imaging," *IEEE Trans Biomed Eng,* vol. 45, no. 1, pp. 119-24, Jan, 1998.
[24] A. Montalibet, J. Jossinet, and A. Matias, "Scanning electric conductivity gradients with ultrasonically-induced Lorentz force," *Ultrasonic Imaging,* vol. 23, no. 2, pp. 117-132, Apr, 2001.
[25] A. Montalibet, J. Jossinet, A. Matias, and D. Cathignol, "Electric current generated by ultrasonically induced Lorentz force in biological media," *Med Biol Eng Comput,* vol. 39, no. 1, pp. 15-20, Jan, 2001.
[26] B. J. Roth, and K. Schalte, "Ultrasonically-induced Lorentz force tomography," *Med Biol Eng Comput,* vol. 47, no. 6, pp. 573-7, Jun, 2009.
[27] S. Haider, A. Hrbek, and Y. Xu, "Magneto-acousto-electrical tomography: a potential method for imaging current density and electrical impedance," *Physiol Meas,* vol. 29, no. 6, pp. S41-50, Jun, 2008.
[28] E. Renzhiglova, V. Ivantsiv, and Y. Xu, "Difference frequency magneto-acousto-electrical tomography (DF-MAET): application of ultrasound-induced radiation force to imaging electrical current density," *IEEE Trans Ultrason Ferroelectr Freq Control,* vol. 57, no. 11, pp. 2391-402, Nov, 2010.
[29] L. Kunyansky, "A mathematical model and inversion procedure for magneto-acousto-electric tomography," *Inverse Problems,* vol. 28, no. 3, Mar, 2012.

[30] P. Grasland-Mongrain, J. M. Mari, J. Y. Chapelon, and C. Lafon, “Lorentz force electrical impedance tomography,” *Irbm,* vol. 34, no. 4-5, pp. 357-360, Nov, 2013.
[31] P. Grasland-Mongrain, F. Destrempes, J. M. Mari, R. Souchon, S. Catheline, J. Y. Chapelon, C. Lafon, and G. Cloutier, “Acousto-electrical speckle pattern in Lorentz force electrical impedance tomography,” *Physics in Medicine and Biology,* vol. 60, no. 9, pp. 3747-3757, May 7, 2015.
[32] B. He, “High-resolution Functional Source and Impedance Imaging,” *Conf Proc IEEE Eng Med Biol Soc,* vol. 4, pp. 4178-82, 2005.
[33] Y. Xu, and B. He, “Magnetoacoustic tomography with magnetic induction (MAT-MI),” *Phys Med Biol,* vol. 50, no. 21, pp. 5175-87, Nov 7, 2005.
[34] X. Li, Y. Xu, and B. He, “Imaging electrical impedance from acoustic measurements by means of magnetoacoustic tomography with magnetic induction (MAT-MI),” *IEEE Trans Biomed Eng,* vol. 54, no. 2, pp. 323-30, Feb, 2007.
[35] X. Li, X. Li, S. Zhu, and B. He, “Solving the forward problem of magnetoacoustic tomography with magnetic induction by means of the finite element method,” *Phys Med Biol,* vol. 54, no. 9, pp. 2667-82, May 7, 2009.
[36] Q. Ma, and B. He, “Investigation on magnetoacoustic signal generation with magnetic induction and its application to electrical conductivity reconstruction,” *Phys Med Biol,* vol. 52, no. 16, pp. 5085-99, Aug 21, 2007.
[37] L. Zhou, X. Li, S. Zhu, and B. He, “Magnetoacoustic tomography with magnetic induction (MAT-MI) for breast tumor imaging: numerical modeling and simulation,” *Phys Med Biol,* vol. 56, no. 7, pp. 1967-83, Apr 7, 2011.
[38] X. Li, Y. Xu, and B. He, “Magnetoacoustic tomography with magnetic induction for imaging electrical impedance of biological tissue,” *Journal of Applied Physics,* vol. 99, no. 6, Mar 15, 2006.
[39] R. Xia, X. Li, and B. He, “Magnetoacoustic tomographic imaging of electrical impedance with magnetic induction,” *Appl Phys Lett,* vol. 91, no. 8, pp. 83903, Aug 22, 2007.
[40] X. Sun, D. Fang, D. Zhang, and Q. Ma, “Acoustic dipole radiation based electrical impedance contrast imaging approach of magnetoacoustic tomography with magnetic induction,” *Med Phys,* vol. 40, no. 5, pp. 052902, May, 2013.
[41] G. Hu, and B. He, “Magnetoacoustic imaging of electrical conductivity of biological tissues at a spatial resolution better than 2 mm,” *PLoS One,* vol. 6, no. 8, pp. e23421, 2011.
[42] G. Hu, E. Cressman, and B. He, “Magnetoacoustic imaging of human liver tumor with magnetic induction,” *Appl Phys Lett,* vol. 98, no. 2, pp. 23703, Jan 10, 2011.
[43] G. Hu, X. Li, and B. He, “Imaging biological tissues with electrical conductivity contrast below 1 S m by means of magnetoacoustic tomography with magnetic induction,” *Appl Phys Lett,* vol. 97, no. 10, Sep 6, 2010.

[44] X. Li, and B. He, “Multi-excitation magnetoacoustic tomography with magnetic induction for bioimpedance imaging,” *IEEE Trans Med Imaging,* vol. 29, no. 10, pp. 1759-67, Oct, 2010.
[45] L. Mariappan, and B. He, “Magnetoacoustic tomography with magnetic induction: bioimepedance reconstruction through vector source imaging,” *IEEE Trans Med Imaging,* vol. 32, no. 3, pp. 619-27, Mar, 2013.
[46] L. Guo, G. Liu, and H. Xia, “Magneto-Acousto-Electrical Tomography With Magnetic Induction for Conductivity Reconstruction,” *Biomedical Engineering, IEEE Transactions on,* vol. 62, no. 9, pp. 2114-2124, 2015.
[47] L. Mariappan, Q. Shao, C. Jiang, K. Yu, S. Ashkenazi, J. C. Bischof, and B. He, “Magneto acoustic tomography with short pulsed magnetic field for in-vivo imaging of magnetic iron oxide nanoparticles,” *Nanomedicine*, Dec 2, 2015.
[48] V. S. Kalambur, B. Han, B. E. Hammer, T. W. Shield, and J. C. Bischof, “In vitro characterization of movement, heating and visualization of magnetic nanoparticles for biomedical applications,” *Nanotechnology,* vol. 16, no. 8, pp. 1221-1233, Aug, 2005.
[49] A. Ito, Y. Kuga, H. Honda, H. Kikkawa, A. Horiuchi, Y. Watanabe, and T. Kobayashi, “Magnetite nanoparticle-loaded anti-HER2 immunoliposomes for combination of antibody therapy with hyperthermia,” *Cancer Letters,* vol. 212, no. 2, pp. 167-175, Aug 30, 2004.
[50] B. Le, M. Shinkai, T. Kitade, H. Honda, J. Yoshida, T. Wakabayashi, and T. Kobayashi, “Preparation of tumor-specific magnetoliposomes and their application for hyperthermia,” *Journal of Chemical Engineering of Japan,* vol. 34, no. 1, pp. 66-72, Jan, 2001.
[51] C. L. Carter, C. Allen, and D. E. Henson, “Relation of tumor size, lymph node status, and survival in 24,740 breast cancer cases,” *Cancer,* vol. 63, no. 1, pp. 181-7, Jan 1, 1989.
[52] B. He, R. Baird, R. Butera, A. Datta, S. George, B. Hecht, A. Hero, G. Lazzi, R. C. Lee, J. Liang, M. Neuman, G. C. Y. Peng, E. J. Perreault, M. Ramasubramanian, M. D. Wang, J. Wikswo, G. Z. Yang, and Y. T. Zhang, “Grand Challenges in Interfacing Engineering With Life Sciences and Medicine,” *Ieee Transactions on Biomedical Engineering,* vol. 60, no. 3, pp. 589-598, Mar, 2013.
[53] J. Bercoff, M. Tanter, and M. Fink, “Supersonic shear imaging: a new technique for soft tissue elasticity mapping,” *IEEE Trans Ultrason Ferroelectr Freq Control,* vol. 51, no. 4, pp. 396-409, Apr, 2004.
[54] X. Zhang, J. Liu, and B. He, “Magnetic-Resonance-Based Electrical Properties Tomography: A Review,” *Biomedical Engineering, IEEE Reviews,* vol. 7, pp. 87 - 96, 2014.
[55] N. Gao, S. A. Zhu, and B. He, “Estimation of electrical conductivity distribution within the human head from magnetic flux density measurement,” *Physics in Medicine and Biology,* vol. 50, no. 11, pp. 2675-2687, Jun 7, 2005.

[56] R. Yang, X. Li, A. Song, B. He, and R. Yan, “A 3-D reconstruction solution to current density imaging based on acoustoelectric effect by deconvolution: a simulation study,” *IEEE Trans Biomed Eng,* vol. 60, no. 5, pp. 1181-90, May, 2013.

[57] E. J. Bond, L. Xu, S. C. Hagness, and B. D. Van Veen, “Microwave imaging via space-time beamforming for early detection of breast cancer,” *IEEE Transactions on Antennas and Propagation,* vol. 51, no. 8, pp. 1690-1705, 2003.

[58] H. F. Zhang, K. Maslov, G. Stoica, and L. V. Wang, “Functional photoacoustic microscopy for high-resolution and noninvasive in vivo imaging,” *Nat Biotechnol,* vol. 24, no. 7, pp. 848-51, Jul, 2006.

[59] M. A. Hahn, A. K. Singh, P. Sharma, S. C. Brown, and B. M. Moudgil, “Nanoparticles as contrast agents for in-vivo bioimaging: current status and future perspectives,” *Analytical and Bioanalytical Chemistry,* vol. 399, no. 1, pp. 3-27, Jan, 2011.

[60] M. L. Etheridge, and J. C. Bischof, “Optimizing Magnetic Nanoparticle Based Thermal Therapies Within the Physical Limits of Heating,” *Annals of Biomedical Engineering,* vol. 41, no. 1, pp. 78-88, Jan, 2013.

[61] I. M. Gescheit, M. Ben-David, and I. Gannot, “A Proposed Method for Thermal Specific Bioimaging and Therapy Technique for Diagnosis and Treatment of Malignant Tumors by Using Magnetic Nanoparticles,” *Advances in Optical Technologies,* vol. 2008, pp. 1-7, 2008.

[62] D. Artemov, N. Mori, B. Okollie, and Z. M. Bhujwalla, “MR molecular imaging of the Her-2/neu receptor in breast cancer cells using targeted iron oxide nanoparticles,” *Magnetic Resonance in Medicine,* vol. 49, no. 3, pp. 403-408, Mar, 2003.

[63] J. W. M. Bulte, and D. L. Kraitchman, “Iron oxide MR contrast agents for molecular and cellular imaging,” *Nmr in Biomedicine,* vol. 17, no. 7, pp. 484-499, Nov, 2004.

[64] J. J. Zhang, R. Chamberlain, M. Etheridge, D. Idiyatullin, C. Corum, J. Bischof, and M. Garwood, “Quantifying Iron-Oxide Nanoparticles at High Concentration Based on Longitudinal Relaxation Using a Three-Dimensional SWIFT Look-Locker Sequence,” *Magnetic Resonance in Medicine,* vol. 71, no. 6, pp. 1982-1988, Jun, 2014.

[65] M. L. Etheridge, K. R. Hurley, J. Zhang, S. Jeon, H. L. Ring, C. Hogan, C. L. Haynes, M. Garwood, and J. C. Bischof, “Accounting for biological aggregation in heating and imaging of magnetic nanoparticles,” *Technology (Singap World Sci),* vol. 2, no. 3, pp. 214-228, Sep, 2014.

[66] U. Gneveckow, A. Jordan, R. Scholz, V. Bruss, N. Waldofner, J. Ricke, A. Feussner, B. Hildebrandt, B. Rau, and P. Wust, “Description and characterization of the novel hyperthermia- and thermoablation-system MFH 300F for clinical magnetic fluid hyperthermia,” *Med Phys,* vol. 31, no. 6, pp. 1444-51, Jun, 2004.

[67] I. Steinberg, M. Ben-David, and I. Gannot, “A new method for tumor detection using induced acoustic waves from tagged magnetic

nanoparticles," *Nanomedicine-Nanotechnology Biology and Medicine,* vol. 8, no. 5, pp. 569-579, Jul, 2012.

[68] A. Levy, A. Dayan, M. Ben-David, and I. Gannot, "A new thermography-based approach to early detection of cancer utilizing magnetic nanoparticles theory simulation and in vitro validation," *Nanomedicine,* vol. 6, no. 6, pp. 786-96, Dec, 2010.

[69] R. S. C. Cobbold, *Foundations of biomedical ultrasound*, New York: Oxford University Press, 2007.

[70] A. A. Oraevsky, A. A. Karabutov, and E. V. Savateeva, "Enhancement of optoacoustic tissue contrast with absorbing nanoparticles," *Hybrid and Novel Imaging and New Optical Instrumentation for Biomedical Applications,* vol. 4434, pp. 60-69, 2001.

[71] Y. W. Wang, X. Y. Xie, X. D. Wang, G. Ku, K. L. Gill, D. P. O'Neal, G. Stoica, and L. V. Wang, "Photoacoustic tomography of a nanoshell contrast agent in the in vivo rat brain," *Nano Letters,* vol. 4, no. 9, pp. 1689-1692, Sep, 2004.

[72] A. L. Oldenburg, F. J. J. Toublan, K. S. Suslick, A. Wei, and S. A. Boppart, "Magnetomotive contrast for in vivo optical coherence tomography," *Optics Express,* vol. 13, no. 17, pp. 6597-6614, Aug 22, 2005.

[73] R. John, R. Rezaeipoor, S. G. Adie, E. J. Chaney, A. L. Oldenburg, M. Marjanovic, J. P. Haldar, B. P. Sutton, and S. A. Boppart, "In vivo magnetomotive optical molecular imaging using targeted magnetic nanoprobes," *Proceedings of the National Academy of Sciences of the United States of America,* vol. 107, no. 18, pp. 8085-8090, May 4, 2010.

[74] M. Mehrmohammadi, J. Oh, L. Ma, E. Yantsen, T. Larson, S. Mallidi, S. Park, K. P. Johnston, K. Sokolov, T. Milner, and S. Emelianov, "Imaging of iron oxide nanoparticles using magneto-motive ultrasound," *2007 Ieee Ultrasonics Symposium Proceedings, Vols 1-6*, pp. 652-+, 2007.

[75] J. Oh, M. D. Feldman, J. Kim, C. Condit, S. Emelianov, and T. E. Milner, "Detection of magnetic nanoparticles in tissue using magneto-motive ultrasound," *Nanotechnology,* vol. 17, no. 16, pp. 4183-90, Aug 28, 2006.

[76] G. Hu, and B. He, "Magnetoacoustic imaging of magnetic iron oxide nanoparticles embedded in biological tissues with microsecond magnetic stimulation," *Appl Phys Lett,* vol. 100, no. 1, pp. 13704-137043, Jan 2, 2012.

[77] Y. Xu, and L. H. V. Wang, "Time reversal and its application to tomography with diffracting sources," *Physical Review Letters,* vol. 92, no. 3, Jan 23, 2004.

[78] K. Ranganathan, and W. F. Walker, "A novel beamformer design method for medical ultrasound. Part I: Theory," *IEEE Trans Ultrason Ferroelectr Freq Control,* vol. 50, no. 1, pp. 15-24, Jan, 2003.

[79] L. Zhou, S. A. Zhu, and B. He, "A Reconstruction Algorithm of Magnetoacoustic Tomography With Magnetic Induction for an Acoustically Inhomogeneous Tissue," *Ieee Transactions on Biomedical Engineering,* vol. 61, no. 6, pp. 1739-1746, Jun, 2014.

[80] R. E. Rosensweig, “Heating magnetic fluid with alternating magnetic field,” *Journal of Magnetism and Magnetic Materials,* vol. 252, no. 1-3, pp. 370-374, Nov, 2002.
[81] C. Fang, and M. Q. Zhang, “Multifunctional magnetic nanoparticles for medical imaging applications,” *Journal of Materials Chemistry,* vol. 19, no. 35, pp. 6258-6266, 2009.
[82] R. Weissleder, D. D. Stark, B. L. Engelstad, B. R. Bacon, C. C. Compton, D. L. White, P. Jacobs, and J. Lewis, “Superparamagnetic Iron-Oxide - Pharmacokinetics and Toxicity,” *American Journal of Roentgenology,* vol. 152, no. 1, pp. 167-173, Jan, 1989.
[83] K. Yu, A. Sohrabpour, and B. He, “Electrophysiological Source Imaging of Brain Networks Perturbed by Low-Intensity Transcranial Focused Ultrasound,” *IEEE Trans Biomed Eng,* vol. 63, no. 9, pp. 1787-1794, Sep, 2016.
[84] B. He, L. Yang, C. Wilke, and H. Yuan, “Electrophysiological imaging of brain activity and connectivity-challenges and opportunities,” *IEEE Trans Biomed Eng,* vol. 58, no. 7, pp. 1918-31, Jul, 2011.
[85] B. He, T. Coleman, G. M. Genin, G. Glover, X. Hu, N. Johnson, T. Liu, S. Makeig, P. Sajda, and K. Ye, “Grand challenges in mapping the human brain: NSF workshop report,” *IEEE Trans Biomed Eng,* vol. 60, no. 11, pp. 2983-92, Nov, 2013.
[86] B. J. Edelman, N. Johnson, A. Sohrabpour, S. Tong, N. Thakor, and B. He, “Systems Neuroengineering: Understanding and Interacting with the Brain,” *Engineering,* vol. 1, no. 3, pp. 292-308, Sep, 2015.
[87] R. T. LaLumiere, “A new technique for controlling the brain: Optogenetics and its potential for use in research and the clinic,” *Brain Stimul,* vol. 4, pp. 1-6, 2011.
[88] M. K. Lyons, “Deep brain stimulation: current and future clinical applications,” *Mayo Clin Proc,* vol. 86, pp. 662-672, 2011.
[89] M. D. Johnson, H. H. Lim, T. I. Netoff, A. T. Connolly, N. Johnson, A. Roy, A. Holt, K. O. Lim, J. R. Carey, J. L. Vitek, and B. He, “Neuromodulation for Brain Disorders: Challenges and Opportunities,” *Ieee Transactions on Biomedical Engineering,* vol. 60, no. 3, pp. 610-624, Mar, 2013.
[90] D. Panescu, “Vagus nerve stimulation for the treatment of depression,” *IEEE Eng Med Biol Mag,* vol. 24, no. 6, pp. 68-72, Nov-Dec, 2005.
[91] A. Jelovac, E. Kolshus, and D. M. McLoughlin, “Relapse following successful electroconvulsive therapy for major depression: a meta-analysis,” *Neuropsychopharmacology,* vol. 38, no. 12, pp. 2467-74, Nov, 2013.
[92] J.-P. Lefaucheur, N. André-Obadia, A. Antal, S. S. Ayache, C. Baeken, D. H. Benninger, R. M. Cantello, M. Cincotta, M. de Carvalho, D. De Ridder, H. Devanne, V. Di Lazzaro, S. R. Filipović, F. C. Hummel, S. K. Jääskeläinen, V. K. Kimiskidis, G. Koch, B. Langguth, T. Nyffeler, A. Oliviero, F. Padberg, E. Poulet, S. Rossi, P. M. Rossini, J. C. Rothwell, C. Schönfeldt-Lecuona, H. R. Siebner, C. W. Slotema, C. J. Stagg, J. Valls-Sole, U. Ziemann, W. Paulus, and L. Garcia-Larrea, “Evidence-based guidelines on

the therapeutic use of repetitive transcranial magnetic stimulation (rTMS)," *Clinical Neurophysiology,* vol. 125, no. 11, pp. 2150-2206, 2014.

[93] M. A. Nitsche, and W. Paulus, "Excitability changes induced in the human motor cortex by weak transcranial direct current stimulation," *Journal of Physiology-London,* vol. 527, no. 3, pp. 633-639, Sep 15, 2000.

[94] A. Roy, B. Baxter, and B. He, "High-Definition Transcranial Direct Current Stimulation Induces Both Acute and Persistent Changes in Broadband Cortical Synchronization: A Simultaneous tDCS-EEG Study," *Ieee Transactions on Biomedical Engineering,* vol. 61, no. 7, pp. 1967-1978, Jul, 2014.

[95] R. Kanai, L. Chaieb, A. Antal, V. Walsh, and W. Paulus, "Frequency-dependent electrical stimulation of the visual cortex," *Curr Biol,* vol. 18, no. 23, pp. 1839-43, Dec 9, 2008.

[96] H. Kim, S. D. Lee, A. Chiu, S. S. Yoo, and S. Park, "Estimation of the spatial profile of neuromodulation and the temporal latency in motor responses induced by focused ultrasound brain stimulation," *Neuroreport,* vol. 25, no. 7, pp. 475-9, May 7, 2014.

[97] W. Legon, T. F. Sato, A. Opitz, J. Mueller, A. Barbour, A. Williams, and W. J. Tyler, "Transcranial focused ultrasound modulates the activity of primary somatosensory cortex in humans," *Nat Neurosci,* vol. 17, no. 2, pp. 322-9, Feb, 2014.

[98] E. Mehic, J. M. Xu, C. J. Caler, N. K. Coulson, C. T. Moritz, and P. D. Mourad, "Increased anatomical specificity of neuromodulation via modulated focused ultrasound," *PLoS One,* vol. 9, no. 2, pp. e86939, 2014.

[99] S. S. Yoo, A. Bystritsky, J. H. Lee, Y. Zhang, K. Fischer, B. K. Min, N. J. McDannold, A. Pascual-Leone, and F. A. Jolesz, "Focused ultrasound modulates region-specific brain activity," *Neuroimage,* vol. 56, no. 3, pp. 1267-75, Jun 1, 2011.

[100] S. S. Yoo, H. Kim, B. K. Min, E. Franck, and S. Park, "Transcranial focused ultrasound to the thalamus alters anesthesia time in rats," *Neuroreport,* vol. 22, no. 15, pp. 783-787, Oct 26, 2011.

[101] T. Deffieux, Y. Younan, N. Wattiez, M. Tanter, P. Pouget, and J. F. Aubry, "Low-intensity focused ultrasound modulates monkey visuomotor behavior," *Curr Biol,* vol. 23, no. 23, pp. 2430-3, Dec 2, 2013.

[102] W. Lee, S. D. Lee, M. Y. Park, L. Foley, E. Purcell-Estabrook, H. Kim, K. Fischer, L. S. Maeng, and S. S. Yoo, "Image-Guided Focused Ultrasound-Mediated Regional Brain Stimulation in Sheep," *Ultrasound Med Biol,* vol. 42, no. 2, pp. 459-70, Feb, 2016.

[103] S. Hameroff, M. Trakas, C. Duffield, E. Annabi, M. B. Gerace, P. Boyle, A. Lucas, Q. Amos, A. Buadu, and J. J. Badal, "Transcranial ultrasound (TUS) effects on mental states: a pilot study," *Brain Stimul,* vol. 6, no. 3, pp. 409-15, May, 2013.

[104] W. Legon, A. Rowlands, A. Opitz, T. F. Sato, and W. J. Tyler, "Pulsed ultrasound differentially stimulates somatosensory circuits in humans as indicated by EEG and FMRI," *PLoS One,* vol. 7, no. 12, pp. e51177, 2012.

[105] J. Mueller, W. Legon, A. Opitz, T. F. Sato, and W. J. Tyler, “Transcranial Focused Ultrasound Modulates Intrinsic and Evoked EEG Dynamics,” *Brain Stimul*, Sep 6, 2014.
[106] W. Lee, H. Kim, Y. Jung, I. U. Song, Y. A. Chung, and S. S. Yoo, “Image-guided transcranial focused ultrasound stimulates human primary somatosensory cortex,” *Sci Rep,* vol. 5, pp. 8743, 2015.
[107] K. Ashkan, P. Rogers, H. Bergman, and I. Ughratdar, “Insights into the mechanisms of deep brain stimulation,” *Nat Rev Neurol,* vol. 13, no. 9, pp. 548-554, Sep, 2017.
[108] A. T. Barker, R. Jalinous, and I. L. Freeston, “Non-invasive magnetic stimulation of human motor cortex,” *Lancet,* vol. 1, no. 8437, pp. 1106-7, May 11, 1985.
[109] M. Kobayashi, and A. Pascual-Leone, “Transcranial magnetic stimulation in neurology,” *The Lancet Neurology,* vol. 2, no. 3, pp. 145-156, 2003.
[110] M. A. Nitsche, and W. Paulus, “Excitability changes induced in the human motor cortex by weak transcranial direct current stimulation,” *J Physiol,* vol. 527 Pt 3, pp. 633-9, Sep 15, 2000.
[111] J. C. Horvath, J. D. Forte, and O. Carter, “Evidence that transcranial direct current stimulation (tDCS) generates little-to-no reliable neurophysiologic effect beyond MEP amplitude modulation in healthy human subjects: A systematic review,” *Neuropsychologia,* vol. 66, pp. 213-36, Jan, 2015.
[112] Y. Tufail, A. Matyushov, N. Baldwin, M. L. Tauchmann, J. Georges, A. Yoshihiro, S. I. H. Tillery, and W. J. Tyler, “Transcranial Pulsed Ultrasound Stimulates Intact Brain Circuits,” *Neuron,* vol. 66, no. 5, pp. 681-694, Jun 10, 2010.
[113] W. Lee, H. C. Kim, Y. Jung, Y. A. Chung, I. U. Song, J. H. Lee, and S. S. Yoo, “Transcranial focused ultrasound stimulation of human primary visual cortex,” *Sci Rep,* vol. 6, pp. 34026, Sep 23, 2016.
[114] A. Oliviero, L. Mordillo-Mateos, P. Arias, I. Panyavin, G. Foffani, and J. Aguilar, “Transcranial static magnetic field stimulation of the human motor cortex,” *J Physiol,* vol. 589, no. Pt 20, pp. 4949-58, Oct 15, 2011.
[115] K. Deisseroth, and P. Hegemann, “The form and function of channelrhodopsin,” *Science,* vol. 357, no. 6356, 2017.
[116] E. S. Boyden, F. Zhang, E. Bamberg, G. Nagel, and K. Deisseroth, “Millisecond-timescale, genetically targeted optical control of neural activity,” *Nat Neurosci,* vol. 8, no. 9, pp. 1263-8, Sep, 2005.
[117] A. M. Packer, B. Roska, and M. Hausser, “Targeting neurons and photons for optogenetics,” *Nat Neurosci,* vol. 16, no. 7, pp. 805-15, Jul, 2013.
[118] P. Rajasethupathy, E. Ferenczi, and K. Deisseroth, “Targeting Neural Circuits,” *Cell,* vol. 165, no. 3, pp. 524-34, Apr 21, 2016.
[119] J. Delbeke, L. Hoffman, K. Mols, D. Braeken, and D. Prodanov, “And Then There Was Light: Perspectives of Optogenetics for Deep Brain Stimulation and Neuromodulation,” *Front Neurosci,* vol. 11, pp. 663, 2017.
[120] M. Hallett, “Transcranial magnetic stimulation: a primer,” *Neuron,* vol. 55, no. 2, pp. 187-99, Jul 19, 2007.

[121] S. M. Goetz, B. Luber, S. H. Lisanby, D. L. Murphy, I. C. Kozyrkov, W. M. Grill, and A. V. Peterchev, “Enhancement of Neuromodulation with Novel Pulse Shapes Generated by Controllable Pulse Parameter Transcranial Magnetic Stimulation,” *Brain Stimul,* vol. 9, no. 1, pp. 39-47, Jan-Feb, 2016.
[122] M. C. Ridding, and J. C. Rothwell, “Is there a future for therapeutic use of transcranial magnetic stimulation?,” *Nature Reviews Neuroscience,* vol. 8, pp. 559, 07/01/online, 2007.
[123] M. A. Nitsche, and W. Paulus, “Sustained excitability elevations induced by transcranial DC motor cortex stimulation in humans,” *Neurology,* vol. 57, no. 10, pp. 1899-901, Nov 27, 2001.
[124] K. Nakagawa, and K. Nakazawa, “Static magnetic field stimulation applied over the cervical spinal cord can decrease corticospinal excitability in finger muscle,” *Clinical Neurophysiology Practice,* vol. 3, pp. 49-53, 2018/01/01/, 2018.
[125] N. Grossman, D. Bono, N. Dedic, S. B. Kodandaramaiah, A. Rudenko, H. J. Suk, A. M. Cassara, E. Neufeld, N. Kuster, L. H. Tsai, A. Pascual-Leone, and E. S. Boyden, “Noninvasive Deep Brain Stimulation via Temporally Interfering Electric Fields,” *Cell,* vol. 169, no. 6, pp. 1029-1041 e16, Jun 01, 2017.
[126] R. Polania, M. A. Nitsche, and C. C. Ruff, “Studying and modifying brain function with non-invasive brain stimulation,” *Nat Neurosci,* vol. 21, no. 2, pp. 174-187, Feb, 2018.
[127] O. Naor, S. Krupa, and S. Shoham, “Ultrasonic neuromodulation,” *J Neural Eng,* vol. 13, no. 3, pp. 031003, Jun, 2016.
[128] A. Haritonova, D. Liu, and E. S. Ebbini, “In Vivo application and localization of transcranial focused ultrasound using dual-mode ultrasound arrays,” *IEEE Trans Ultrason Ferroelectr Freq Control,* vol. 62, no. 12, pp. 2031-42, Dec, 2015.
[129] R. L. King, J. R. Brown, W. T. Newsome, and K. B. Pauly, “Effective parameters for ultrasound-induced in vivo neurostimulation,” *Ultrasound Med Biol,* vol. 39, no. 2, pp. 312-31, Feb, 2013.
[130] P. P. Ye, J. R. Brown, and K. B. Pauly, “Frequency Dependence of Ultrasound Neurostimulation in the Mouse Brain,” *Ultrasound Med Biol,* vol. 42, no. 7, pp. 1512-30, Jul, 2016.
[131] W. Zhou, J. Wang, K. Wang, B. Huang, L. Niu, F. Li, F. Cai, Y. Chen, X. Liu, X. Zhang, H. Cheng, L. Kang, L. Meng, and H. Zheng, “Ultrasound neuro-modulation chip: activation of sensory neurons in Caenorhabditis elegans by surface acoustic waves,” *Lab Chip,* vol. 17, no. 10, pp. 1725-1731, May 16, 2017.
[132] S. Ibsen, A. Tong, C. Schutt, S. Esener, and S. H. Chalasani, “Sonogenetics is a non-invasive approach to activating neurons in Caenorhabditis elegans,” *Nat Commun,* vol. 6, pp. 8264, 2015.
[133] J. Kubanek, P. Shukla, A. Das, S. A. Baccus, and M. B. Goodman, “Ultrasound Elicits Behavioral Responses through Mechanical Effects on

Neurons and Ion Channels in a Simple Nervous System," *The Journal of Neuroscience,* vol. 38, no. 12, pp. 3081-3091, 2018.
[134] R. F. Dallapiazza, K. F. Timbie, S. Holmberg, J. Gatesman, M. B. Lopes, R. J. Price, G. W. Miller, and W. J. Elias, "Noninvasive neuromodulation and thalamic mapping with low-intensity focused ultrasound," *J Neurosurg,* vol. 128, no. 3, pp. 875-884, Mar, 2018.
[135] R. D. Airan, R. A. Meyer, N. P. Ellens, K. R. Rhodes, K. Farahani, M. G. Pomper, S. D. Kadam, and J. J. Green, "Noninvasive Targeted Transcranial Neuromodulation via Focused Ultrasound Gated Drug Release from Nanoemulsions," *Nano Lett,* vol. 17, no. 2, pp. 652-659, Feb 08, 2017.
[136] R. W. Bourdeau, A. Lee-Gosselin, A. Lakshmanan, A. Farhadi, S. R. Kumar, S. P. Nety, and M. G. Shapiro, "Acoustic reporter genes for noninvasive imaging of microorganisms in mammalian hosts," *Nature,* vol. 553, no. 7686, pp. 86-90, Jan 3, 2018.
[137] H. A. S. Kamimura, S. Wang, H. Chen, Q. Wang, C. Aurup, C. Acosta, A. A. O. Carneiro, and E. E. Konofagou, "Focused ultrasound neuromodulation of cortical and subcortical brain structures using 1.9 MHz," *Medical Physics,* vol. 43, no. 10, pp. 5730-5735, 2016.
[138] W. Legon, L. Ai, P. Bansal, and J. K. Mueller, "Neuromodulation with single-element transcranial focused ultrasound in human thalamus," *Hum Brain Mapp*, Jan 29, 2018.
[139] F. Darvas, E. Mehic, C. J. Caler, J. G. Ojemann, and P. D. Mourad, "Toward Deep Brain Monitoring with Superficial EEG Sensors Plus Neuromodulatory Focused Ultrasound," *Ultrasound Med Biol,* vol. 42, no. 8, pp. 1834-47, Aug, 2016.
[140] B. He, "Focused Ultrasound Help Realize High Spatiotemporal Brain Imaging? - A Concept on Acousto-Electrophysiological Neuroimaging," *IEEE Transactions on Biomedical Engineering,* vol. 63, no. 12, pp. 2654-2656, 2016.
[141] G. F. Li, H. X. Zhao, H. Zhou, F. Yan, J. Y. Wang, C. X. Xu, C. Z. Wang, L. L. Niu, L. Meng, S. Wu, H. L. Zhang, W. B. Qiu, and H. R. Zheng, "Improved Anatomical Specificity of Non-invasive Neuro-stimulation by High Frequency (5 MHz) Ultrasound," *Sci Rep,* vol. 6, pp. 24738, Apr 20, 2016.
[142] W. Lee, Y. A. Chung, Y. Jung, I. U. Song, and S. S. Yoo, "Simultaneous acoustic stimulation of human primary and secondary somatosensory cortices using transcranial focused ultrasound," *BMC Neurosci,* vol. 17, no. 1, pp. 68, Oct 26, 2016.
[143] R. Xia, X. Li, and B. He, "Reconstruction of vectorial acoustic sources in time-domain tomography," *IEEE Trans Med Imaging,* vol. 28, no. 5, pp. 669-75, May, 2009.
[144] X. Li, Y. Xu, and B. He, "A Phantom Study of Magnetoacoustic Tomography with Magnetic Induction (MAT-MI) for Imaging Electrical Impedance of Biological Tissue," *J Appl Phys,* vol. 99, pp. 066112, Mar 29, 2006.

[145] Q. Ma, and B. He, “Magnetoacoustic tomography with magnetic induction: a rigorous theory,” *IEEE Trans Biomed Eng,* vol. 55, no. 2 Pt 2, pp. 813-6, Feb, 2008.
[146] K. Yu, Q. Shao, S. Ashkenazi, J. C. Bischof, and B. He, “In Vivo Electrical Conductivity Contrast Imaging in a Mouse Model of Cancer Using High-Frequency Magnetoacoustic Tomography With Magnetic Induction (hfMAT-MI),” *IEEE Transactions on Medical Imaging,* vol. 35, no. 10, pp. 2301-2311, 2016.
[147] L. Guo, G. Liu, and Y. Yang, “Difference frequency magnetoacoustic tomography without static magnetic field,” *Applied Physics Express,* vol. 8, no. 8, pp. 086601, 2015.
[148] G. B. Arfken, H. J. Weber, and F. E. Harris, "Chapter 10 - Green's Functions," *Mathematical Methods for Physicists (Seventh Edition)*, G. B. A. J. W. E. Harris, ed., pp. 447-467, Boston: Academic Press, 2013.
[149] J. A. Jensen, “Medical ultrasound imaging,” *Prog Biophys Mol Biol,* vol. 93, no. 1-3, pp. 153-65, Jan-Apr, 2007.
[150] D. B. Montgomery, and J. Terrell, *Some useful information for the design of air-core solenoids*, Cambridge, MA: Defense Technical Information Center, 1961.
[151] W. R. Smythe, *Static and dynamic electricity*, 2nd ed., p.^pp. 260-306, New York: McGraw-Hill, 1950.
[152] L. Mariappan, X. Li, and B. He, “B-scan based acoustic source reconstruction for magnetoacoustic tomography with magnetic induction (MAT-MI),” *IEEE Trans Biomed Eng,* vol. 58, no. 3, pp. 713-20, Mar, 2011.
[153] J. A. Jensen, and N. B. Svendsen, “Calculation of pressure fields from arbitrarily shaped, apodized, and excited ultrasound transducers,” *IEEE Trans Ultrason Ferroelectr Freq Control,* vol. 39, no. 2, pp. 262-7, 1992.
[154] Q. Shao, E. Morgounova, C. Jiang, J. Choi, J. Bischof, and S. Ashkenazi, “In vivo photoacoustic lifetime imaging of tumor hypoxia in small animals,” *J Biomed Opt,* vol. 18, no. 7, pp. 076019, 2013.
[155] Q. Shao, and S. Ashkenazi, “Photoacoustic lifetime imaging for direct in vivo tissue oxygen monitoring,” *J Biomed Opt,* vol. 20, no. 3, pp. 36004, Mar 1, 2015.
[156] S. Rush, J. A. Abildskov, and R. McFee, “Resistivity of Body Tissues at Low Frequencies,” *Circulation Research,* vol. 12, no. 1, pp. 40-50, 1963.
[157] X. Li, and B. He, “Magnetoacoustic tomography with magnetic induction (MAT-MI) for electrical conductivity imaging,” *Conf Proc IEEE Eng Med Biol Soc,* vol. 2009, pp. 3173-6, 2009.
[158] X. Li, L. Mariappan, and B. He, “Three-dimensional multiexcitation magnetoacoustic tomography with magnetic induction,” *J Appl Phys,* vol. 108, no. 12, pp. 124702, Dec 15, 2010.
[159] L. Mariappan, G. Hu, and B. He, “Magnetoacoustic tomography with magnetic induction for high-resolution bioimepedance imaging through vector source reconstruction under the static field of MRI magnet,” *Med Phys,* vol. 41, no. 2, pp. 022902, Feb, 2014.

[160] R. Cailleau, M. Olive, and Q. V. Cruciger, “Long-term human breast carcinoma cell lines of metastatic origin: preliminary characterization,” *In Vitro,* vol. 14, no. 11, pp. 911-5, Nov, 1978.
[161] J. W. Cassidy, C. Caldas, and A. Bruna, “Maintaining Tumor Heterogeneity in Patient-Derived Tumor Xenografts,” *Cancer Res,* vol. 75, no. 15, pp. 2963-8, Aug 1, 2015.
[162] C. L. Morton, and P. J. Houghton, “Establishment of human tumor xenografts in immunodeficient mice,” *Nat Protoc,* vol. 2, no. 2, pp. 247-50, 2007.
[163] M. Lacroix, and G. Leclercq, “Relevance of breast cancer cell lines as models for breast tumours: an update,” *Breast Cancer Research and Treatment,* vol. 83, no. 3, pp. 249-289, Feb, 2004.
[164] D. T. Ross, U. Scherf, M. B. Eisen, C. M. Perou, C. Rees, P. Spellman, V. Iyer, S. S. Jeffrey, M. Van de Rijn, M. Waltham, A. Pergamenschikov, J. C. E. Lee, D. Lashkari, D. Shalon, T. G. Myers, J. N. Weinstein, D. Botstein, and P. O. Brown, “Systematic variation in gene expression patterns in human cancer cell lines,” *Nature Genetics,* vol. 24, no. 3, pp. 227-235, Mar, 2000.
[165] S. Sellappan, R. Grijalva, X. Y. Zhou, W. T. Yang, M. Bar Eli, G. B. Mills, and D. H. Yu, “Lineage infidelity of MDA-MB-435 cells: Expression of melanocyte proteins in a breast cancer cell line,” *Cancer Research,* vol. 64, no. 10, pp. 3479-3485, May 15, 2004.
[166] J. M. Rae, S. J. Ramus, M. Waltham, J. E. Armes, I. G. Campbell, R. Clarke, R. J. Barndt, M. D. Johnson, and E. W. Thompson, “Common origins of MDA-MB-435 cells from various sources with those shown to have melonoma properties,” *Clinical & Experimental Metastasis,* vol. 21, no. 6, pp. 543-552, 2004.
[167] V. V. T. S. Prasad, and R. O. G. Gopalan, “Continued use of MDA-MB-435, a melanoma cell line, as a model for human breast cancer, even in year, 2014,” *npj Breast Cancer,* vol. 1, pp. 15002, 2015.
[168] A. F. Chambers, “MDA-MB-435 and M14 cell lines: identical but not M14 melanoma?,” *Cancer Res,* vol. 69, no. 13, pp. 5292-3, Jul 1, 2009.
[169] W. Wang, and S. R. Eisenberg, “A three-dimensional finite element method for computing magnetically induced currents in tissues,” *IEEE Transactions on Magnetics,* vol. 30, no. 6, pp. 5015-5023, 1994.
[170] Q. A. Pankhurst, J. Connolly, S. K. Jones, and J. Dobson, “Applications of magnetic nanoparticles in biomedicine,” *Journal of Physics D-Applied Physics,* vol. 36, no. 13, pp. R167-R181, Jul 7, 2003.
[171] Q. Shao, E. Morgounova, C. L. Jiang, J. Choi, J. Bischof, and S. Ashkenazi, “In vivo photoacoustic lifetime imaging of tumor hypoxia in small animals,” *Journal of Biomedical Optics,* vol. 18, no. 7, Jul, 2013.
[172] C. L. Jiang, Z. P. Qin, and J. Bischof, “Membrane-Targeting Approaches for Enhanced Cancer Cell Destruction with Irreversible Electroporation,” *Annals of Biomedical Engineering,* vol. 42, no. 1, pp. 193-204, Jan, 2014.

[173] Y. Xu, L. V. Wang, G. Ambartsoumian, and P. Kuchment, “Reconstructions in limited-view thermoacoustic tomography,” *Med Phys,* vol. 31, no. 4, pp. 724-33, Apr, 2004.
[174] M. A. Anastasio, J. Zhang, X. C. Pan, Y. Zou, G. Ku, and L. H. V. Wang, “Half-time image reconstruction in thermoacoustic tomography,” *Ieee Transactions on Medical Imaging,* vol. 24, no. 2, pp. 199-210, Feb, 2005.
[175] M. Xu, and L. V. Wang, “Pulsed-microwave-induced thermoacoustic tomography: filtered backprojection in a circular measurement configuration,” *Med Phys,* vol. 29, no. 8, pp. 1661-9, Aug, 2002.
[176] G. Hu, and B. He, “Magnetoacoustic Imaging of Electrical Conductivity of Biological Tissues at a Spatial Resolution Better than 2 mm,” *Plos One,* vol. 6, no. 8, Aug 12, 2011.
[177] T. Sadhukha, T. S. Wiedmann, and J. Panyam, “Inhalable magnetic nanoparticles for targeted hyperthermia in lung cancer therapy,” *Biomaterials,* vol. 34, no. 21, pp. 5163-71, Jul, 2013.
[178] X. M. Tang, M. Varella-Garcia, A. C. Xavier, E. Massarelli, N. Ozburn, C. Moran, and I. I. Wistuba, “Epidermal Growth Factor Receptor Abnormalities in the Pathogenesis and Progression of Lung Adenocarcinomas,” *Cancer Prevention Research,* vol. 1, no. 3, pp. 192-200, Aug, 2008.
[179] D. T. Merrick, J. Kittelson, R. Winterhalder, G. Kotantoulas, S. Ingeberg, R. L. Keith, T. C. Kennedy, Y. E. Miller, W. A. Franklin, and F. R. Hirsch, “Analysis of c-ErbB1/epidermal growth factor receptor and c-ErbB2/HER-2 expression in bronchial dysplasia: Evaluation of potential targets for chemoprevention of lung cancer,” *Clinical Cancer Research,* vol. 12, no. 7, pp. 2281-2288, Apr 1, 2006.
[180] X. T. Zhang, S. A. Zhu, and B. He, “Imaging Electric Properties of Biological Tissues by RF Field Mapping in MRI,” *Ieee Transactions on Medical Imaging,* vol. 29, no. 2, pp. 474-481, Feb, 2010.
[181] Y. Xu, and L. V. Wang, “Effects of acoustic heterogeneity in breast thermoacoustic tomography,” *IEEE Trans Ultrason Ferroelectr Freq Control,* vol. 50, no. 9, pp. 1134-46, Sep, 2003.
[182] X. D. Wang, Y. J. Pang, G. Ku, X. Y. Xie, G. Stoica, and L. H. V. Wang, “Noninvasive laser-induced photoacoustic tomography for structural and functional in vivo imaging of the brain,” *Nature Biotechnology,* vol. 21, no. 7, pp. 803-806, Jul, 2003.
[183] L. Kunyansky, “A mathematical model and inversion procedure for magneto-acousto-electric tomography,” *Inverse Problems,* vol. 28, no. 3, pp. 35002, 2011.
[184] A. J. Casper, D. Liu, J. R. Ballard, and E. S. Ebbini, “Real-time implementation of a dual-mode ultrasound array system: in vivo results,” *IEEE Trans Biomed Eng,* vol. 60, no. 10, pp. 2751-9, Oct, 2013.
[185] A. Haritonova, D. Liu, and E. S. Ebbini, “In Vivo Application and Localization of Transcranial Focused Ultrasound Using Dual-Mode Ultrasound Arrays,” *IEEE Trans. Ultrasonics, Ferroelectrics and Frequency Control (UFFC), under review; (Invited)*, 2014.

[186] Y. Tufail, A. Matyushov, N. Baldwin, M. L. Tauchmann, J. Georges, A. Yoshihiro, S. I. Tillery, and W. J. Tyler, “Transcranial pulsed ultrasound stimulates intact brain circuits,” *Neuron,* vol. 66, no. 5, pp. 681-94, Jun 10, 2010.
[187] Y. Tufail, A. Yoshihiro, S. Pati, M. M. Li, and W. J. Tyler, “Ultrasonic neuromodulation by brain stimulation with transcranial ultrasound,” *Nat Protoc,* vol. 6, no. 9, pp. 1453-70, Sep, 2011.
[188] F. A. Duck, “Acoustic saturation and output regulation,” *Ultrasound in Medicine and Biology,* vol. 25, no. 6, pp. 1009-1018, 1999.
[189] FDA, "Information for Manufacturers Seeking Marketing Clearance of Diagnostic Ultrasound Systems and Transducers," U. S. D. H. a. H. Services, ed., Center for Devices and Radiological Health, 2008.
[190] M. Muller, “Frequency representation in the rat cochlea,” *Hear Res,* vol. 51, no. 2, pp. 247-54, Feb, 1991.
[191] S. Makeig, M. Westerfield, T. P. Jung, S. Enghoff, J. Townsend, E. Courchesne, and T. J. Sejnowski, “Dynamic brain sources of visual evoked responses,” *Science,* vol. 295, no. 5555, pp. 690-4, Jan 25, 2002.
[192] T. D. Lagerlund, F. W. Sharbrough, and N. E. Busacker, “Spatial filtering of multichannel electroencephalographic recordings through principal component analysis by singular value decomposition,” *Journal of Clinical Neurophysiology,* vol. 14, no. 1, pp. 73-82, Jan, 1997.
[193] P. A. Valdes-Hernandez, A. Sumiyoshi, H. Nonaka, R. Haga, E. Aubert-Vasquez, T. Ogawa, Y. Iturria-Medina, J. J. Riera, and R. Kawashima, “An in vivo MRI Template Set for Morphometry, Tissue Segmentation, and fMRI Localization in Rats,” *Front Neuroinform,* vol. 5, pp. 26, 2011.
[194] T. F. Oostendorp, J. Delbeke, and D. F. Stegeman, “The conductivity of the human skull: results of in vivo and in vitro measurements,” *IEEE Trans Biomed Eng,* vol. 47, no. 11, pp. 1487-92, Nov, 2000.
[195] Y. Lai, W. van Drongelen, L. Ding, K. E. Hecox, V. L. Towle, D. M. Frim, and B. He, “Estimation of in vivo human brain-to-skull conductivity ratio from simultaneous extra- and intra-cranial electrical potential recordings,” *Clin Neurophysiol,* vol. 116, no. 2, pp. 456-65, Feb, 2005.
[196] Y. Zhang, W. van Drongelen, and B. He, “Estimation of in vivo brain-to-skull conductivity ratio in humans,” *Appl Phys Lett,* vol. 89, no. 22, pp. 223903-2239033, 2006.
[197] M. S. Hämäläinen, and R. J. Ilmoniemi, “Interpreting magnetic fields of the brain: minimum norm estimates,” *Medical & Biological Engineering & Computing,* vol. 32, no. 1, pp. 35-42, 1994.
[198] E. Maris, J. M. Schoffelen, and P. Fries, “Nonparametric statistical testing of coherence differences,” *J Neurosci Methods,* vol. 163, no. 1, pp. 161-75, Jun 15, 2007.
[199] W. J. Tyler, “Noninvasive neuromodulation with ultrasound? A continuum mechanics hypothesis,” *Neuroscientist,* vol. 17, no. 1, pp. 25-36, Feb, 2011.

[200] J. Mueller, and W. J. Tyler, “A quantitative overview of biophysical forces impinging on neural function,” *Physical Biology,* vol. 11, no. 5, pp. 051001, 2014.
[201] J. S. Manlapaz, K. E. Astroem, H. T. Ballantine, Jr., and P. P. Lele, “Effects of Ultrasonic Radiation in Experimental Focal Epilepsy in the Cat,” *Exp Neurol,* vol. 10, pp. 345-56, Oct, 1964.
[202] B. K. Min, A. Bystritsky, K. I. Jung, K. Fischer, Y. Zhang, L. S. Maeng, S. I. Park, Y. A. Chung, F. A. Jolesz, and S. S. Yoo, “Focused ultrasound-mediated suppression of chemically-induced acute epileptic EEG activity,” *BMC Neurosci,* vol. 12, pp. 23, 2011.
[203] M. Plaksin, E. Kimmel, and S. Shoham, “Cell-Type-Selective Effects of Intramembrane Cavitation as a Unifying Theoretical Framework for Ultrasonic Neuromodulation,” *eNeuro,* vol. 3, no. 3, May-Jun, 2016.
[204] M. Plaksin, S. Shoham, and E. Kimmel, “Intramembrane cavitation as a predictive bio-piezoelectric mechanism for ultrasonic brain stimulation,” *Journal of Molecular Neuroscience,* vol. 53, pp. S103-S103, Aug, 2014.
[205] A. Bystritsky, A. S. Korb, P. K. Douglas, M. S. Cohen, W. P. Melega, A. P. Mulgaonkar, A. DeSalles, B. K. Min, and S. S. Yoo, “A review of low-intensity focused ultrasound pulsation,” *Brain Stimul,* vol. 4, no. 3, pp. 125-36, Jul, 2011.
[206] W. J. Tyler, Y. Tufail, M. Finsterwald, M. L. Tauchmann, E. J. Olson, and C. Majestic, “Remote Excitation of Neuronal Circuits Using Low-Intensity, Low-Frequency Ultrasound,” *Plos One,* vol. 3, no. 10, Oct 29, 2008.
[207] M. Scanziani, and M. Hausser, “Electrophysiology in the age of light,” *Nature,* vol. 461, no. 7266, pp. 930-9, Oct 15, 2009.
[208] S. Hippenmeyer, E. Vrieseling, M. Sigrist, T. Portmann, C. Laengle, D. R. Ladle, and S. Arber, “A developmental switch in the response of DRG neurons to ETS transcription factor signaling,” *PLoS Biol,* vol. 3, no. 5, pp. e159, May, 2005.
[209] J. Z. Tsien, D. F. Chen, D. Gerber, C. Tom, E. H. Mercer, D. J. Anderson, M. Mayford, E. R. Kandel, and S. Tonegawa, “Subregion- and cell type-restricted gene knockout in mouse brain,” *Cell,* vol. 87, no. 7, pp. 1317-26, Dec 27, 1996.
[210] E. Krook-Magnuson, C. Armstrong, M. Oijala, and I. Soltesz, “On-demand optogenetic control of spontaneous seizures in temporal lobe epilepsy,” *Nat Commun,* vol. 4, pp. 1376, 2013.
[211] R. Oostenveld, P. Fries, E. Maris, and J. M. Schoffelen, “FieldTrip: Open source software for advanced analysis of MEG, EEG, and invasive electrophysiological data,” *Comput Intell Neurosci,* vol. 2011, pp. 156869, 2011.
[212] M. O. Culjat, D. Goldenberg, P. Tewari, and R. S. Singh, “A review of tissue substitutes for ultrasound imaging,” *Ultrasound Med Biol,* vol. 36, no. 6, pp. 861-73, Jun, 2010.
[213] W. D. O'Brien, Jr., “Ultrasound-biophysics mechanisms,” *Prog Biophys Mol Biol,* vol. 93, no. 1-3, pp. 212-55, Jan-Apr, 2007.

[214] S. A. Goss, R. L. Johnston, and F. Dunn, “Comprehensive compilation of empirical ultrasonic properties of mammalian tissues,” *The Journal of the Acoustical Society of America,* vol. 64, no. 2, pp. 423-457, 1978.
[215] W. J. Fry, and R. B. Fry, “Temperature Changes Produced in Tissue during Ultrasonic Irradiation,” *Journal of the Acoustical Society of America,* vol. 25, no. 1, pp. 6-11, 1953.
[216] A. Ersen, A. Abdo, and M. Sahin, “Temperature elevation profile inside the rat brain induced by a laser beam,” *Journal of Biomedical Optics,* vol. 19, no. 1, pp. 015009, 2014.
[217] P. D. Murray, and A. Keller, “Somatosensory response properties of excitatory and inhibitory neurons in rat motor cortex,” *Journal of Neurophysiology,* vol. 106, no. 3, pp. 1355-1362, 2011.
[218] V. B. Mountcastle, W. H. Talbot, H. Sakata, and J. Hyvärinen, “Cortical neuronal mechanisms in flutter-vibration studied in unanesthetized monkeys. Neuronal periodicity and frequency discrimination,” *Journal of Neurophysiology,* vol. 32, no. 3, pp. 452-484, 1969.
[219] D. J. Simons, “Response properties of vibrissa units in rat SI somatosensory neocortex,” *Journal of Neurophysiology,* vol. 41, no. 3, pp. 798-820, 1978.
[220] R. M. Bruno, and D. J. Simons, “Feedforward mechanisms of excitatory and inhibitory cortical receptive fields,” *J Neurosci,* vol. 22, no. 24, pp. 10966-75, Dec 15, 2002.
[221] J. Kubanek, “Neuromodulation with transcranial focused ultrasound,” *Neurosurg Focus,* vol. 44, no. 2, pp. E14, Feb, 2018.
[222] F. A. Duck, “Medical and non-medical protection standards for ultrasound and infrasound,” *Prog Biophys Mol Biol,* vol. 93, no. 1-3, pp. 176-91, Jan-Apr, 2007.
[223] Y. Younan, T. Deffieux, B. Larrat, M. Fink, M. Tanter, and J. F. Aubry, “Influence of the pressure field distribution in transcranial ultrasonic neurostimulation,” *Med Phys,* vol. 40, no. 8, pp. 082902, Aug, 2013.
[224] D. E. Sosnovik, M. Nahrendorf, and R. Weissleder, “Magnetic nanoparticles for MR imaging: agents, techniques and cardiovascular applications,” *Basic Res Cardiol,* vol. 103, no. 2, pp. 122-30, Mar, 2008.
[225] D. P. Cormode, P. C. Naha, and Z. A. Fayad, “Nanoparticle contrast agents for computed tomography: a focus on micelles,” *Contrast Media Mol Imaging,* vol. 9, no. 1, pp. 37-52, Jan-Feb, 2014.
[226] M. Mehrmohammadi, J. Oh, S. Mallidi, and S. Y. Emelianov, “Pulsed magneto-motive ultrasound imaging using ultrasmall magnetic nanoprobes,” *Mol Imaging,* vol. 10, no. 2, pp. 102-10, Apr, 2011.
[227] B. Gleich, and J. Weizenecker, “Tomographic imaging using the nonlinear response of magnetic particles,” *Nature,* vol. 435, no. 7046, pp. 1214-7, Jun 30, 2005.
[228] J. Lange, R. Kotitz, A. Haller, L. Trahms, W. Semmler, and W. Weitschies, “Magnetorelaxometry - a new binding specific detection method based on magnetic nanoparticles,” *Journal of Magnetism and Magnetic Materials,* vol. 252, no. 1-3, pp. 381-383, Nov, 2002.